MODELING CONTROLLED-SOURCE ELECTROMAGNETIC RESPONSES OF

IDEALIZED HYDRAULIC FRACTURING SCENARIOS

A Dissertation

by

MATTHEW JOHN COUCHMAN

Submitted to the Office of Graduate and Professional Studies of
Texas A&M University
in partial fulfillment of the requirements for the degree of

DOCTOR OF PHILOSOPHY

Chair of Committee,	Mark Everett
Committee Members,	Benchun Duan
	Yuefeng Sun
	John Killough
Head of Department,	Julie Newman

December 2019

Major Subject: Geophysics

ABSTRACT

I explore the capability of terrestrial controlled source electromagnetic (CSEM) methods to detect electrically conductive injected fluids associated with hydraulic fracturing of unconventional reservoirs. An existing finite element program is modified to incorporate a rectangular mesh for implementation of geologic features such as slabs with given dimensions and conductivities, and is validated by comparisons to analytical responses. Local mesh refinement around the lateral wellbore in conjunction with a transverse conductance argument enables a first order approximation for modeling the long slender wellbore, since its realistic dimensions are not feasible to model. My numerical results find that responses from the lateral wellbore are ~5 orders of magnitude greater than those from fluid-filled fracture zones. Inline responses provide more information than broadside responses, including the depth of a lateral wellbore and the lateral location of a fluid-filled fracture zone. Host sediment conductivity is an important factor, as the response to a fracture zone is 100 times larger in terrestrial sediments than clays. If both lateral wellbore and fluid zones are present, the wellbore response dominates. Once the response of the wellbore is removed, the residual response remains dominated by a residual wellbore signature. This is likely caused by mutual inductance of the wellbore and fluid zones. The composite signature provides scant information regarding the location of the fluid zone; though the signature of the latter is somewhat preserved. The wellbore, especially its toe, is shown to act as a secondary source. Further tests suggest that the wellbore-fluid coupling is inductive rather than

galvanic, although the latter cannot be discounted. The detection of fracture zones likely

depends on the source used, the host sediment conductivity, and the ambient

electromagnetic noise levels, which vary from site to site and from day to day.

ACKNOWLEDGEMENTS

CONTRIBUTORS AND FUNDING SOURCES

Contributors

This work was supervised by dissertation committee consisting of Professor Mark Everett [advisor] and Professors Bechun Duan and Yuefeng Sun of the Department of Geology and Geophysics and Professor John Killough of the Department of Petroleum Engineering.

Funding Sources

TABLE OF CONTENTS

LIST OF FIGURES

xiv

LIST OF TABLES

CHAPTER I

INTRODUCTION

Real-time monitoring of the efficiency of unconventional hydrocarbon extraction is a tremendous challenge facing the oil and gas industry. The daily production level of tight oil in the United States was ~9 million barrels per day in February 2017 (Figure 1) with predictions ranging up to productions levels of 17 million barrels per day by 2040. Most estimates for U.S oil production forecast tight oil being more productive than non-tight, or conventional oil. With the upwards trajectory of tight shale production and hence its increasing importance to the nation's overall energy portfolio, monitoring the efficiency of projects that involve tight shales becomes ever more valuable to the future economy. Figure 2 shows the distribution of tight shale plays throughout the lower 48 states in 2015; the wide spatial distribution emphasizes their abundance. This project explores an emerging oilfield technology that could enable more efficient fracture monitoring. The objective of the technology is to image fluid movement away from the wellbore. Knowledge of fluid pathways could be used to make hydraulic fracturing projects more efficient. Furthermore this technology may also be of use in near-surface applications to detect and monitor fluid leakage from pipelines. The main objective of my dissertation project is to develop the fundamental understanding that is necessary to evaluate the potential for terrestrial controlled source electromagnetic (CSEM) monitoring of fluids flowing from a pipeline or wellbore. Such understanding would enable petroleum engineers to detect hydraulic fracture fluids based on their CSEM

1

signature and, if coupled to an accurate geomechanical model, perhaps to infer the subsurface flow pathways of the electrically conductive injected fluids. The work here focuses on terrestrial CSEM; however, it builds on technological advances recently made in marine CSEM technology. Marine and terrestrial CSEM field acquisition schematics are shown in Figures 3 and 4.

The potential application of terrestrial CSEM to development of unconventional petroleum resources motivated this project; however, there are alternative applications of the technology. The project is designed to better understand, regardless of application, CSEM monitoring subsurface fluid movements that present an electrical conductivity contrast to the host geological formation. Monitoring of geothermal fluids or groundwater is a relevant application of this technology. Investigations about the role of fractures and geomechanical properties in shaping an electromagnetic signal is applicable to hydrocarbons, geothermal fluids, groundwater and CO_2 for sequestration. CSEM surveys may also be used in tandem with aeromagnetic surveys at potential geothermal sites to provide detailed and reliable maps of fluid connectivity. CSEM complements the magnetotelluric (MT) method, particularly in the monitoring of deep electrically conductive fluids. The technology may also be developed as a means to infer pathways of conductive nuclear waste through fractures in a resistive host rock. Finally, the method could also be applicable to other planetary bodies. The use of CSEM could be investigated, for example, as a low-frequency electromagnetic exploration tool for detecting groundwater movement beneath the surface of Mars.
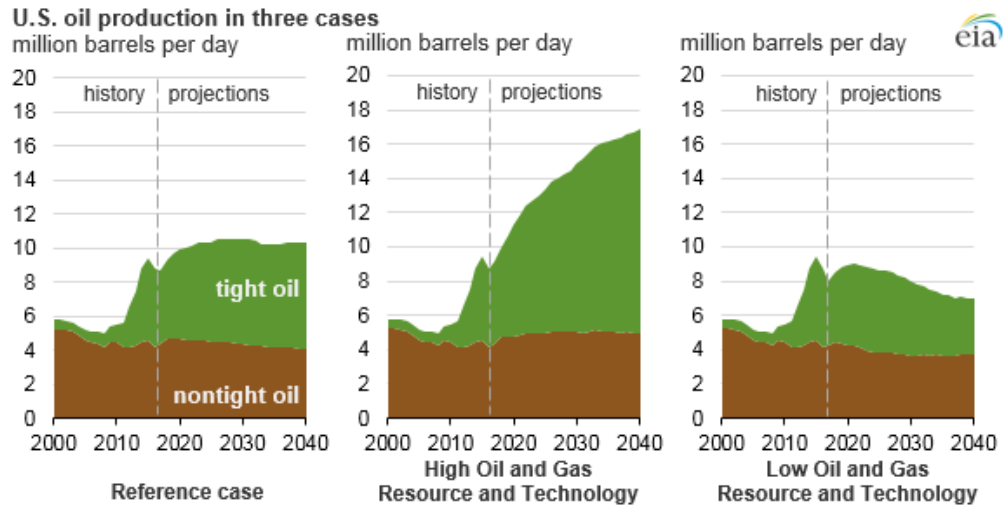
Figure 1 Predictions for production of tight oil and non-tight oil (EIA, 2017)
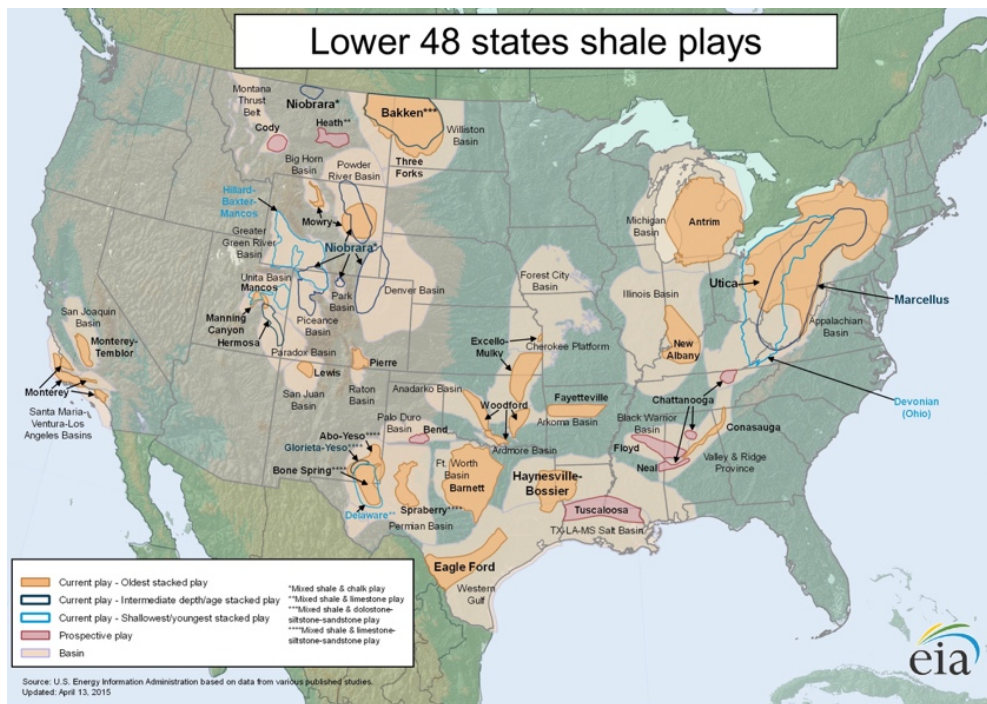
Figure 2 Map Showing tight shale plays in lower 48 US states as of May 2011 (EIA, 2016)
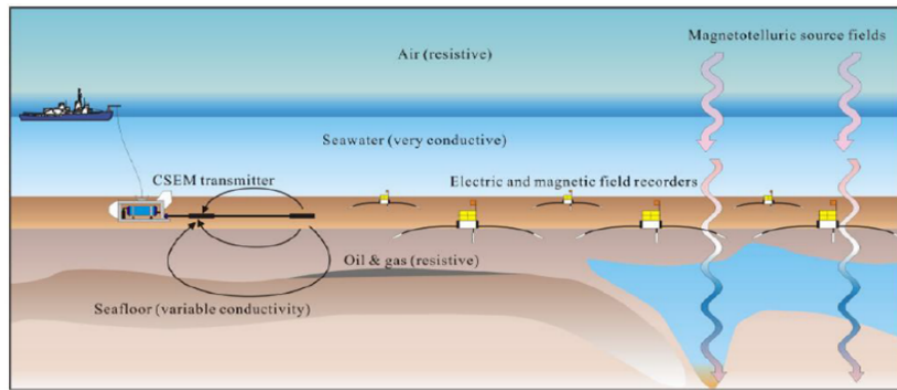
Figure 3 Schematic of typical marine CSEM acquisition and parameters (modified from Constable & Srnka, 2007)
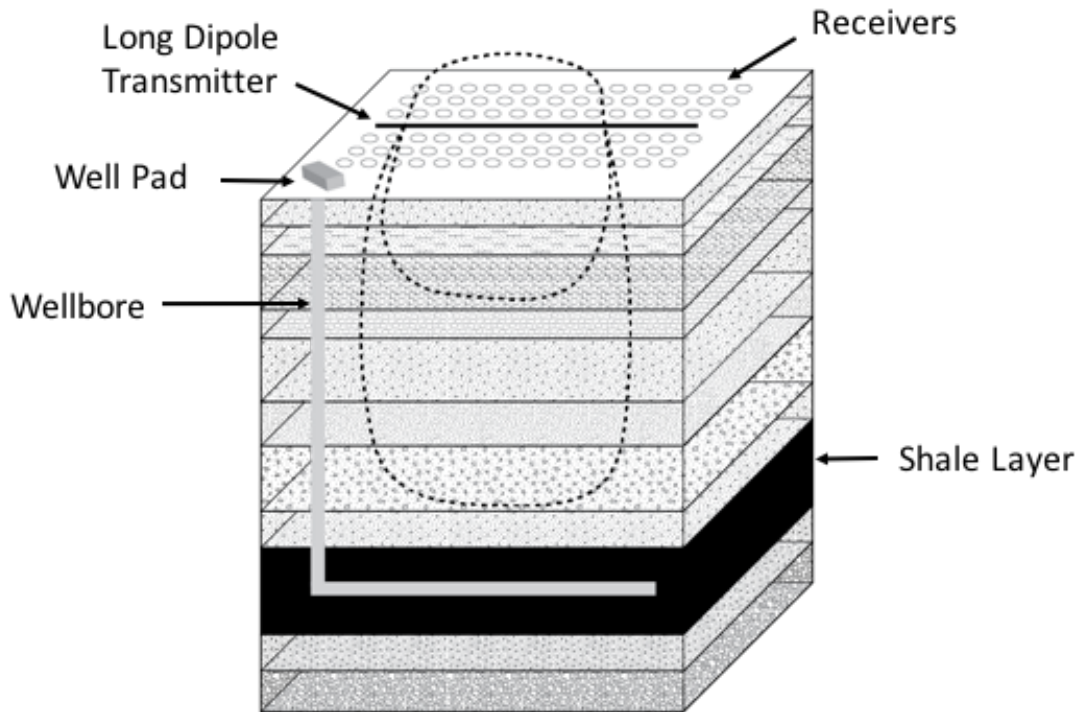
Figure 4 Example of a CSEM acquisition configuration in tight shale environment. Layout consists of a long-dipole source (solid) and electric field sensors (ellipses) on the surface directly above a lateral wellbore. An example of the dipole field is shown (black, dashed)

Literature Review

Early Terrestrial Research – Academia

The first concerted development of controlled source electromagnetics for direct hydrocarbon prospection took place in the former Soviet Union in the 1960s. However, earlier attempts had been made for terrestrial hydrocarbon exploration as far back as the 1930s (Schlumberger, et al., 1934, Rust, 1938). An early system outlined in a patent (Barret, 1939) describes a system transmitting at 1.9 MHz from a grounded dipole source. The system designer claimed to detect anomalies in the received electromagnetic field that were caused by reflections from the edges of oil-bearing anticlinal traps in various Texas, Louisiana and Oklahoma oilfields. The anomalies proved not to be reliable oil indicators. As later analysis showed, they were likely caused by terrain irregularities and near-surface heterogeneities located along the transmitter-to-receiver path.

The CSEM method is linked to its natural-source cousin, the magnetotelluric (MT) method developed in the 1950's by Cagniard (1953) and others. MT methods should be considered when discussing the history of the CSEM method. Since MT has not proven to be a useful hydrocarbon prospection method however, I refer attention here to an overview of magnetotellurics found in Vozoff (1990).

The majority of early CSEM studies were focused on terrestrial environments, with much of this work being applied towards the detection of hydrocarbon-bearing reservoirs. The research developed in the former Soviet Union was brought to the United States by Professor George Keller of the Colorado School of Mines. In a seminal 1969

World Oil magazine article (Keller, 1969), Keller described a prototype CSEM system operating at a base frequency of 0.1 Hz, featuring a 28 kW grounded bipole source with broadside magnetic field sensors capturing responses at ranges from 8-30 km.

During the 1980s, an analytical modeling study along with a field example from Venezuela comprised the 1981 Ph.D. dissertation of Hermino Passalacqua (Passalacqua, 1981). His subsequent paper (Passalacqua, 1983) demonstrated, for the first time, that the electromagnetic response from a grounded–wire dipole source depends sensitively on the transverse resistance (resistivity-thickness) product of a thin oil-bearing layer. Passalacqua clearly explained how the key detection mechanism proves to be electric charge accumulation at the top and bottom interfaces of the thin resistive layer that adjoins the enclosing, relatively conductive geological medium.

Advances in Academic Marine Methods – Pre 2010

After the 1960s CSEM research in marine settings began to gain ground, for both oil exploration and other applications such as submarine seabed-to-seabed communication (Chave, et al., 1990). Here, I summarize aspects of two review papers which outline the history of academic marine CSEM development (Constable, 2010; Constable & Srnka, 2007).

The earliest published work describing the marine CSEM technique is that of Bannister (1698), which focused on theoretical responses of a frequency-domain, seafloor-to-seafloor, dipole-dipole configuration. Researchers at Scripps Institution of Oceanography have carried out CSEM experiments since the late 1970s to study the

6

shallow resistive parts of the oceanic lithosphere. This was accomplished by replacing the relatively high frequency energy lost to MT fields with that provided by a deep-towed transmitter. Similar developments were made by Martin Sinha and his group at the University of Cambridge throughout the 1980s. During this time the mid-ocean ridge had become a key area of interest to the CSEM community and a neutrally buoyant transmitter "flown" 100 m above the seafloor was deployed over the rough bathymetry at the mid-ocean ridge (Sinha, et al., 1990). The deep-tow technology would later be adapted for hydrocarbon exploration. A 1981 presentation given by Alan Chave at a meeting of the Scripps Industrial Associates showed calculations that demonstrated how the amplitude and phase response of a marine CSEM system consisting of in-line electric dipole transmitter and receivers, operating at frequencies of 0.1-10 Hz and transmitter-receiver (TX-RX) offsets of 1-5 km, can resolve a resistive layer representative of a submarine oilfield.

An analytic layered-earth (1D) solution for the frequency-domain electric dipole configuration was developed by Chave and Cox (1982). Improvements to 1D modeling were developed in the 1980s including: solutions for time-domain excitation (Edwards & Chave, 1986); the inclusion of a fast Hankel transform (Flosadottir & Constable, 1996); and development of 1D inversion algorithms (Flosadottir & Constable, 1996). Further development of marine CSEM techniques occurred throughout the 1990s. During this time 2.5D (spatially compact source deployed over a two-dimensional seafloor) numerical finite-element methods were introduced for time domain (Everett &

7

Edwards, 1992) and frequency domain (Unsworth, et al., 1993) configurations. This was followed by inversion algorithms (e.g. MacGregor, et al., 2001).

Computational restrictions denied the use of full 3D modeling in the 1990s. However, 3D numerical algorithms were introduced by the turn of the century and were flexible enough to include water layers, an air layer, multiple geological layers, and simple shapes such as a disk or slab that may be used to represent a conductive or resistive body. Early examples include finite difference (Newman & Alumbaugh, 1995) and finite element (Badea et al., 2001) approaches.

Recent Marine Advances (2010-2019)

Marine CSEM techniques for hydrocarbon exploration have continued to be developed with a significant amount of research being conducted at Scripps Institute of Oceanography. Recent publications discuss the use of marine CSEM for exploration in the Gulf of Mexico (Weitemeyer, et al., 2017) and at Scarbrough gas field offshore western Australia, focusing on experimental design and 2D inversion (Myer, et al., 2012; Myer, et al., 2015). Another publication describes the application of CSEM 3D forward modeling in the Flemish Basin (Dunham, et al., 2018). Further research from Scripps has discussed a deep-towed CSEM receiver (Constable, et al., 2016) and AUV-borne CSEM systems (Bloomer, et al., 2016).

Marine CSEM techniques for hydrocarbon exploration is ongoing with significant research still being conducted at Scripps Institute of Oceanography. Recent publications discuss marine CSEM for exploration in Gulf of Mexico (Weitemeyer, et

al., 2017) and Scarbrough gas field offshore western Australia, focusing on experimental design and 2D inversion (Myer, et al., 2012; Myer, et al., 2015). Another publication describes CSEM 3D forward modeling in Flemish Basin (Dunham, et al., 2018). Further research from Scripps has discussed a deep-towed receiver (Constable, et al., 2016) and an AUV-borne system (Bloomer, et al., 2016).

Multiple other groups have conducted research on marine CSEM techniques. There has been research into the effects of anisotropy on CSEM responses (Bouchara, et al., 2015) and integration of seismic and CSEM data (Alvarez et al., 2017; Alvarez et al., 2017), including investigations of seismically-regularized CSEM inversion (Brown et al., 2012; Guo, et al., 2017) and CSEM-regularized seismic velocity inversion (Colombo, et al., 2018). A further investigation of marine CSEM inversion is found in Ayani, et al. (2017). In addition to integration of seismic and CSEM data, studies of integrated CSEM and magnetotelluric data have been conducted (Hoversten et al., 2015).

A comparison of time and frequency domain CSEM for hydrocarbon exploration appears in Connell & Key (2013). Studies into the separate sea and subseafloor contributions to CSEM responses have also been published (Calderón-Moctezuma, et al., 2017). Liu et al. (2018) has suggested a hybrid solver that combines integral equation and differential equation methods. Further work has taken place to understand the CSEM response of multiple steel casings embedded in a layered earth (Kohnke, et al., 2018) and efforts toward denoising marine CSEM data have been considered (Yang, et al., 2018).

Recent Academic & Industry Terrestrial

In recent years, advances have also been made in terrestrial CSEM. Studies have demonstrated more efficient ways to generate a computational mesh (Weiss & Wilson, 2017), methods to insert a realistic wellbore into the mesh (Patzer, et al., 2017), or to consider a steel-cased borehole as an electrical transmission line (Aldridge, et al., 2015). There has also been work done on relating CSEM responses to fracture propagation, fluid flow and the geomechanics of water-based hydraulic fracturing (Um & Kim, 2016; Kim et al., 2014). This remains a field with room for new contributions. Recent work has focused on borehole (Tietze, et al., 2017) and borehole-to-surface (Tietze et al., 2015) CSEM monitoring of oilfield operations. A contribution has also been made to understand the effect of topography on CSEM responses (Hickey, et al., 2010). Finally there are various examples of CSEM field studies in the Eagle Ford, Anadarko and Delaware basins and the Schoonebeck oil field (Hickey, et al., 2015; Hickey, et al., 2017; Schaller et al., 2017). Streich (2016) provides a comprehensive review of CSEM approaches to hydrocarbon detection in terrestrial environments.

Non-Hydrocarbon

There has been significant research applying the terrestrial CSEM method in non-hydrocarbon exploration scenarios. A review can be found in Thiel (2017). As discussed there, CSEM has been used for tracking fluid movement in geothermal reservoirs and for CO_2 sequestration analysis. Examples of CSEM studies for characterizing gas hydrates include Attias, et al. (2014) and Goswami, et al. (2013). In

addition to characterizing fluids, CSEM methods have also been used for mapping resistive permafrost (Sherman, et al., 2017).

Outline of Dissertation

The structure of this dissertation is as follows. The next chapter describes the theoretical and computational background behind the finite element algorithm used for this project. In this chapter, I split the discussion into mesh generation, finite-element linear system solution, and post processing. Chapter 2 also reviews some necessary electromagnetic theory. Chapter 3 discusses validation of the rectangular and cylindrical meshes. Chapter 4 discusses the benefits and limitation of the conductance argument used for modeling the lateral wellbore. Chapter 5 contains modeling of in-line and broadside responses from simplified hydraulic fracturing scenarios, including the separate and combined effects of a lateral wellbore and fluid-filled fracture zones. Chapter 6 focuses on the field patterns in a terrestrial environment and how they are influenced by the lateral wellbore and the injection of fluid. Chapter 7 discusses the potential future uses and limitations of the terrestrial CSEM technique.

CHAPTER II

FINITE-ELEMENT MODELING ALGORITHM

This research uses an adapted version of the finite-element modeling (FEM)

program developed in FORTRAN 77 by Badea et al. (2001) with modifications by

Stalnaker et al. (2006). The program is split into three routines which are run

sequentially (see Figure 5). The first routine generates the mesh for modeling CSEM

responses. This module includes specification of the geoelectrical model for the scenario

under test. The second routine computes the secondary Coulomb-gauged potentials on

all mesh nodes, based on a source vector comprised of analytically derived primary

potentials. Addition of the secondary and primary potentials provides the total potentials.

The primary, secondary and total potentials are output on surface, or seafloor, nodes to

facilitate predictions of actual measurements. The third routine interpolates the solutions

across surface, or seafloor, nodes in the two horizontal (x, y) directions. This procedure

provides the in-line and broadside responses that would be measured by ideal noise-free

receivers. A parameter file is required that contains information such as mesh aspect

ratio, required tolerance on the linear solver, background conductivities, etc. Each

routine has its own input file, providing the specific information needed to execute that

module. I have written a fourth routine that may replace or be used with the third

routine. It computes electric field distributions throughout the modeling domain. This

chapter reviews my adaptations to the program but the original paper Badea et al. (2001)

is recommended for complete details of the algorithm.

12
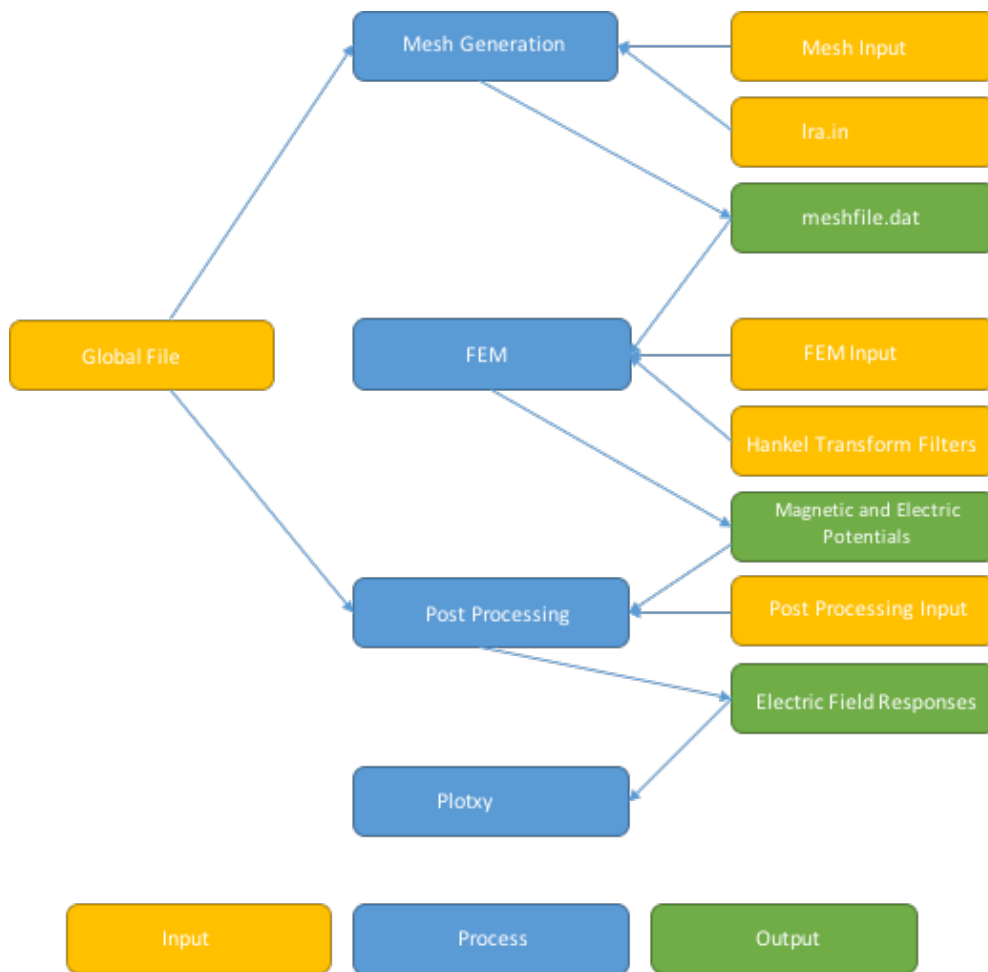
Figure 5 Flow Chart for FEM Program

Background Electromagnetic Theory

To understand how FEM and analytical solutions for a given geoelectrical model are generated, it is important to understand fundamental aspects of electromagnetic (EM) theory. The relevant physics is that of electromagnetic induction due to a grounded source as opposed to a purely inductive source. The former refers to the presence of a grounded wire dipole acting as the source whereas the latter is realized by an inductive loop source. For more information on purely inductive systems see (Everett, 2013).

When discussing electromagnetic induction the Lorentz force (2.1) is of fundamental interest. This is the force experienced by a mobile charge carrier (q) that is moving with velocity v in an electromagnetic field,

$$F = q(E + v \times B) \tag{2.1}$$

In accordance with (2.1), a voltage develops along any arbitrary closed path L, inside a conductive body that is which is exposed to a time-varying magnetic field B. In the CSEM case, the geophysicist shapes the external time-variation of the transmitter waveform.

Mobile charge carriers within a conductor drift in response to an applied electric field E. The drift velocity is much lower than the speed of light due to lattice scattering of the charge carriers. An electric charge current density J is given as

$$J = nqv \tag{2.2}$$

where n corresponds to the volumetric concentration of the charge carrier. It is the induced drift of mobile charges which act as a secondary source of the EM response that is recorded by receivers at the surface.

Maxwell's equations governing the generation and propagation of EM fields are given by

$$\nabla \times E = - \frac{\partial B}{dt} \tag{2.3}$$

$$\nabla \times B = \mu\sigma(r)E + \mu J_s + \mu\varepsilon\frac{\partial E}{\partial t} \tag{2.4}$$

$$\nabla \cdot E = \frac{\rho_{ch}}{\varepsilon} \tag{2.5}$$

$$\nabla \cdot B = 0 \tag{2.6}$$

where E (V/m) represents the electric field, B (T) is the magnetic field, μ (H/m)

represents magnetic permeability, while ε (F/m) refers to the electric permittivity. The

particular value μ_0 is the permeability of free space, $4\pi \times 10^{-7}$(H/m). Throughout this

dissertation, magnetic permeability is assumed to be equal to that of free space as the

magnetic permeability of very few geomaterials differ from this value by an appreciable

amount. The quantity J_s is the applied current density, a parameter that is under

experimenter control. However, when considering the low frequencies relevant in this

work, we apply the diffusive Maxwell's equations.

$$\nabla \times E = i\omega\mu_0 H \tag{2.7}$$

$$\nabla \times H = J_s + \sigma E \tag{2.8}$$

where

$$B = \mu_0 H \tag{2.9}$$

In the set of equations (2.7-2.9), we have introduce the auxiliary field H, where

the magnetic field B is the product of the free-space magnetic permeability and the

auxiliary field. The curl of E is proportional to the magnetic field (product of permeability of free space and auxiliary field) and the angular frequency

$$\omega = 2\pi f \tag{2.10}$$

where f is the operating frequency of the transmitter. The σE term in (2.8) corresponds to the induced current density in the subsurface. A harmonic time-variation exp(-iωt) is implicitly assumed in these equations.

The depth of penetration is determined by the skin depth, which corresponds to the depth at which an incident plane wave loses $1/e \sim 36.8\%$ of its incident amplitude.

$$\delta = \sqrt{\frac{2}{\mu\sigma\omega}} \tag{2.11}$$

The skin depth equation (2.11) depends on angular frequency, magnetic permeability, and the conductivity of the medium. The higher the operating frequency and conductivity, the smaller the depth of penetration. This is due to increased efficiency of the conversion of the transmitted EM energy into kinetic energy of mobile charge carriers.

For time-harmonic or other types of excitation, the earth/sea/air system is excited by an EM source. The response measured at a receiver is a weighted spatial average of the conductivity of the whole system. The weighting decreases with increasing distance

from the source to receiver. Thus a target at 1 m range is relatively easy to detect if it is

buried 1 m below the seafloor, but its signal may be buried in noise, or below the

receiver sensitivity, if buried 1 km deep. One can also lower the operating frequency to

increase the depth of investigation, although the spatial resolution will be degraded.

Mesh Generation

The original version of the FEM program used for this study was designed with

wireline logging in mind. The calculations were performed on a cylindrical mesh. This

mesh geometry is not practical for surface-based CSEM as it makes implementation of

geologic features such as fault zones, and the lateral wellbore, challenging to discretize.

Therefore I have modified the mesh generation algorithm to produce a rectangular mesh.
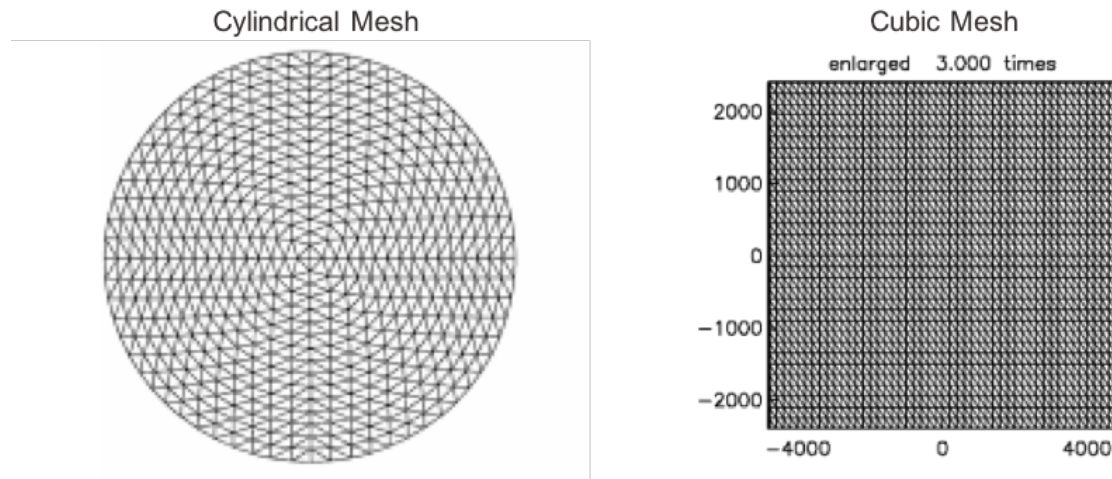
Figure 6 Horizontal slices through cylindrical and rectangular meshes generated in the FEM program

The mesh generation module uses three files: the actual FORTRAN source code,

plus an input file and the global parameter file. The latter prescribes the memory

17

requirements for the mesh, specifies information regarding local refinement (described below, and in chapter 3), and assigns constants such as the mesh size and density, and assigns the conductivities for various background layers.

While the focus herein is on CSEM applied to the terrestrial environment, the program may also compute FEM solutions appropriate to the marine environment. Within the global parameter file, a water depth may be assigned. The global file also specifies the conductivity of the air (nominally 1 x 10^{-8} S/m), that of the water layer if applicable (nominally 3.2 S/m for seawater), and the conductivity of the host sediments.

The mesh size and nodal density is discussed further in chapter 3. A suitable aspect ratio for the lateral extent of the mesh in each direction must be chosen. After much testing, I found that the lateral extent of the mesh in the (x, y) directions should be double that of the vertical extent. On such meshes, FE-computed solutions were compared to several previously published solutions to validate their accuracy and robustness. The density of nodes within the mesh is also a critical parameter. The denser the mesh, the more accurate the solutions. However, an increase in accuracy comes at the cost of increased time and computational memory. A trade-off is therefore necessary considering the resources and time available.

An option for local mesh refinement is included. Local refinement increases the nodal density within a prescribed region of the mesh. This allows for discretization of smaller targets and/or improves the accuracy of solutions in the prescribed region. The global parameter file specifies the number of nested local refinements requested.

18

The input file provides information regarding the geoelectrical model for which the CSEM response is to be computed. The input file supplies the number of layers or 'slabs' within the model, which includes the air and the underlying homogeneous halfspace. The user first specifies the conductivities of these two regions, before providing dimensions and conductivities of any additional slabs.

The mesh generation module uses the information provided by the global and the input files to produce the mesh. The module first creates a regular rectangular mesh based on the information in the global file; then it determines the mesh node coordinates and the vertices of the tetrahedra that comprise the mesh. If required, the mesh is refined within a prescribed region, as specified in a local refinement file. Within the local refinement process, firstly the tetrahedra enclosed in the refinement region are 'marked' before new nodes, termed split points, are added at the midpoints of their edges. Following this, all unmarked tetrahedra which share at least one edge with a marked tetrahedron are selected, and the requisite number of additional split points are determined. The marked tetrahedra are then subdivided into two, four or eight tetrahedra, depending on the number of split points. The local mesh refinement algorithm follows the method of Liu and Joe (1996).

After mesh generation is complete, the mesh volume is calculated, and the quality factor Q, with $0 \leq Q \leq 1$ (Liu and Joe, 1996) of each tetrahedron is determined. As desired, 2D slices through the mesh are output for visualization to check mesh quality (see Figure 6). The sum of the volumes of the mesh tetrahedra should equal the volume of the modeling domain. A quality factor histogram (Figure 7) is constructed that

provides information on the distribution of shapes of the individual tetrahedra

comprising the mesh. A quality factor close to 0 represents a long thin tetrahedron with a

high aspect ratio, while a quality factor close to 1 represents a regular tetrahedron.

Without local refinement, only three shapes of tetrahedra are produced and each has its

distinct quality factor. Local refinement adds tetrahedra with variable quality factors

(Figure 8). A good quality factor is usually between 0.55 and 0.7. The FE solution

accuracy degrades if the mesh contains poorly-shaped tetrahedra so it is important to

maintain a high mesh quality. The 2D mesh visualizations provide an opportunity to

assess mesh quality. The location of these mesh slices is specified by the user. The plots

produce an image of the entire mesh domain and a zoomed image with designated zoom

factor. Finally, the mesh is checked to ensure that a valid nodal connectivity map has

been computed.
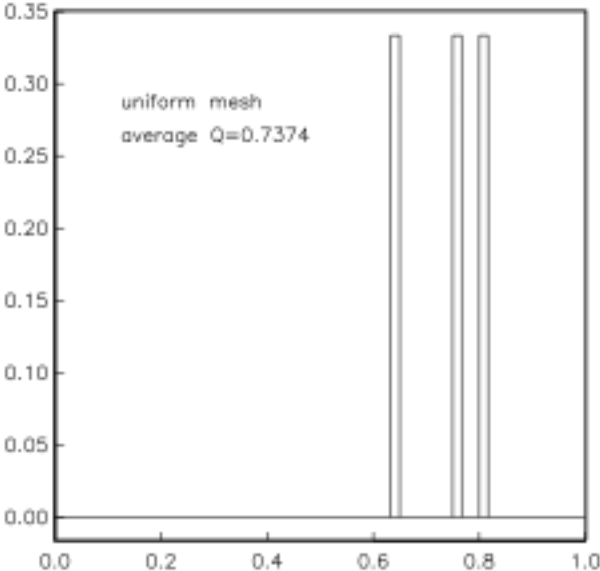
Figure 7 Example of a quality factor histogram of a mesh without local refinement
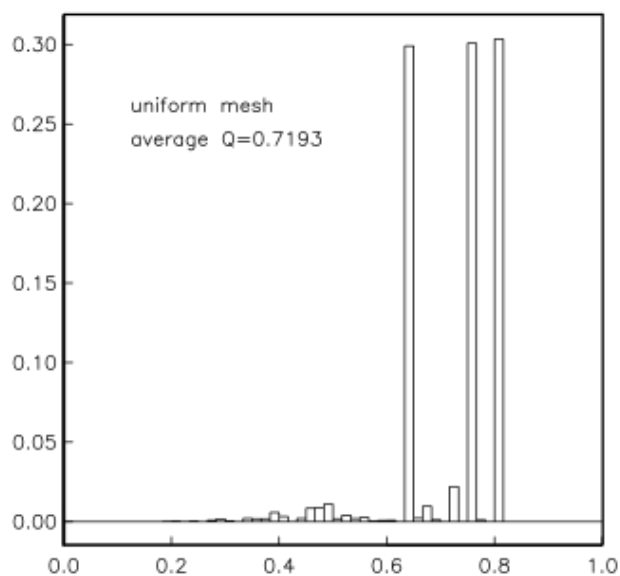
Figure 8 Example of a quality factor histogram of a mesh with local refinement

After the mesh has been checked, the specified slabs are incorporated into the mesh with their appropriate conductivity. The volume of the tetrahedra and the number of nodes within each slab is reported. This provides a simple quality check as the expected volume of the slab can be compared with the volume of the slab actually placed in the mesh.

Analytic Responses

An analytic expression for the CSEM response due to electric dipole excitation may be determined in certain scenarios. This category includes a halfspace of uniform conductivity, or a layered Earth. In the latter case, the response may be computed by the finite element code and verified against previously published solutions. The algorithm

has been so checked against several previously published solutions (e.g. Um & Alambaugh, 2007; Ward & Hohmann, 1987; Weiss, 2007; Streich, 2016) (see chapter 3). Specifically, I have calculated the electric-field response for a 1-D model containing a buried layer (Figure 9). There are several methods that can be used to generate an analytic solution to this problem. A first method directly computes the electric and magnetic fields. A second method computes electromagnetic potentials based on, for example, the Coloumb gauge condition. The latter method allows for the analytic solutions to be used as the primary field in the finite-element code, since it is based on a Coulomb-gauge formulation of Maxwell's governing equations. A Coulomb-gauged analytic solution may be derived for both terrestrial and marine cases.
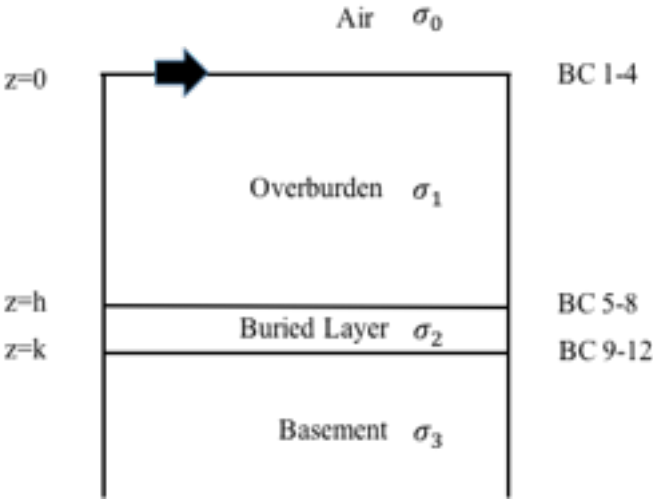
Figure 9 1-D geoelctrical model with buried layer showing locations for each boundary conditions (BC), the transmitter is shown by the black arrow

Analytical Response for Electric and Magnetic Field

Potentials are purely mathematical entities that are introduced as a matter of convenience to ease computation of electromagnetic fields. The Hertz vector $\mathbf{\Pi}$ has long been used as a potential (Everett 1990); it is defined by

$$\mathbf{B} = \mu_0 \sigma \, \nabla \times \mathbf{\Pi} \tag{2.12}$$

$$\mathbf{E} = -i\omega\mu_0\sigma \, \mathbf{\Pi} \tag{2.13}$$

The derivation of the Hertz-vector solution for the electromagnetic field due to a point dipole source located over a plane-layered Earth is too lengthy to include in this dissertation but may be obtained from the author on request.

Finite Element Response

The details of the finite element implementation appear in Badea. et al. (2001). Here I outline construction and solution of the finite element linear system. The mesh parameters created by mesh generation module, and the conductivity and slab location information, is read in. The finite element matrix is then constructed. To do this, the tetrahedra associated with each pair of connected nodes are determined. From each pair, a 4x4 elemental submatrix is constructed. The complex elements of the submatrix are inner products (integrals) of basis functions and their spatial derivatives over the domain comprising the union of the volumes of tetrahedra common to each nodal pair. The 4x4

submatrix is inserted into the appropriate (row, column) location of the global finite element matrix. The latter is of dimension $4N$ x $4N$ where N is the number of interior nodes in the mesh. The four entries of a submatrix reflects the four unknowns that are to be solved on each node; namely, the three components of the magnetic vector potential **A** and the electric scalar potential ψ.

The source term of the finite element linear system is then constructed. The source is specified in terms of the analytic solution for the primary magnetic vector potential, evaluated at each node of the computational domain. The individual components of the source vector, which is the right-hand-side of the FE linear system, are formed as integrals of products over tetrahedra of the analytic solution and the relevant basis functions.

The finite-element linear system, once constructed, is solved using the iterative quasi-minimal residual (QMR) algorithm (Freund, 1992). The matrix is complex symmetric. Preconditioning by the diagonal Jacobi method is conducted in order to accelerate convergence (Newman, 1995). After solution of the preconditioned system, the matrix is rescaled to produce the final result. The unknowns are nodal values of the magnetic vector potential **A** and scalar electric potential ψ. The computed potentials at designated receiver locations are output as separate files for the primary, secondary and total responses. The total response is computed by adding the primary and secondary responses. The results are then sent to the post-processing routine (see below). The secondary-field solution vector is also output and used for visualizations of field patterns.

Post Processing

Following their computation, the primary, secondary and total potentials are output to separate files. There are two post-processing modules. The first uses the potentials at surface nodes to calculate the electric field that would be recorded by ideal, noise-free surface receivers placed inline with the source dipole moment or broadside at 90^0 to the dipole moment. The second module uses the total field potentials on all subsurface nodes to compute electric or magnetic field patterns throughout the modeling domain. This module enables visualizations to aid the interpretation of responses.

Surface Potentials

The post-processing modules read in the primary, secondary and total field surface potentials output by the finite element module. The potentials along the x-axis (inline) and y-axis (broadside) are used to compute the electric field responses. Also required are the potentials evaluated along the $y \pm \Delta x$ axes, where Δx corresponds to the distance between nodes in the x-direction. These values are needed for numerical differentiation of the potentials.

The electric field responses are computed at inline and broadside locations according to

$$E_x = i\omega \left(A_x + \frac{\partial \psi}{\partial x} \right) \qquad (2.14)$$

$$E_y = i\omega \left(A_y + \frac{\partial \psi}{\partial y} \right) \qquad (2.15)$$

The scalar electric potentials on the $y \pm \Delta x$ axes are used to compute the derivative $\partial \psi / \partial y$ in equation (2.15). Inline, the magnetic vector and scalar electric potentials are sorted along the x-axis using a straight insertion algorithm.

The components (E_x, E_y) are aligned parallel and perpendicular to the dipole moment, respectively. The reader should appreciate that the parallel component E_x can be computed at a broadside location and similarly the perpendicular component E_y can be computed at an inline location.

PLOTXY

The software package PLOTXY (Parker and Shure, 1988) is a command-line plotting program. I use it to plot the inline and broadside electric field amplitude [V/m] as a function of TX-RX offset.

Subsurface Potentials

To create visualizations of 2D field patterns, the magnetic vector and electric scalar potentials at all subsurface nodes are used. A least squares algorithm is used to perform the necessary differentiations to obtain the electromagnetic field components. Visualizations are made using a special-purpose Postscript-generating code.

CHAPTER III

MESH DESIGN & VALIDATION

To produce accurate CSEM responses, the finite-element mesh must be optimized. The original finite-element code (Badea, et al. 2001) used a cylindrical mesh since it was intended for well-logging applications. As more computing power becomes available, meshes can be refined to produce more accurate results. A mesh is refined by increasing its node density. In this work, the original mesh has been adapted to rectangular geometry. Such an adjustment allows for straightforward implementation of geologic and man-made features such as fault zones and a lateral wellbore. The cylindrical mesh geometry is also better suited to model the surface-based grounded-dipole CSEM configuration employed here. The software has previously been validated on known 1-D, 2-D, and 3-D problems. The rectangular-mesh version of the algorithm has been checked again by comparisons against previously published solutions in marine (Um and Alumbaugh 2007; Ward and Hohmann 1987; Weiss 2007) and terrestrial (Streich 2016) settings. These additional checks provide increased confidence in the results.

The values of three parameters prescribe the mesh. Firstly, the mesh dimensions are designated. Larger meshes tend to give more accurate results but also require additional computational memory and time. The size of the mesh must comply with available computational limitations. The second mesh design parameter is the aspect ratio of its lateral to vertical dimensions. This corresponds in the cylindrical case to the

ratio of mesh radius to its vertical extent. For the rectangular mesh the important ratio is lateral to vertical extent. After considerable testing, an aspect ratio of 2:1 was determined as it provided to best agreement against the aforementioned previously published solutions. The final parameter that can be varied to optimize mesh performance is the node density. There is again a trade-off between time, memory, and accuracy of responses. Denser node placement gives more accuracy; however, the relative improvement diminishes as the number of nodes increases.

Several diagnostics are available to evaluate the quality of the mesh. The simplest is a readout of each slab volume, the number of its constituent tetrahedra, and its bounding coordinates (see Table 1 for an example). This diagnostic allows the user to determine whether a slab has been correctly discretized and placed in the proper location within the mesh. Information regarding the total volume of the mesh, being the sum of the volumes of its constituent tetrahedra, also provides a helpful diagnostic check. Other control procedures for ensuring a good quality mesh are visualizations of 2- D cross sections and examination of quality-factor histograms (see previous chapter).

With reference to the geoelectrical models in Figure 10, in Figures 11 and 12, I show the validation of terrestrial-CSEM solutions computed on the rectangular mesh. The corresponding analytic solutions were published by Streich (2016). I have made further validations against other solutions, but the Streich (2016) case provides an illustrative, rigorous check. More accurate results may be achieved using a finer mesh.

(a)

Air $\sigma = 1\times10^{-8}\ S/m$

1-km   Sediment $\sigma = 0.5\ S/m$

100-m   Resistive Layer $\sigma = 0.033\ S/m$

Sediment $\sigma = 0.5\ S/m$

(b)

Air $\sigma = 1\times10^{-8}\ S/m$

1-km   Sediment $\sigma = 0.033\ S/m$

100-m   Conductive Layer $\sigma = 0.5\ S/m$

Sediment $\sigma = 0.033\ S/m$
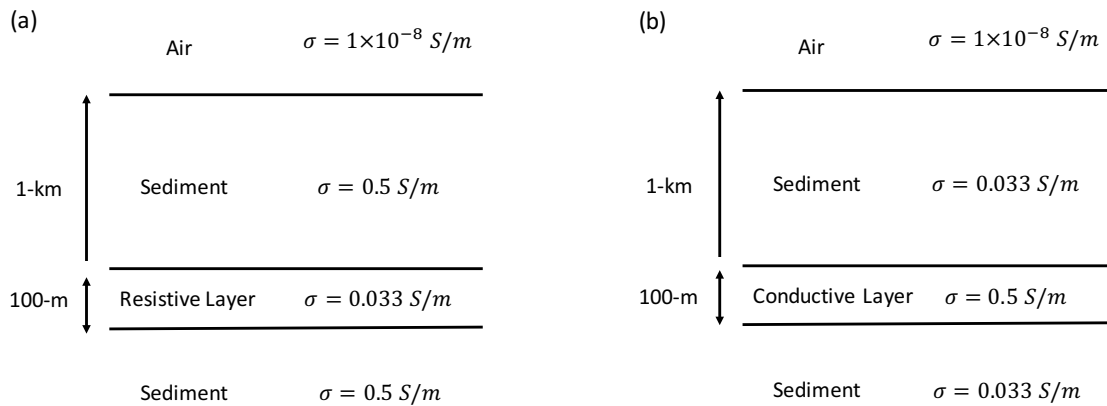
Figure 10 1-D geoelectrical models used to validate finite element solution (Streich, 2016)
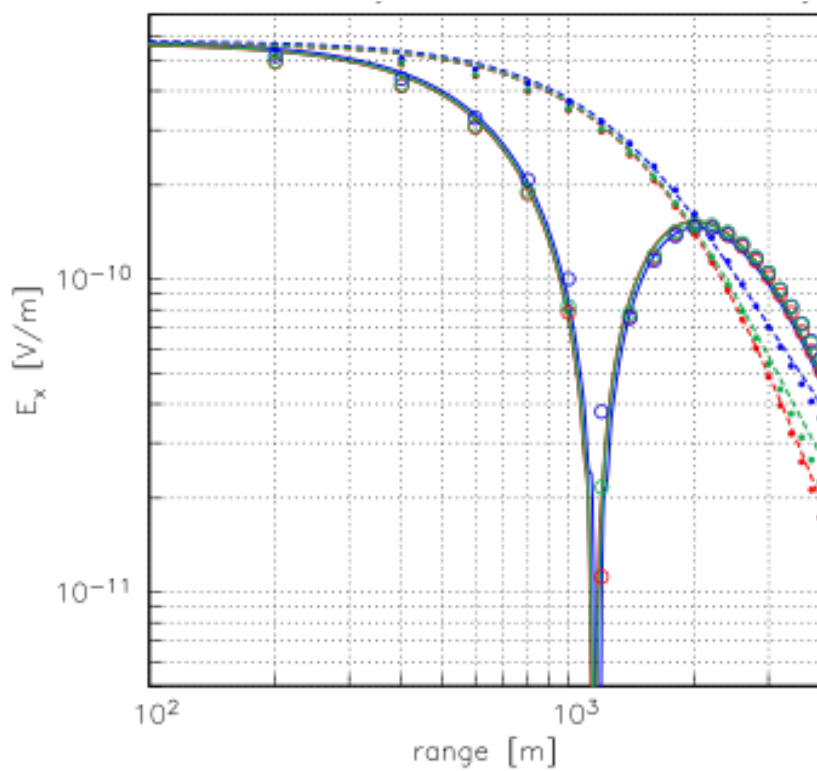
Figure 11 Validation of secondary electric field response for finite element (symbols) code against analytic solution (solid lines) for resistive layer geoelectrical model (a) given in Streich, 2016 at frequencies of 0.1 (blue), 0.5 (green) & 1-Hz (red)
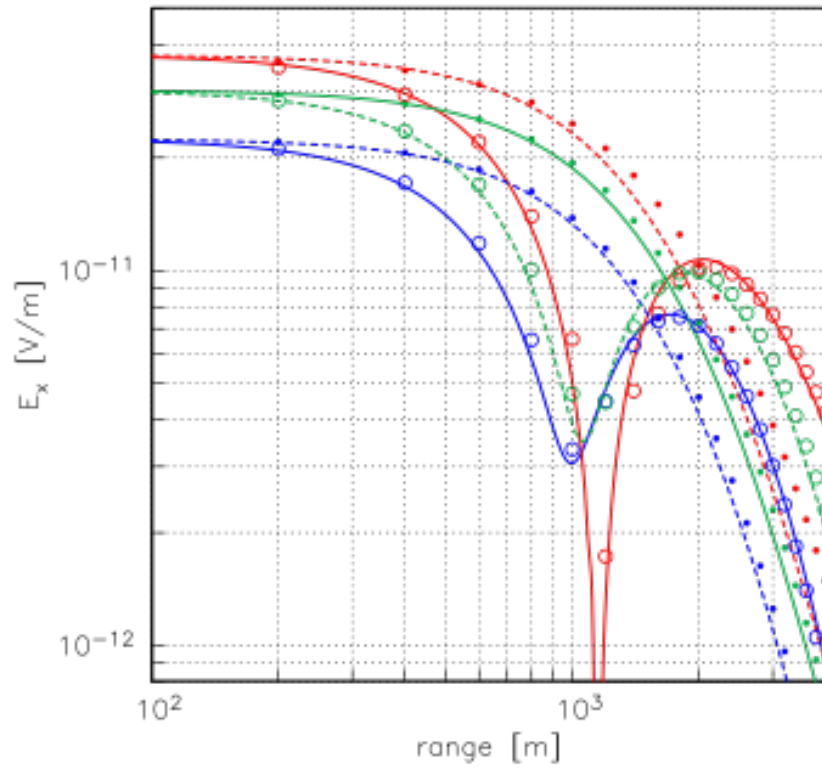
Figure 12 Validation of secondary electric field response for finite element (symbols) code against analytic solution (solid lines) for conductive layer geoelectrical model (a) given in Streich, 2016 at frequencies of 0.1 (blue), 0.5 (green) & 1-Hz (red)
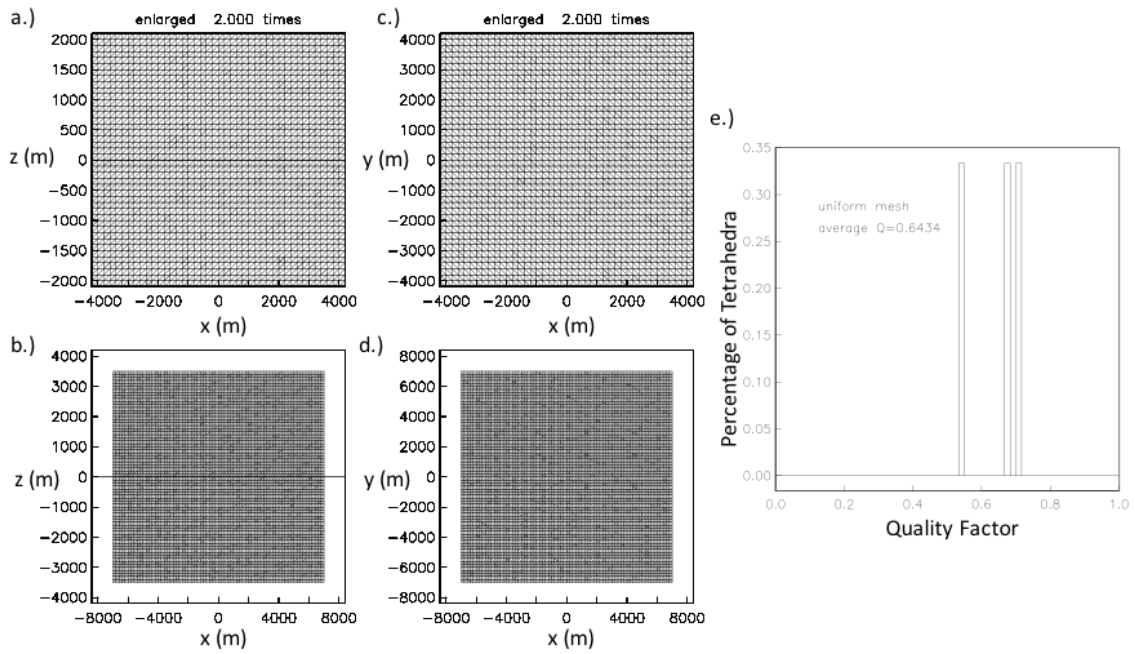
Figure 13 Mesh cross sections and quality factor histogram for mesh used to generate responses in figures 10a & 11. Enlarged mesh cross section through the x-z plane. b.) Full-scale cross section of mesh through the x-z plane. c.) Enlarged mesh cross section through the x-y plane. d.) Full-scale cross section of mesh through the x-y plane. e.) Quality factor histogram

Mesh Volume	1.00000000000467
Average Quality Factor	0.6434
Total Volume of Tetrahedra (m^3)	1.372E12
Air Tetrahedra	1029000
Sediment Tetrahedra	999600
Conductive/Resistive Layer Tetrahedra	29400
Min/Max Value in x for layer (m)	-7000/7000
Min/Max Value in y for layer (m)	-7000/7000
Min/Max Value in z for layer (m)	1000/1100

Table 1 Mesh diagnostics for mesh used to generate responses in figures 10 & 11

Local Mesh Refinement

It is supposed that controlled source electromagnetic (CSEM) responses are diagnostic mainly of a measure of the conductance of a highly-conductive target at depth, rather than separately on the target conductivity and its geometry. The transverse conductance C [units, Sm] of an elongated body, for example, is given by the product of its cross-sectional area A [m^2] and conductivity σ [S/m],

$$C = \sigma A \tag{3.1}$$

The transverse conductance formula (3.1) is investigated in this work as a means to assign an equivalent conductance to a wellbore or pipeline of prescribed conductivity and cross-sectional area. The advantages of locally refining the finite-element mesh in the vicinity of a long, straight, slender conductor such as a lateral wellbore buried at depth are also herein explored. While there are several methods available to evaluate the CSEM response of a wellbore or similar elongated conductor (e.g. Patzer *et al.* 2017;

Puzyrev *et al.* 2017), I use a sequence of local refinements of a coarse mesh, coupled with application of the formula (3.1), to model the response of a deeply-buried, small-diameter but highly conductive lateral wellbore.

Without local refinement, to maintain a practical computational size, the lateral and vertical mesh grid spacing must be kept larger than 400 and 100 m, respectively, to resolve CSEM responses at 1 Hz to depths of several km (see Figure 13). These grid spacing were determined by extensive tests of various mesh aspect ratios. Specifically, CSEM responses on various meshes were checked against the aforementioned previously published solutions. Computational memory limitations prohibit fine-scale global refinements of the mesh. The net result of the tests is that a wellbore of 400×100 m can be implemented on a $14 \times 14 \times 7$ km grid comprising 71 nodes in each of the lateral and vertical directions. The wellbore can be made smaller if local mesh refinement is used, as shown below.

We use the transverse conductance formula (3.1) to assign an appropriate conductance to a modeled wellbore of smaller diameter. An actual wellbore (Figure 14a) has diameter ~20 cm, wall thickness ~2 cm and conductivity ~5×10^6 S/m. However, for the wellbore that can be discretized without local refinement (400×100 m), equation (3.1) prescribes that a much lower conductivity of ~3 S/m (Figure 14b) should be used in the CSEM modelling. Note that the wellbores modelled in this paper are treated as solid, elongated prisms of small cross-section rather than cylindrical thin-walled annuli.
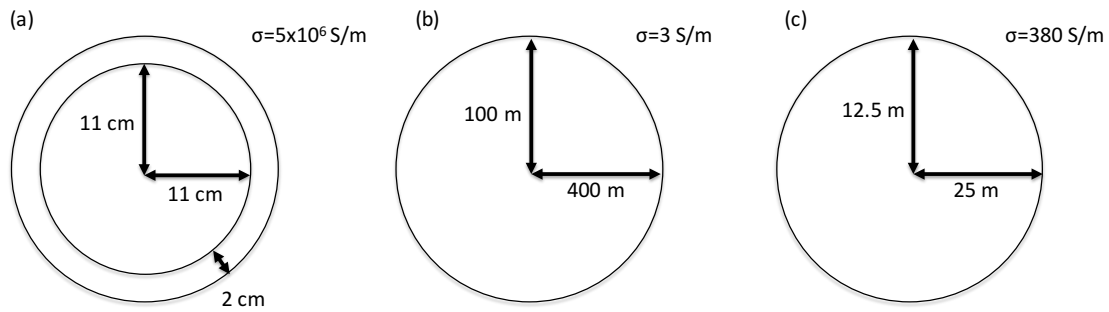
Figure 14 (a) Realistic wellbore cross-section for which without local refinement the wellbore (b) must be modelled, using the conductance equation to determine a suitable conductivity. With local refinement of the wellbore area option (c) can be modelled, a case considerably closer to our realistic case (a)

The finite-element-computed secondary inline electric-field response at both positive and negative TX-RX offsets is displayed in Figure 15. The lateral wellbore is buried beneath 2 km of sediment of conductivity 0.01 S/m and it is aligned with and located directly beneath the transmitter deployed at the surface. The responses at negative and positive offsets are similar but not identical. A further test was conducted to provide further confidence in mesh robustness. An 'upside-down' test, in which the geoelectrical model is reflected in the z-axis (Figure 15b), is compared to the original case (Figure 15a). This test produced a precise $x \rightarrow -x$ mirror symmetry (Figure 15c) in the responses at positive and negative receiver offsets. This test suggests that the asymmetry in responses at the positive and negative offsets is caused by the inherent

asymmetry of the tetrahedral mesh.
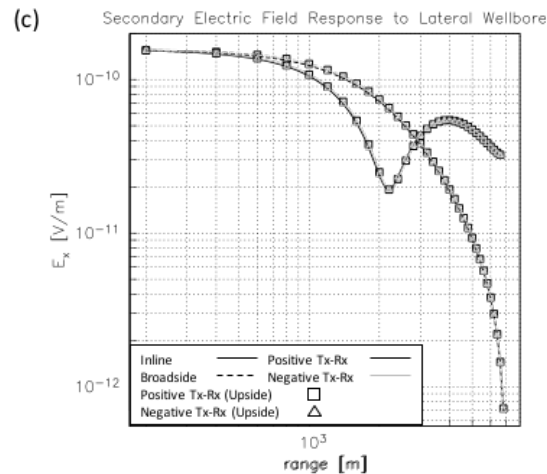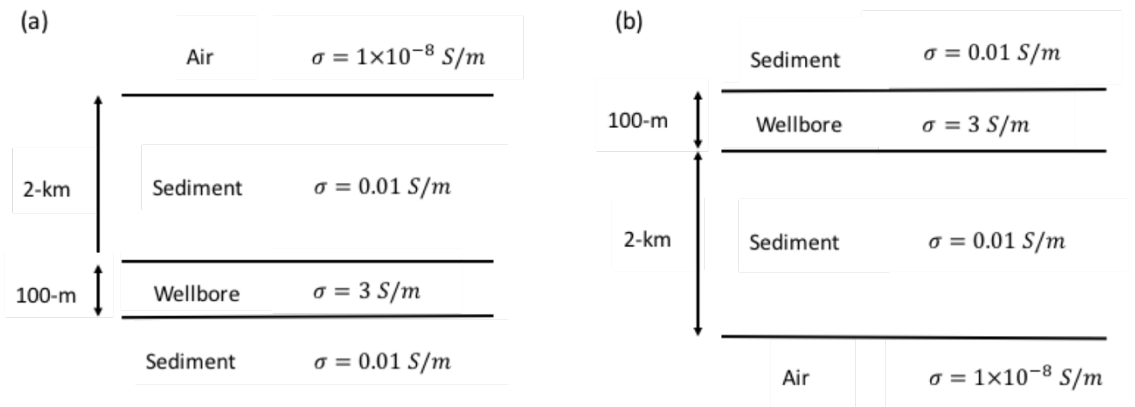
Figure 15 The secondary electric field response for the geoelectric model (a) is shown in (c) the inline (solid) and broadside (dashed) responses are shown for positive (black) and negative (grey) transmitter (TX) – receiver (RX) offsets. The same test is then repeated for geological model (b), where the secondary field responses are shown by squares (positive TX-RX offset) and triangles (negative TX-RX offset). This is termed the upside down test. The secondary field responses in both cases show a negligible difference between the positive and negative TX-RX offsets. This along with exact match between the normal and 'upside down' test responses provides increased confidence in mesh robustness

A local refinement of the finite element mesh allows a more realistically-sized wellbore to be modelled. For example, application of 5 nested local mesh refinements enables a wellbore size of ~25 × ~12.5-m to be modeled. In that case, a appropriate conductivity is ~380 S/m (Figure 14c). Further nested local mesh refinements are possible. There is a trade-off between the computational memory required to model a very slender structure against the marginal improvement in accuracy of the CSEM response. The number of nested refinements must respect computational memory and time constraints. Each refinement adds a substantial computational burden since it increases the dimension of the finite element linear system that must be solved. Small, highly conductive structures also degrade the conditioning of the finite element matrix, leading to longer times to solution convergence. The increased time and degradation in matrix conditioning does not permit modelling of realistically-sized wellbores on the computational resource available for this project.

Figure 16 indicates the secondary inline electric-field response for both positive and negative TX-RX offsets in the presence of a locally refined wellbore. The geoelectrical model is given in Figure 16a. The secondary inline and broadside electric field responses show similar shapes to the responses computed on a mesh without local refinement. The locally-refined responses do exhibit a noticeable reduction in amplitude. The differences in responses with and without local refinement indicates that the conductance formula (3.1) is not an exact method for replacing a slender, highly-conducting wellbore of realistic size with one of larger radius and lower conductivity. This point is discussed further in chapter 4.

36

(a)

	Air	$\sigma = 1{\times}10^{-8}\ S/m$
2-km	Sediment	$\sigma = 0.01\ S/m$
12.5-m	Wellbore	$\sigma = 380\ S/m$
	Sediment	$\sigma = 0.01\ S/m$

(b) Secondary Electric Field Response with Local Refinement

Legend:
- Inline (No Refinement) ———
- Broadside (No Refinement) - - -
- Positive Tx-Rx ———
- Negative Tx-Rx ———
- Inline (Refined) □
- Broadside (Refined) △
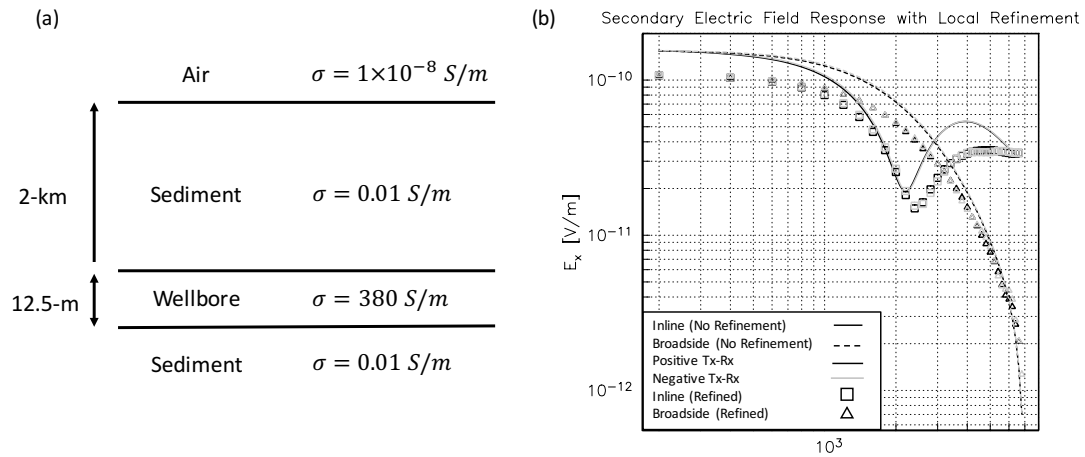
Figure 16 Following local refinement in the wellbore area, the geoelectrical model shown in (a) may now be used, this now utilizes a 25-m x 12.5-m cross section for the wellbore, the conductivity of the wellbore is computed via the conductance equation. The secondary electric field for cases with and without local refinement are shown in (b) as a function of TX-RX offset. The responses associated with a locally refined mesh are of lower amplitude and are likely more accurate given the increased realism to the wellbore size and shape achieved through local refinement

In summary, the modelled dimensions of the lateral wellbore, whilst made more realistic by local refinement, are still vastly greater than the dimensions of an actual wellbore. The local refinement algorithm is capable, in principle, of reducing the modelled wellbore to its actual size. However, such fine-scale discretization would require an excessively large amount of computing power. As computational power continues to be increased, the modelled lateral wellbore could be further refined in size. However attention must also be paid to the finite-element matrix conditioning, which degrades as the conductivity contrast increases between the lateral wellbore and host sediments.

CHAPTER IV

CAPABILITIES & LIMITATIONS OF THE TRANSVERSE CONDUCTANCE

ARGUMENT

In most cases, and certainly if computational resources are scarce, memory and

processing speed must be considered when building and discretizing a geoelectrical

model in order to compute its CSEM response. The discretization of slender highly-

conducting bodies, in particular, requires local mesh refinement. Local refinement

introduces additional degrees of freedom into the finite-element linear system, and hence

more computational power is required to solve the resulting equations.

I have investigated a method to account for slender bodies in CSEM modeling,

without introducing excessive numbers of degrees of freedom. Consider the conductance

equation (Hibbs, 2015)

$$C = \sigma A \tag{4.1}$$

The transverse conductance C [units, Sm] of an elongated body is the product of

its cross-sectional area A [m^2] and conductivity σ [S/m]. The formula (4.1) is used herein

to assign an appropriate equivalent conductance to a slender body of prescribed

conductivity and cross-sectional area, as noted in chapter 3. This prescription can be

applied to a lateral wellbore, for example. It is presumed that CSEM responses are

diagnostic mainly of the conductance of a highly-conductive target at depth, rather than

separately on the target conductivity and its geometry. This argument applies exactly to

1-D plane-layered solutions, particularly at low frequencies, but it has not been

rigorously tested on problems involving 2-D and 3-D structures.

Here, a conductance argument is applied to a realistic wellbore of radius 11 cm

and conductivity 5×10^6 S/m. I consider several "equivalent" larger wellbores of radii

25, 50 and 100 m and corresponding conductivities 48, 12 and 3 S/m. If the conductance

argument applies exactly, then the secondary electric field responses from each of the

equivalent lateral wellbores should be equal.
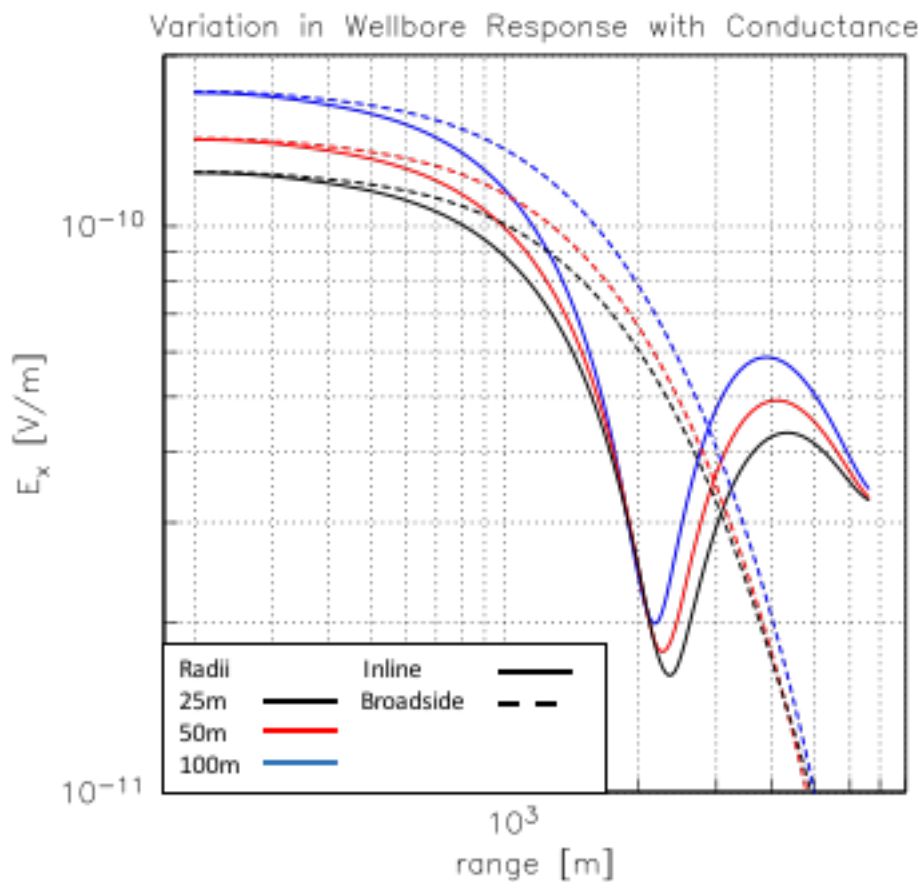
Figure 17 Variation in wellbore response for 3 wellbore of equal conductance

Figure 17 displays the secondary inline and broadside responses from each equivalent wellbore. The wellbores are buried at 2 km depth in a homogeneous halfspace of conductivity 0.01 S/m. Though the responses have a similar shape, they are not equal. Nevertheless, the different responses may be used to understand the "generic" wellbore response. The inline responses provide consistent and useful information on the burial depth, for example, since the location of the minimum corresponds approximately to the wellbore burial depth. Also, a smaller-radius wellbore has a lower amplitude than a larger-radius wellbore. Thus, it is expected that the actual response from a 'realistic' wellbore would be of considerably lower amplitude than those shown in the figure; however, the response should maintain a similar shape and preserve information regarding burial depth.

To determine whether the differences in the equivalent-wellbore responses could be tied to a specific model parameter, such as cross-sectional area, I sought a constant scaling factor that would equalize the wellbore responses. The study was conducted on both secondary and total in-line responses. It became clear that a constant scaling factor is not sufficient to equalize the responses of the lateral wellbores. Upon further investigation, it turned out that piecewise scaling functions with respect to TX-RX offset are required. To illustrate this, the responses are divided into four sections, where x=TX-RX offset and d=wellbore burial depth: (1) $x < 0$ and $|x| > d$; (2) $x < 0$ and $|x| < d$; (3) $x > 0$ and $|x| > d$; (4) $x > 0$ and $|x| < d$.
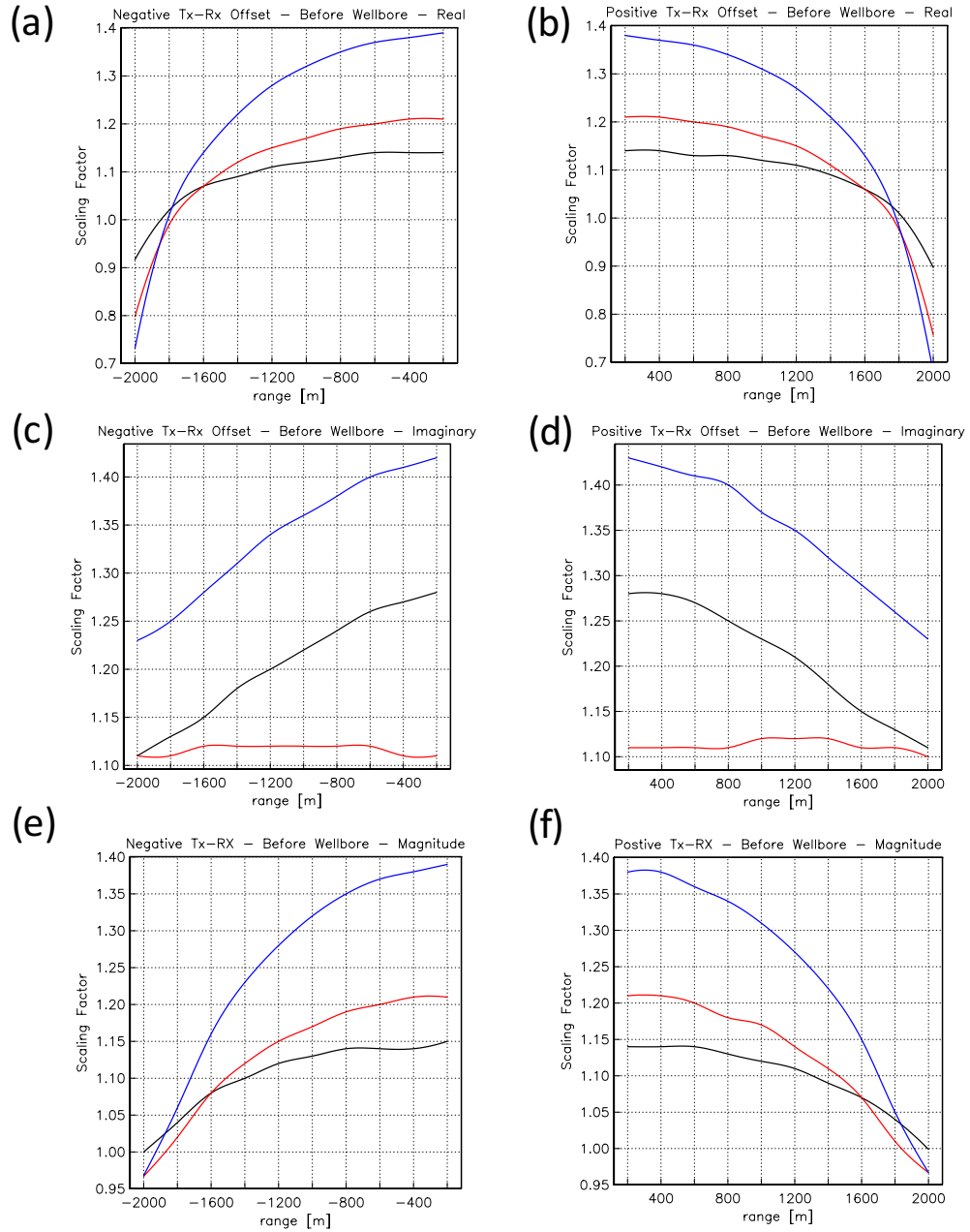
Figure 18 **Secondary field scaling factor vs TX-RX offset to compare wellbore of radii 25 to 50m (black), 50 to 100m (red) and 25 to 100m (blue) for cases where x<0 and |x|<d (a,c,e) and where x>0 and |x|<d (b,d,f). Scaling factors are shown for the real (a,b) and imaginary (c,d) components as well as the magnitude (e,f)**
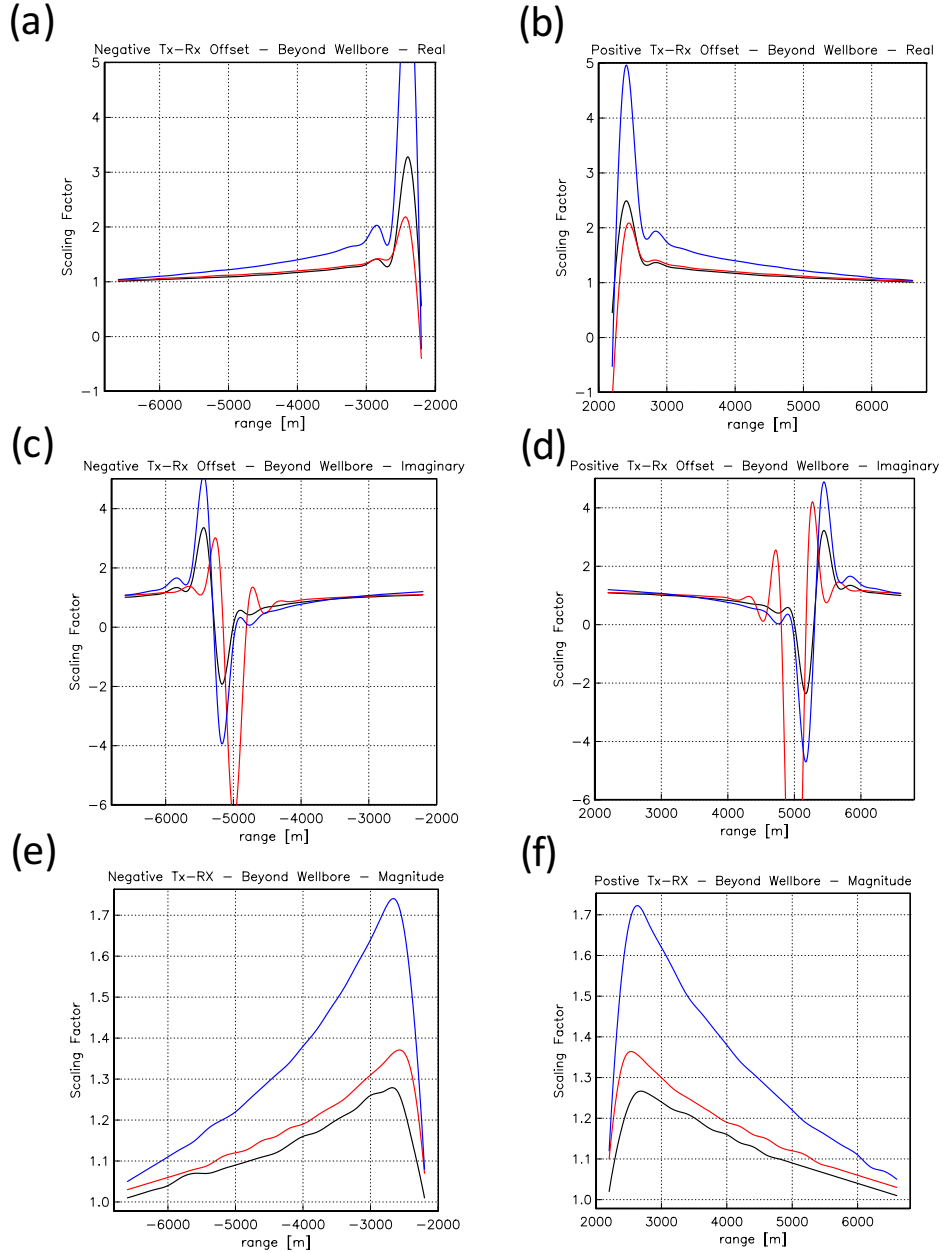
Figure 19 Secondary field scaling factor vs TX-RX offset to compare wellbore of radii 25 to 50m (black), 50 to 100m (red) and 25 to 100m (blue) for cases where x<0 and |x|>d (a,c,e) and where x>0 and |x|>d (b,d,f). Scaling factors are shown for the real (a,b) and imaginary (c,d) components as well as the magnitude (e,f)

Figure 18 shows that the required scaling factors, as functions of TX-RX offset, are symmetrical around the transmitter at $x = 0$ for cases where $|x| < d$. Figure 19 shows a similar pattern for cases $|x| > d$. Evidently the required scaling for the examples shown here is not a simple relationship. A similar experiment was carried out using the total response. Figures 20 and 21 indicates that the scaling functions are even more complicated. Again there is a symmetry around the transmitter for both regions $|x| < d$ and $|x| > d$. Nevertheless, the overall result of the search is that a simple scaling factor, or function, cannot be found such that the conductance argument in (4.1) can be applied to deduce the response of a realistic wellbore based on an equivalence to computationally-tractable ones of larger wellbores.
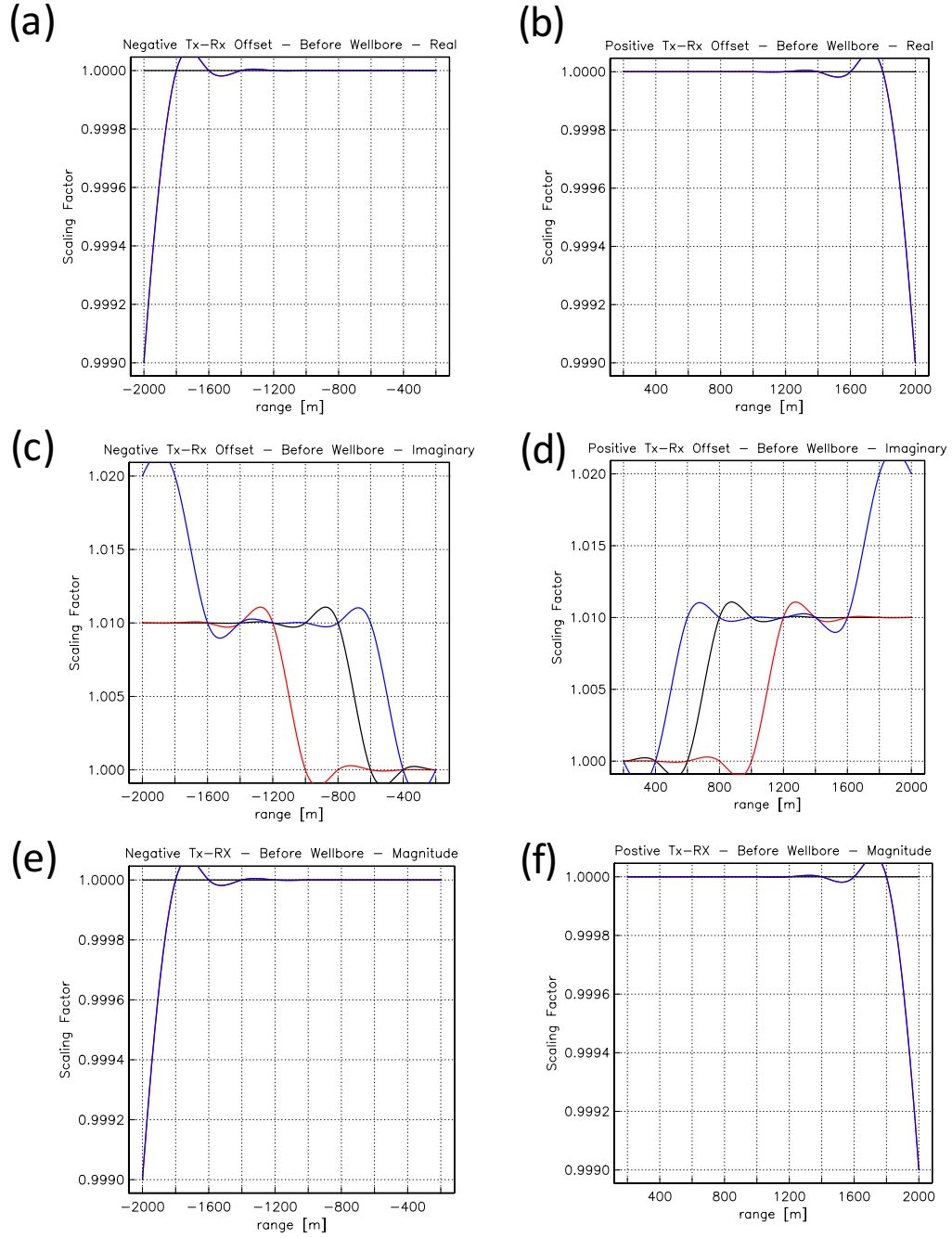
Figure 20 Total field scaling factor vs TX-RX offset to compare wellbore of radii 25 to 50m (black), 50 to 100m (red) and 25 to 100m (blue) for cases where x<0 and |x|<d (a,c,e) and where x>0 and |x|<d (b,d,f). Scaling factors are shown for the real (a,b) and imaginary (c,d) components as well as the magnitude (e,f)

44
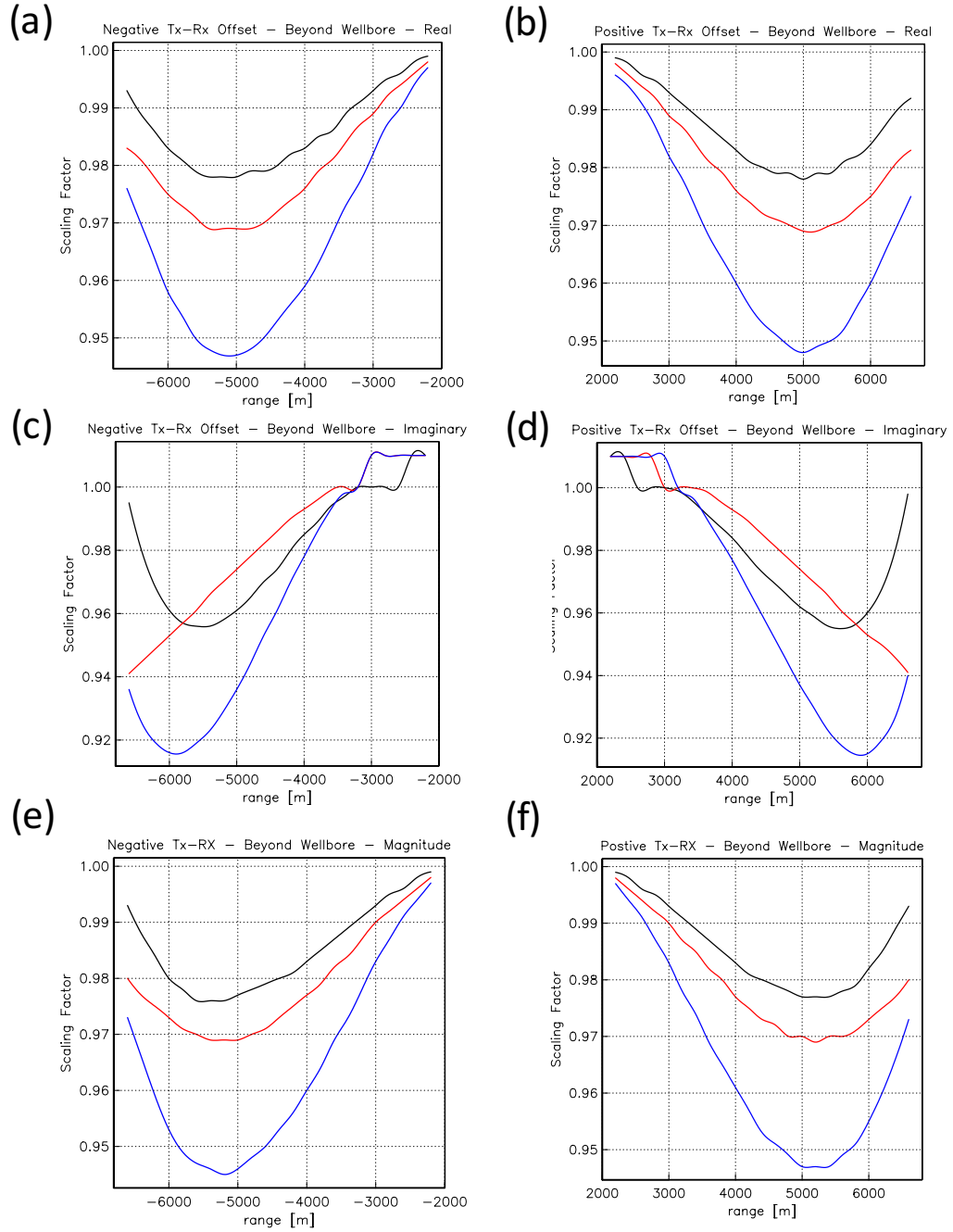
Figure 21 Total field scaling factor vs TX-RX offset to compare wellbore of radii 25 to 50m (black), 50 to 100m (red) and 25 to 100m (blue) for cases where x<0 and |x|>d (a,c,e) and where x>0 and |x|>d (b,d,f). Scaling factors are shown for the real (a,b) and imaginary (c,d) components as well as the magnitude (e,f)
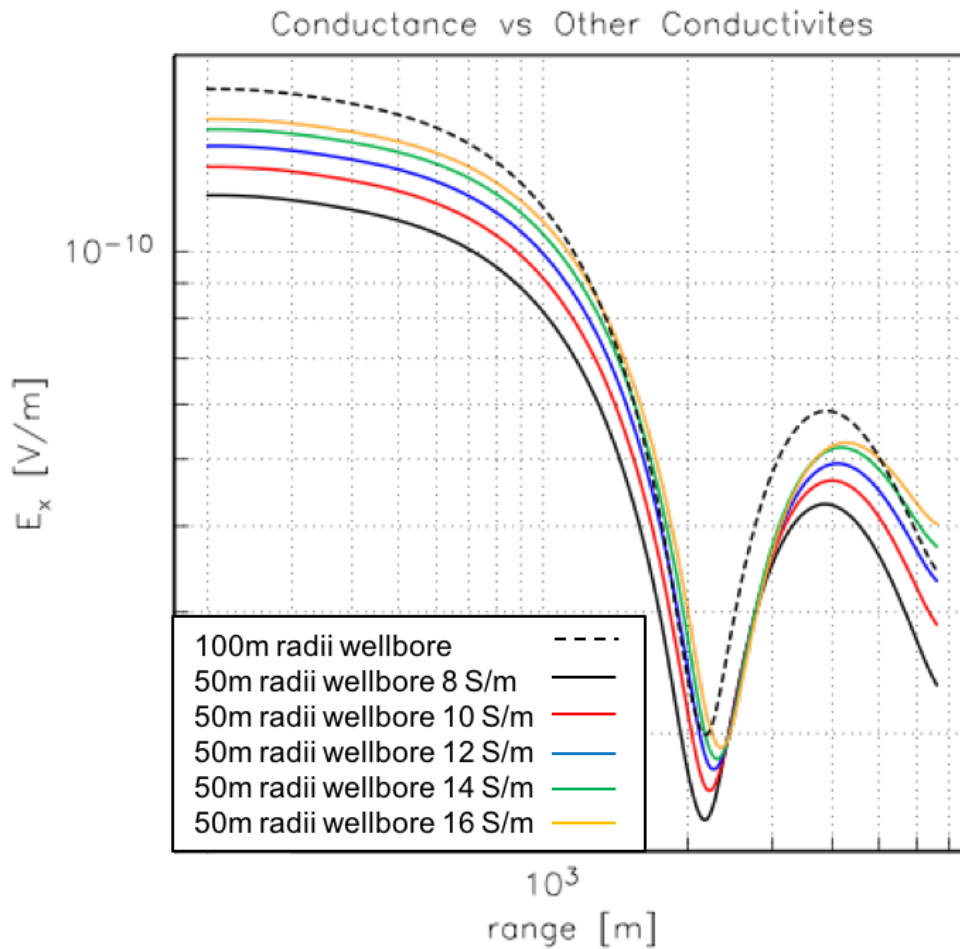
Figure 22 Attempts to match a 50m radii wellbore (solid) to a 100m radii wellbore (dashed) for secondary inline electric field., where 12 S/m represents the conductivity calculated using the conductance argument

The conductance argument, if it were applicable, would have provided a computationally-feasible approach to obtain the otherwise intractable response of a long slender body, such as a wellbore or pipeline. Figures 17 does demonstrate that the shapes of the secondary responses are similar for the three equivalent wellbores. Burial depth can be estimated with reasonable accuracy.

The preceding investigation begs the following question. How are the different "equivalent" responses related to each other? To address this question, different conductivities were assigned to a 50-m-radius wellbore and their responses are compared to the original 100-m-radius wellbore response. Figure 22 demonstrates that a 50-m-radius wellbore, assigned the conductivity (12 S/m) determined by the conductance formula (4.1), does not produce the closest match to the 100-m wellbore. A better fit is a 50-m wellbore of conductivity 16 S/m. This result shows that the conductance formula, while still useful, cannot be strictly applied to the modest goal of predicting the response of a 50-m wellbore from the response of a 100-m one.

To summarize, I have found that the position of the inline-response minimum varies only slightly with the dimension of the "equivalent" wellbore. The conductance argument does not however produce consistent amplitudes. Larger bodies (assigned lower conductivities) produce larger-amplitude responses that their smaller (assigned to be more conductive) counterparts.

As a practical matter, this result should be taken into account in situations where the signal-to-noise ratio is low. A conductance argument, based on computed responses of a larger-than-realistic body, may suggest that a deeply buried target is detectable, when in fact the amplitude of the actual target could fall below the detection threshold.

The conductance argument remains a useful tool for approximating responses from bodies that may not be modelled due to constraints in computational power. Also, numerical instability of the FE linear system solver may occur under very high conductivity contrasts, such that computing the responses of realistically small, highly-

conducting bodies may be intractable with the algorithm used. Local mesh refinement

(chapter 3) should be used to discretize an object as closely as possible to its actual size.

However, it must be kept in mind that large conductivity contrasts can generate

instabilities while solving the finite element linear equations.

CHAPTER V

FEM RESPONSES TO LATERAL WELLBORE AND FLUID-FILLED FRACTURE

ZONES

This work presents highly idealized simulations of terrestrial CSEM responses

caused by injection of fluids associated with hydraulic stimulation of unconventional

reservoirs. The eventual aim of work along these lines is to investigate whether

hydraulic fracture fluids can be identified based on their CSEM signature and, insofar as

possible, to infer gross details of the subsurface flow pathways.

A finite element (FE) algorithm based on Badea et al. (2001) is used to compute

terrestrial CSEM responses. The original purpose of the FE code was to study well-

logging responses, consequently a cylindrical mesh geometry was used. The mesh has

been modified in this study to rectangular geometry. Geological and other anomalous

structures in the subsurface may be specified by assigning dimensions and conductivities

to slab-like bodies. The modified algorithm has been checked by comparing numerical

results to previously published solutions in marine (Um and Alumbaugh 2007; Ward and

Hohmann 1987; Weiss 2007) and terrestrial (Streich 2016) settings. In particular, the

two geoelectrical models shown in Figure 23 are used as test scenarios including a

resistive and conductive layer, respectively. The good agreement shown in Figures 24

and 25 between the results and the analytically-derived solutions for the terrestrial case

in Streich (2016) provides confidence in the FE-computed terrestrial CSEM responses.

49

Here I explore the potential of using the terrestrial CSEM method for detection of subsurface conductive fluids associated with hydraulic fracturing. A first step in this direction is accomplished here by modelling CSEM responses of highly idealized scenarios that incorporate electrically conductive fluids adjacent to a lateral wellbore.

Furthermore I discuss mesh generation techniques that have been developed to discretize a slender, highly-conductive lateral wellbore. The fine meshing of a slender structure is accomplished through local refinements of an initially-coarse rectangular mesh, while conductivity is assigned using an equivalent conductance formula (4.1). The limitations of the equivalent conductance formula have been discussed in the previous chapter. The effect on terrestrial CSEM responses of host sediment conductivity variations is also investigated in this chapter.

For all modelling scenarios, both broadside and inline CSEM responses are evaluated. Inline profiles are those in which receivers are placed along a line on Earth's surface that is parallel to the dipole moment of the transmitter and contains the transmitter. Broadside profiles are those in which receivers are placed along a line on Earth's surface that is perpendicular to the dipole moment of the transmitter and contains the transmitter. The transmitter is modelled as a point electric dipole of moment of 1 A-m operating at frequency 1 Hz. Future improvements to this work will accommodate the finite-length grounded-wire dipole source sometimes used in field studies. The finite-length source allows a larger transmitter moment, which improves the signal to noise ratio of the measured subsurface response.

(a)

Air $\sigma = 1 \times 10^{-8} \ S/m$

1-km

Sediment $\sigma = 0.5 \ S/m$

100-m Resistive Layer $\sigma = 0.033 \ S/m$

Sediment $\sigma = 0.5 \ S/m$

(b)

Air $\sigma = 1 \times 10^{-8} \ S/m$

1-km

Sediment $\sigma = 0.033 \ S/m$

100-m Conductive Layer $\sigma = 0.5 \ S/m$

Sediment $\sigma = 0.033 \ S/m$
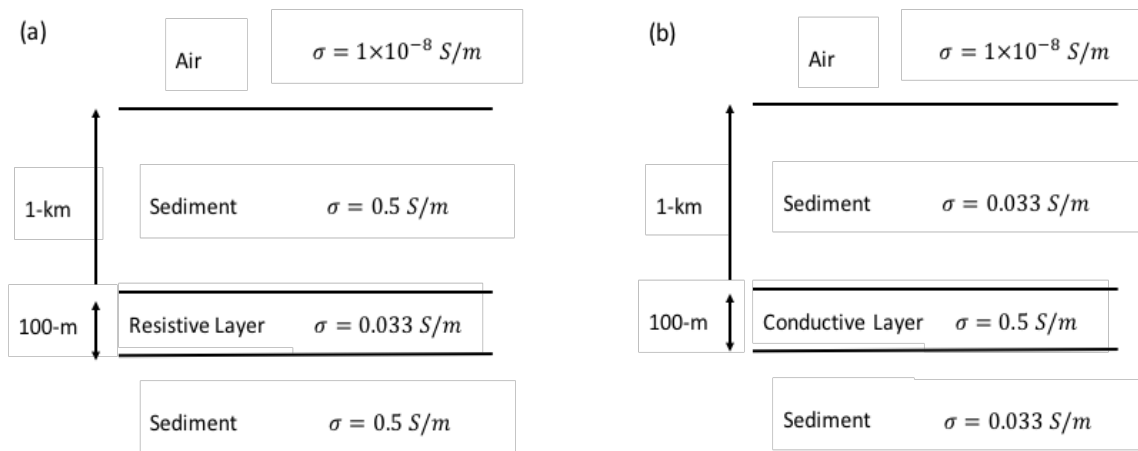
Figure 23 1-D geoelectrical models used to validate finite element solution (Streich, 2016)
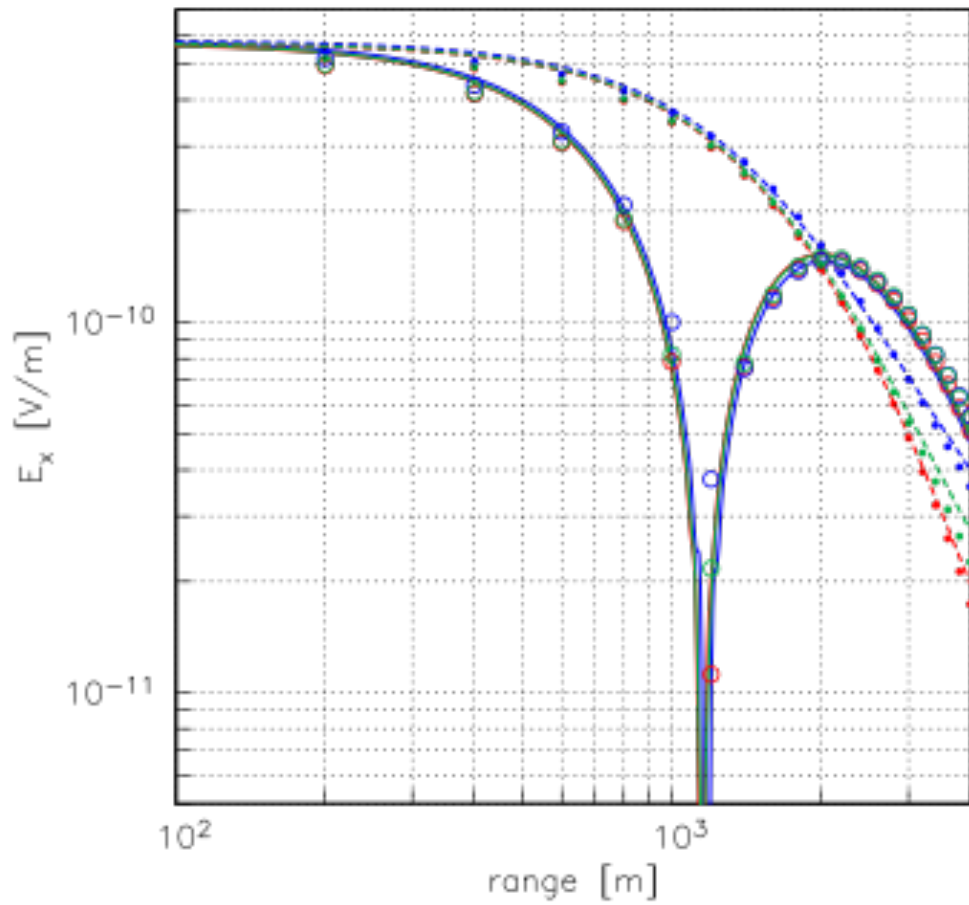
Figure 24 Validation of secondary electric field response for finite element (symbols) code against analytic solution (solid lines) for resistive layer geoelectrical model (a) given in Streich, 2016 at frequencies of 0.1 (blue), 0.5 (green) & 1-Hz (red)
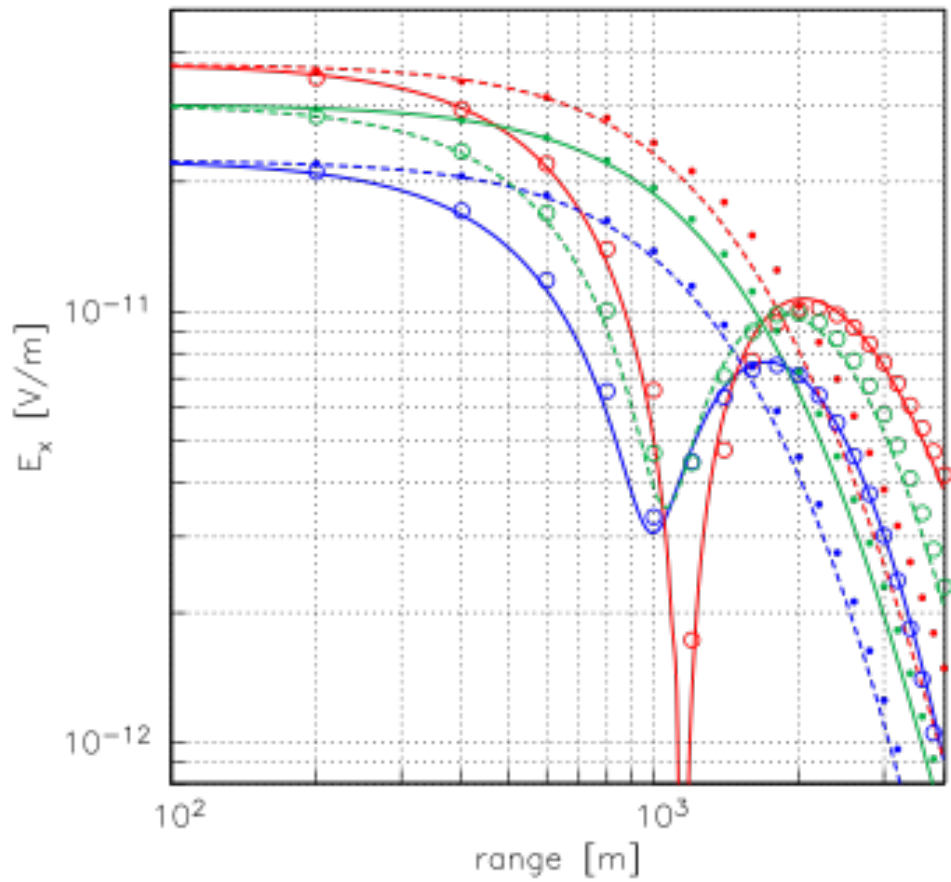
Figure 25 Validation of secondary electric field response for finite element (symbols) code against analytic solution (solid lines) for conductive layer geoelectrical model (a) given in Streich, 2016 at frequencies of 0.1 (blue), 0.5 (green) & 1-Hz (red)

Lateral Wellbore Responses

In order to understand controlled-source electromagnetic (CSEM) responses of hydraulic fracturing scenarios, it is important to study signals observed at different receiver locations. For example, the inline and broadside responses, as a function of TX-RX offset, for variable lateral-wellbore burial depths (0.5-3.0 km) are displayed in Figure 26.

The inline responses show more signal variability along the profile compared to the broadside responses. The former display a different shape for all burial depths and include a local minimum at offsets just beyond the depth of wellbore burial. The minima are followed by local maxima at larger ranges. Broadside responses show a greater amplitude at low to mid ranges; but at higher ranges, inline responses have the greater amplitude. All broadside responses have essentially the same shape. These observations indicate that inline responses are more sensitive than their broadside counterparts to the presence of steel casing.

Both the inline and broadside responses decrease in amplitude for increasing wellbore burial depth. This effect is due to the attenuation of electromagnetic signals traversing the vertical distance to the surface from the buried wellbore. Broadside responses show an increased negative gradient vs TX-RX offset for decreasing wellbore burial depth but, in general, broadside responses provide only limited information on the depth of a lateral wellbore at large TX-RX offsets. The inline responses however show a

54

significant shift in the local minimum to greater TX-RX offsets with increasing wellbore

burial depth. The variation is diagnostic of the burial depth of the lateral wellbore.

(a)

	Air	$\sigma = 1\times10^{-8} \; S/m$
w_d	Sediment	$\sigma = 0.01 \; S/m$
12.5-m	Casing	$\sigma = 380 \; S/m$
	Sediment	$\sigma = 0.01 \; S/m$

(b) Responses from Steel Casing at Various Depths
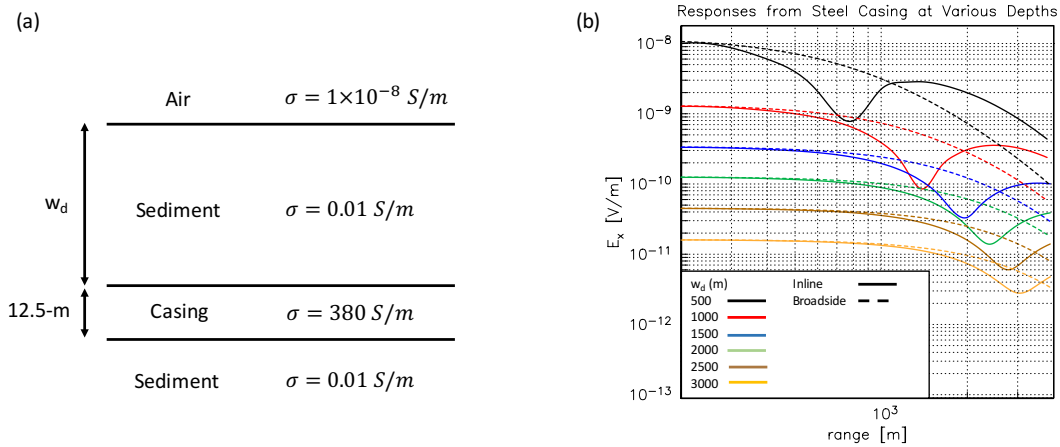
Figure 26 Secondary electric field responses for various lateral wellbore depths (b), with the inline (solid) and broadside (dashed) responses. The geoelectrical model (a) shows a casing buried at various depths w_d. Increased wellbore depth corresponds to a lower amplitude inline and broadside responses, with amplitude troughs being recorded at larger TX –RX offsets

Detection of Fluid-Filled Fracture Zones

A second component of an idealized hydraulic fracturing scenario is a fluid-filled

fracture zone. Figures 27a and 27b illustrate a scenario comprising a $200 \times 187.5 \times$

12.5-m fracture zone located at distance x_f from the transmitter on the x-axis and offset

in the y-direction by 12.5-m from the positive x-axis. The y-direction offset is intended

to leave space for the addition of a lateral wellbore, the modelling of which is discussed

later. The fracture zone has conductivity 0.32 S/m computed using the conductance

formula (4.1). The modelled fracture zone is equivalent to a fracture zone of the same

lateral dimensions, but 40-mm thick and containing 1.5×10^7 L of fluid of conductivity of 20 S/m.

Figure 27c shows the inline and broadside secondary electric-field responses for models with various x_f-values ranging from 2000 to 2800 m. Inline responses again show an increased signal variability along the profile compared to the broadside responses and also have a distinct shape comprising a local minimum followed by a local maximum. The position of the local minimum is sensitive to x_{ff}, suggesting that inline responses are diagnostic of the lateral position of the fluid-filled fracture zone. As x_f is increased, there is a concomitant shift in the position of the local minimum and maximum to greater TX-RX offsets.

The broadside responses show increased amplitudes compared to their inline counterparts for both small TX-RX offsets and those near the local minimum of the inline responses. Differentiating between broadside responses for different values of x_f however is challenging, especially at large offsets. Hence, a broadside response provides little information regarding the lateral location of a fluid-filled fracture zone.

The previous results are extended by incorporating a second fluid-filled fracture zone on the opposite side of the x-axis. The geoelectrical model is shown in Figure 28a. The two fracture zones have the same properties as the one shown in Figure 27a. Both inline and broadside responses (Figure 28b) are similar to those caused by the single fluid-filled fracture zone, however there is a slight increase in amplitude associated with the inclusion of the second zone. Thus it is difficult to discern, based on purely inline or

56

broadside measurements from a point-dipole transmitter, in which direction fluid flows

from the lateral wellbore.
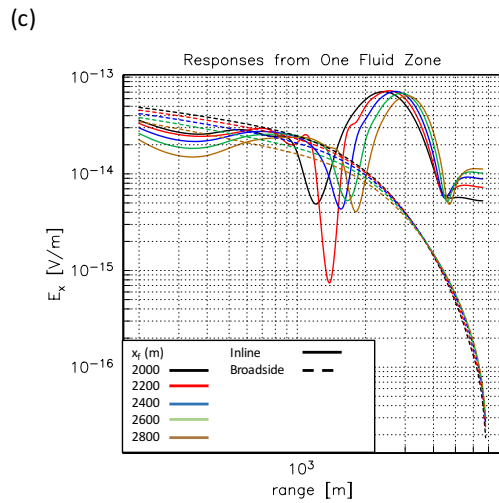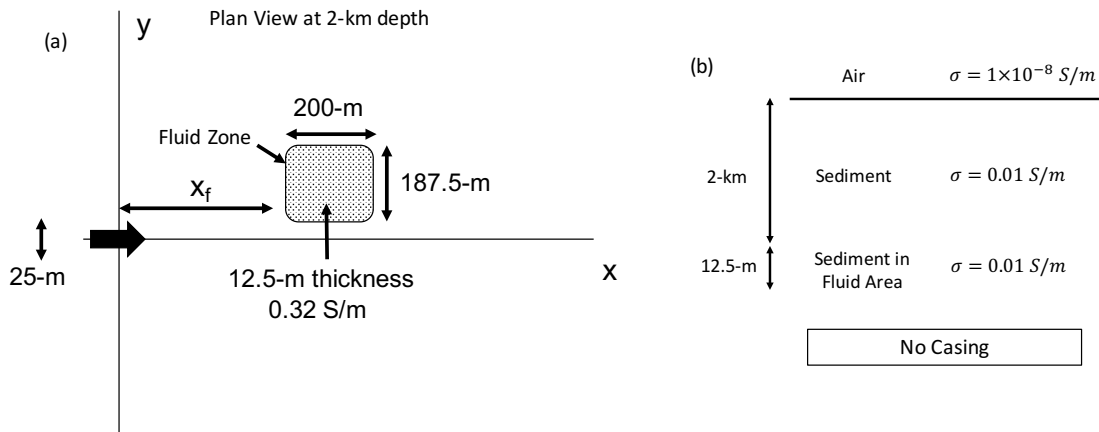
Figure 27 (a) shows a plan view at 2-km depth, at which we have a fluid-filled fracture zone of dimensions 200 x 187.5 x 12.5-m. The fluid filled fracture zone has a conductance which matches that of a 40mm thick fracture zone of the same lateral dimensions. Here we simulate the secondary electric field response from the fracture zone for various transmitter – fluid offsets (x_f). The geoelectric model for this scenario is shown in (b) whilst (c) shows the inline (solid) and broadside (dashed) responses. Responses are more dramatic in the inline direction and show a reduced TX – RX offset for peak amplitude for reduced offsets x_f. The response from the fracture zone is distinct and consistent across multiple x_f offsets

(a)

y   Plan View at 2-km depth

200-m

Fluid Zone

x_f

187.5-m

25-m

x

12.5-m thickness
0.32 S/m

(b)

Responses from Two Fluid Zones

E_x [V/m]

x_f (m)	Inline	Broadside
2000		
2200		
2400		
2600		
2800		

range [m]
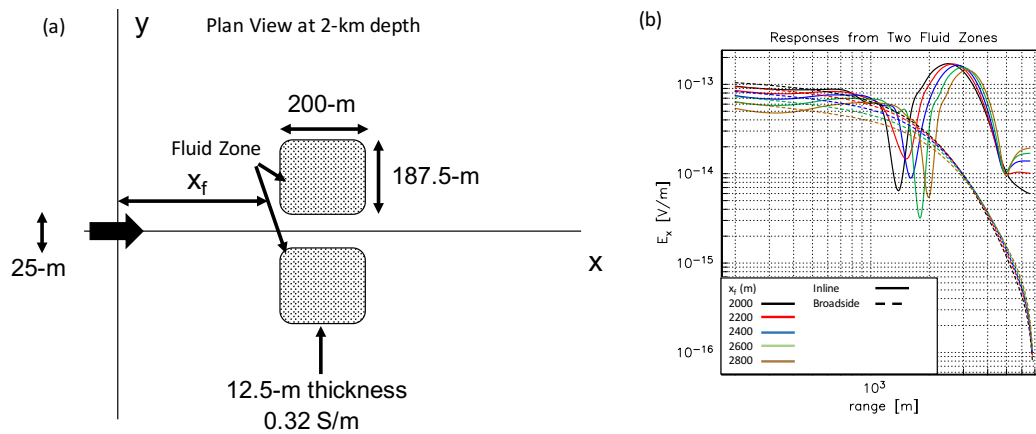
Figure 28 (a) shows a plan view at 2-km depth, at which we have two fluid filled fracture zones of the same dimensions as in figure 27 on either side of the x-axis. The geoelectric model for this scenario is that of 27b; two fluid-filled fracture zones are now included. (b) shows the inline (solid) and broadside (dashed) secondary electric field responses. Responses continue to be more dramatic in the inline direction and show similar trends to cases with a single fracture zone

Host Sediment Conductivity

In the previous sections, CSEM responses were evaluated from models in which fluid-filled fracture zones are buried beneath 2 km of sediment of conductivity 0.01 S/m. The latter value is commonly associated with terrigenous sediments. A host conductivity of 0.1 S/m was also tested to represent clays or marine sediments. Figure 29 shows the difference, due to the host conductivity, in the responses of the two fluid-filled fracture zones described in Figure 28a. The zones are located x_f=2200 m from the transmitter and the response curves correspond to cases where the overburden conductivity is either 0.01 S/m (terrigenous sediment) or 0.1 S/m (marine sediment).

The amplitude of the inline and broadside responses is ~100 times larger for terrestrial sands compared to the responses for clay overburden. Thus, host sediment

59

conductivity should play an important role in determining the ability of the CSEM technique to detect a fluid-filled fracture zone. A reduction in the signal variability of inline responses for a clay overburden is evident, compared to that of the terrestrial sediment overburden. This makes the identification of local minima and maxima more challenging in clays, and the local minimum no longer corresponds to the distance x_f. The inline response amplitude is also considerably greater than that of the broadside response for the clay overburden case at all ranges. In previous scenarios, the broadside response had slightly larger amplitudes at short transmitter-receiver offsets.

The differences between the responses for different values of host sediment conductivity shows that information about the enclosing geological formation is one key to understanding CSEM hydraulic fracture monitoring. An increase in the secondary electric field amplitude may be misinterpreted as a greater or lesser volume of fluid if the host sediment conductivity is not accurately captured in the simulation. In clay-rich sediments, fluid-filled fracture zones are considerably more difficult to detect than those located in terrestrial sediments. The difficulty with clay sediments is exacerbated in the presence of ambient oilfield electromagnetic noise level. A more powerful transmitter would be required when working in clay-rich environments to combat noise contamination. Effects of electrical anisotropy of the host formation are also potentially very important but an evaluation of them is outside the scope of this study.

Variation With Host Sediment Conductivity
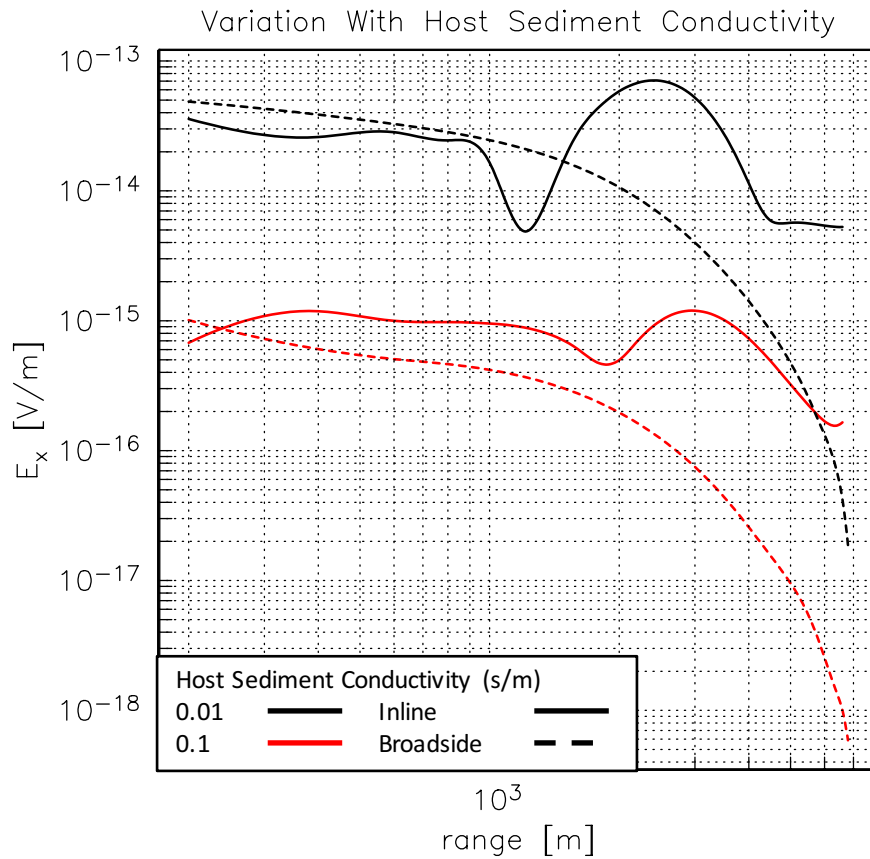
Figure 29 Variation in the host sediment conductivity has a profound impact on the secondary electric field response. For a host sediment conductivity of 0.1-S/m, there is a reduction in the amplitude of both the inline and broadside responses, as well as a reduction in the magnitude of change for inline responses compared to cases with a host sediment conductivity of 0.01- s/m

Fluid-Filled Fracture Zone Detection with Presence of Lateral Wellbore

Next we combine a single fluid-filled fracture zone from the previous scenario

with a locally refined lateral wellbore. This combination generates the geoelectrical

model portrayed in Figure 30. The lateral wellbore, of conductivity 380 S/m and radius

12.5 m, is located next to the fluid-filled fracture zone at 2 km depth. The overburden conductivity is 0.01 S/m.

Figure 30c shows the inline and broadside secondary electric-field responses for various values of the x_f parameter ranging from 2000 to 2800 m. The responses correspond to the combined fracture-zone/wellbore system. The responses are dominated by the wellbore, due to its much larger conductivity, whereas the effect of fluid in the fracture zones is not obvious. There is no discernible pattern in either the inline or broadside responses for variations in the fluid-zone location. As previously shown, the presence of the lateral wellbore is clearly indicated by the local minimum at 2.2 km in the inline response, whilst the broadside response provides much less diagnostic information. The complex nature of the responses is likely due to mutual inductance between the fluid zones and lateral wellbore.

Further investigation into the effects of mutual inductance is shown in Figure 31, where the fluid zone is now physically separated from the wellbore. If the wellbore-fluid coupling was purely galvanic I would expect a near-zero amplitude related to the fluid, however a reduced but non-zero amplitude is present. This suggests a strong inductive coupling since wellbore and fluid are not in direct contact. This test does not show that the response complications are purely due to inductive effects as there should be some galvanic coupling between the wellbore and fluid zone through the intervening geological medium (Cuevas, 2018) .
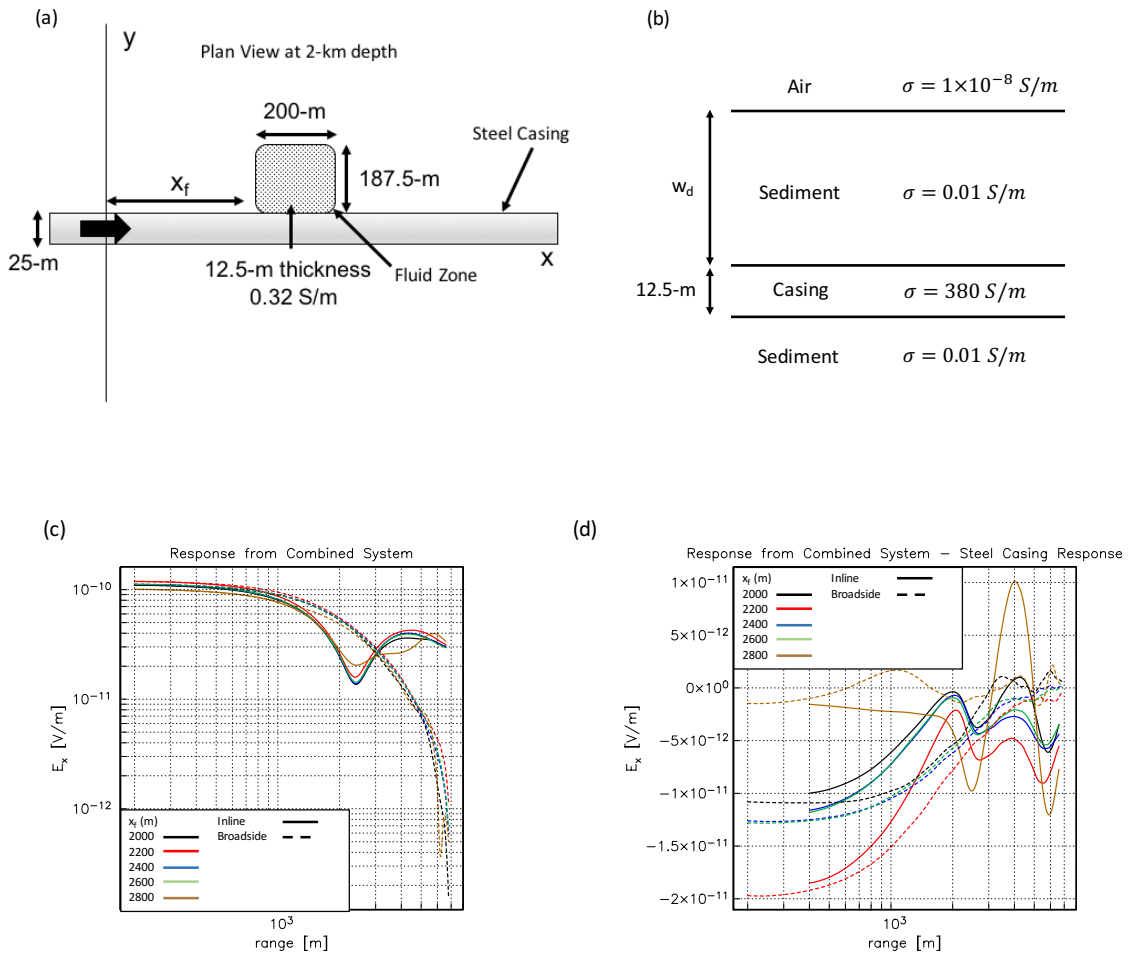
Figure 30 (a) shows a plan view at 2-km depth, which incorporates the lateral wellbore described in figure 26, with the fluid filled fracture zones from Figure 27. The geoelectrical model for this scenario is shown in (b). (c) demonstrates the inline (solid) and broadside (dashed) secondary electric field responses associated with the model. (d) shows the inline electric field responses once the wellbore signature has been subtracted from the secondary field responses. In this case, the broadside responses were not plotted due to their complex nature. (d) demonstrates that the fluid signature cannot be retrieved through this method due to the mutual inductance between wellbore and fracture zone

63
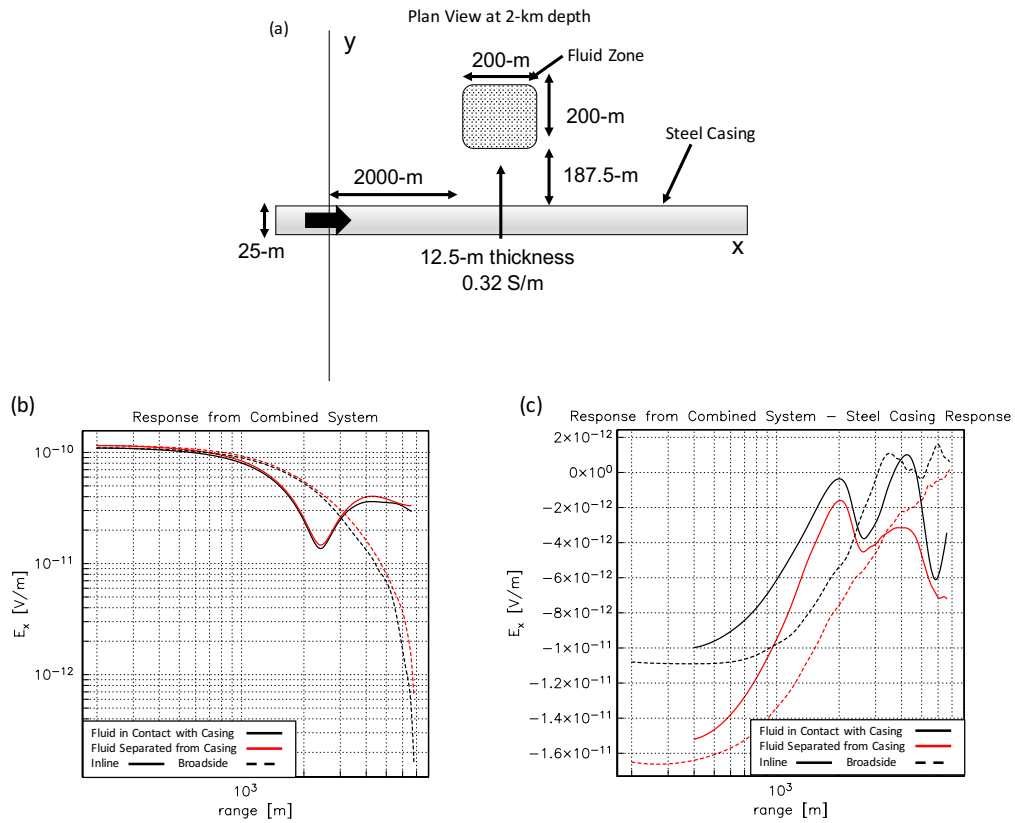
Figure 31 (a) shows a plan view at 2-km depth, for a case where the fluid is now separated from the steel casing by 200m. The geoelctrical model for this scenario is the same as figure 30b (c) demonstrates the inline (solid) and broadside (dashed) secondary electric field responses associated with this model (red) and that described in figure 30 for a fluid-transmitter offset of 2000m. (d) shows the inline electric field responses once the casing signature has been subtracted from the secondary field responses for both cases. demonstrating that the fluid signature pattern is complicated by inductive effects due to the presence of a reduced, but non zero response

Discussion

Responses show that the presence and location of a lateral steel wellbore or a fluid zone can be determined in an idealized modelling scenario. The low amplitudes generated by fluid zones may be detectable only in low-noise environments provided there is a strong conductivity contrast between the fluid zones and the surrounding sediment.

The ability to detect fluid leakage depends upon factors such as the dipole moment of the source. If sufficiently powerful, the source could overcome the ambient noise. The latter varies temporally and spatially in a complex and unpredictable manner. The inline secondary electric-field response is more sensitive than the broadside response to the lateral casing or fluid zone. The role of magnetic susceptibility of the wellbore has been debated but it is not considered here; see Heagy et al., 2015, Puzyrev, et al. 2017, Kohnke et al, 2017. A vertical wellbore, extending to the surface is likewise not considered although it could generate a large signature (e.g. Patzer et al., 2017). Future simulations should try to determine realistic detection levels in the presence of oilfield electromagnetic noise. The latter is difficult to model as it varies site-by-site and day-by-day basis. The noise comprises both a randomly-varying, incoherent component as well as a potentially strong, signal-generated component caused by induction of eddy currents in the oilfield infrastructure.

The modelled dimensions of the lateral casing are made significantly more realistic by local refinement. They remain however much greater than the actual dimensions. The local refinement algorithm can, in principle, reduce the modelled casing

65

to its actual size. However, such fine-scale discretization would require an excessive amount of computing power. The finite-element matrix condition number degrades in the presence of large conductivity contrasts.

I find that inline responses correlate to the well casing burial depth and the lateral position of the fluid. The inline responses exhibit more signal variability than the broadside solutions and hence provide more diagnostic information about the fluid or the casing.

A knowledge of the geoelectrical properties of the host sediments is important. There is a large difference in response between a model with more-conductive clay sediments compared to one with less-conductive terrestrial sediment. The presence of an electrically conductive fluid-filled fracture zone is considerably easier to detect in terrestrial sediments than in clays.

In the case where the casing and fluid zones are both included in the model, the secondary inline electric-field response is dominated by the steel casing. Once the casing signature is removed, the remaining fluid zone response has a higher-than-expected amplitude. This suggests that the lateral wellbore is acting as a secondary source. The resulting complicated response is likely due to effects of mutual inductance between the casing and fluid zone. Mutual inductance effects can generate strongly variable CSEM responses (e.g. Fernandes 2008) caused by eddy currents generated in one conductive body due to the magnetic flux caused by the eddy currents generated in another.

A further investigation of mutual inductance shows that the amplitude of the fluid zone remains high even when it is separated from the casing. However, some

studies have suggested strong galvanic coupling between such zones and casing

(Cuevas, 2018), Further study is needed to acquire a greater understanding of the

wellbore-fluid electromagnetic coupling.

In the cases shown here, the fluid in the fracture zones is assumed to have spread

geometrically without any geotechnical or fluid-dynamical constraints. Improved

modelling of the movement of the electrically conductive fluid should be performed to

generate geomechanically feasible flow patterns and hence produce more realistic

CSEM signatures of the fluid motion.

Further tests on the dependence of CSEM detection of fluids on the operating

frequency should be conducted. For 1-Hz tests using terrestrial sediments, the skin depth

is 5 km while for clay sediments it is 1.6 km. Tuning the operating frequency above or

below 1 Hz will find the optimum frequency to be used for a specified depth of

investigation.

CHAPTER VI

FIELD PATTERNS IN ELECTROMAGNETICS IN THE PRESENCE OF STEEL

CASING FOR MARINE AND TERRESTRIAL ENVIRONMENTS

The controlled source electromagnetic (CSEM) technique has potential for use in detecting fluid movement away from a pipeline or wellbore due to large electrical conductivity contrasts between the fluid, steel-casing and host sedimentary formation. With different applications of the technique currently under development (e.g. Hickey et al 2015; Hickey et al 2017; Tietze et al, 2015, Tietze et al 2017), modeling studies are required to gain understanding and permit improved interpretation of CSEM responses. Electric-field responses in terrestrial environments have been discussed in the literature (Streich 2016, chapter 5); however, most efforts have focused on the response at the surface, rather than field patterns at depth.

Here, I describe electric field patterns in simplified scenarios representing fluid that has flowed out of a lateral steel wellbore. The electric field patterns are based on unrealistically large-radius wellbores, whose conductivity is assigned according to the transverse conductance formula (see chapter 4). A modified version of the 3-D finite element algorithm of Badea *et al.* (2001) is used which solves Maxwell's equations formulated in terms of Coulomb-gauged potentials on a cylindrical mesh. The potentials are computed at all interior nodes of the mesh, allowing for a post-processing step that involves calculation of electric and magnetic fields everywhere within the subsurface.

Previous CSEM studies have examined field distributions for a shallow-water case involving a resistive layer (Chave et al, 2016), and terrestrial cases involving conductive and resistive layers (Everett and Chave 2019). The main finding from these studies is that horizontal energy within the resistive layer is observed to flow toward the source. The studies are based on layered Earth models however that do not include a lateral wellbore or fluid.

This work presents modeling of idealized terrestrial CSEM responses of models that include the lateral steel-casing and conductive fluid. Field patterns for shallow marine and terrestrial settings are compared. The terrestrial patterns provide information in the presence of the complicating factors of the fluid and wellbore.

Both broadside and inline CSEM field patterns are evaluated in the form of 2-D vertical cross-sections, or slices. The inline slice is the vertical plane directly below a line on Earth's surface that is parallel to the dipole moment of the transmitter and contains the transmitter. The broadside slice is the vertical plane below a line on Earth's surface that is perpendicular to the dipole moment of the transmitter and contains the transmitter. The transmitter is modelled as an x-directed point electric dipole of moment of 1 A-m operating at frequency 1 Hz. A finite-length grounded-wire dipole source is not considered. The finite-length source allows a larger transmitter moment, which may improve the signal to noise ratio of the measured subsurface response.

Theory

Following the finite-element computation of the Coulomb-gauged potentials on the mesh-interior nodes (see chapter 2), the magnetic field **B** and auxiliary field **H** are calculated by numerical differentiation. This calculation is based on the definition of the magnetic vector potential *A*, equations (5.1 and 5.2, below). The electric field **E** is computed using equation (5.3).

$$B = \nabla \times A \tag{5.1}$$

$$H = \frac{B}{\mu_0} = \frac{1}{\mu_0}(\nabla \times A) \tag{5.2}$$

$$E = i\omega(A + \nabla \psi) \tag{5.3}$$

Modeling Results for Diminishing Water Depths

I first consider the patterns associated with conventional layered earth models. I use the geoelectrical models shown in Figure 32 to represent, respectively, a buried conductive or resistive layer. Furthermore I consider models characterized by water depths ranging from a marine case with water depth up to 2 km to a terrestrial setting, which is the limiting case of zero water depth.

I calculate various electromagnetic field components and visualize the field patterns in two dimensions in the inline and broadside planes. These planes are used since they provide complementary images of the associated field patterns. Figures 33 and 34 show the layered-earth field patterns associated at water depth 1 km for the

conductive layer case. The components E_x, E_y, E_z in the inline and broadside vertical

planes are shown in the respective figures. Evidently, the E_x component is dominated by

the source. The effect of the source is greatly diminished on the E_y component (note the

change in scale), which may make it easier to detect buried objects. The E_z component is

shown here for completeness but henceforth omitted as it is not commonly measured in

practice.
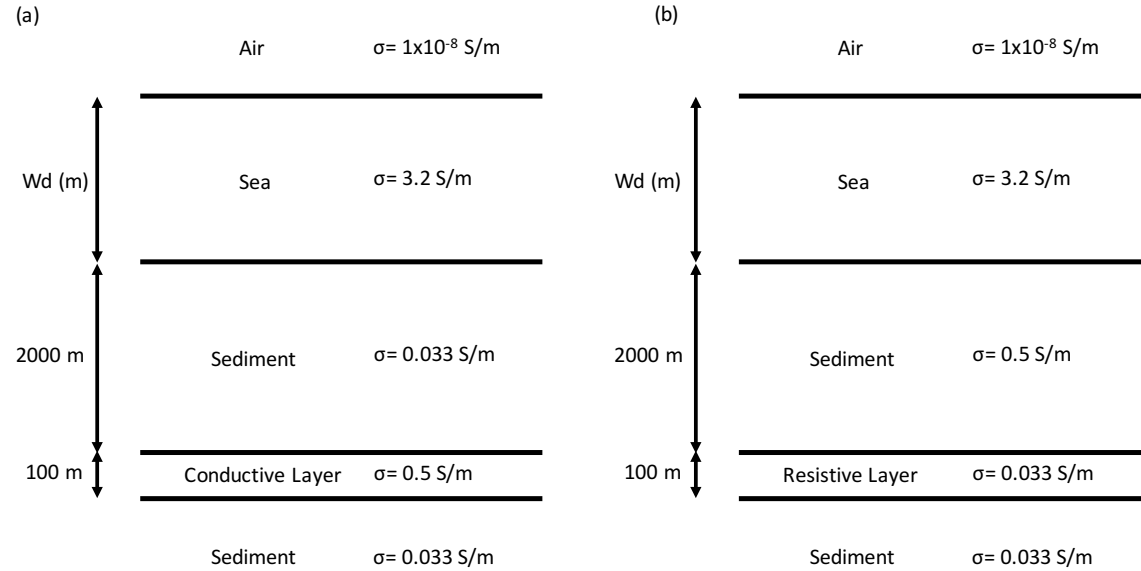
(a)

| | Air | σ= 1x10⁻⁸ S/m |

Wd (m) Sea σ= 3.2 S/m

2000 m Sediment σ= 0.033 S/m

100 m Conductive Layer σ= 0.5 S/m

Sediment σ= 0.033 S/m

(b)

Air σ= 1x10⁻⁸ S/m

Wd (m) Sea σ= 3.2 S/m

2000 m Sediment σ= 0.5 S/m

100 m Resistive Layer σ= 0.033 S/m

Sediment σ= 0.033 S/m

Figure 32 Geoelctrical model for cases with varying water depths including a buried conductive layer (a) and resistive buried layer (b)
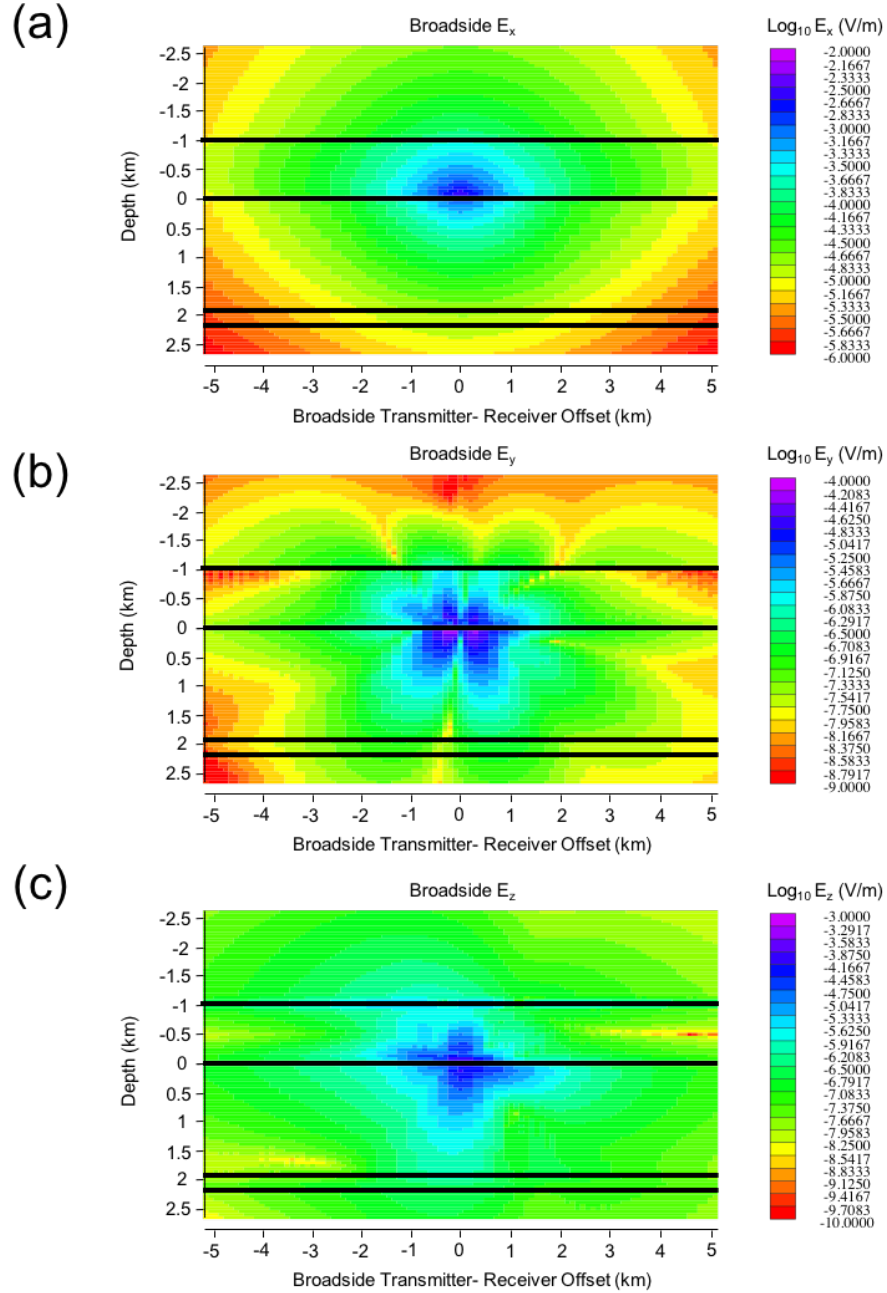
Figure 33 Broadside electric field patterns for each electric field component associated with the geoelectrical model shown in figure 32a for a water depth of 1-km. The annotated lines represent the boundary between the air and water layers, the boundary between the water layer and sediment and the two boundaries between the sediment and the conductive layer as seen from top to bottom
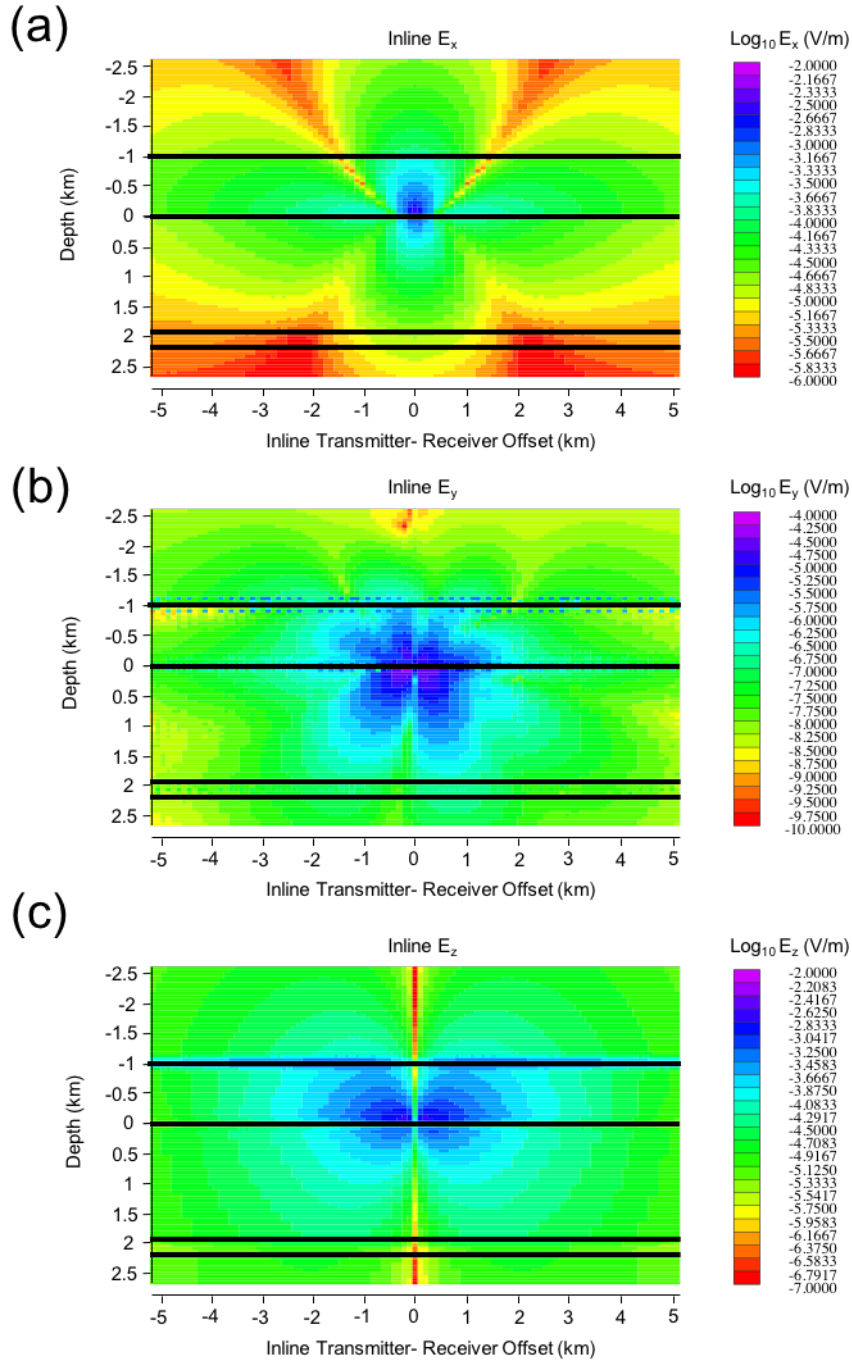
Figure 34 Inline electric field patterns for each electric field component associated with the geoelectrical model shown in figure 32a for a water depth of 1-km. The annotated lines represent the boundary between the air and water layers, the boundary between the water layer and sediment and the two boundaries between the sediment and the conductive layer as seen from top to bottom

Figure 35 shows E_x field patterns in the broadside plane for different water depths, while Figure 36 shows the same patterns in the inline plane. Figure 37 and 38 show the same information for the E_y component. There are advantages to examining each electric field component and orientation of view when attempting to detect the effects of layering in the field patterns. For instance, the water layer depth is more recognizable in the broadside field patterns (Figures 35, 36) compared to the inline patterns (Figures 37, 38). The presence of the conductive layer at depth is not evident in either the E_x broadside or inline patterns but does appear more prominently as a distortion in both E_y patterns. The field patterns associated with the terrestrial case (zero water depth) are not visible here due to their low field amplitudes.
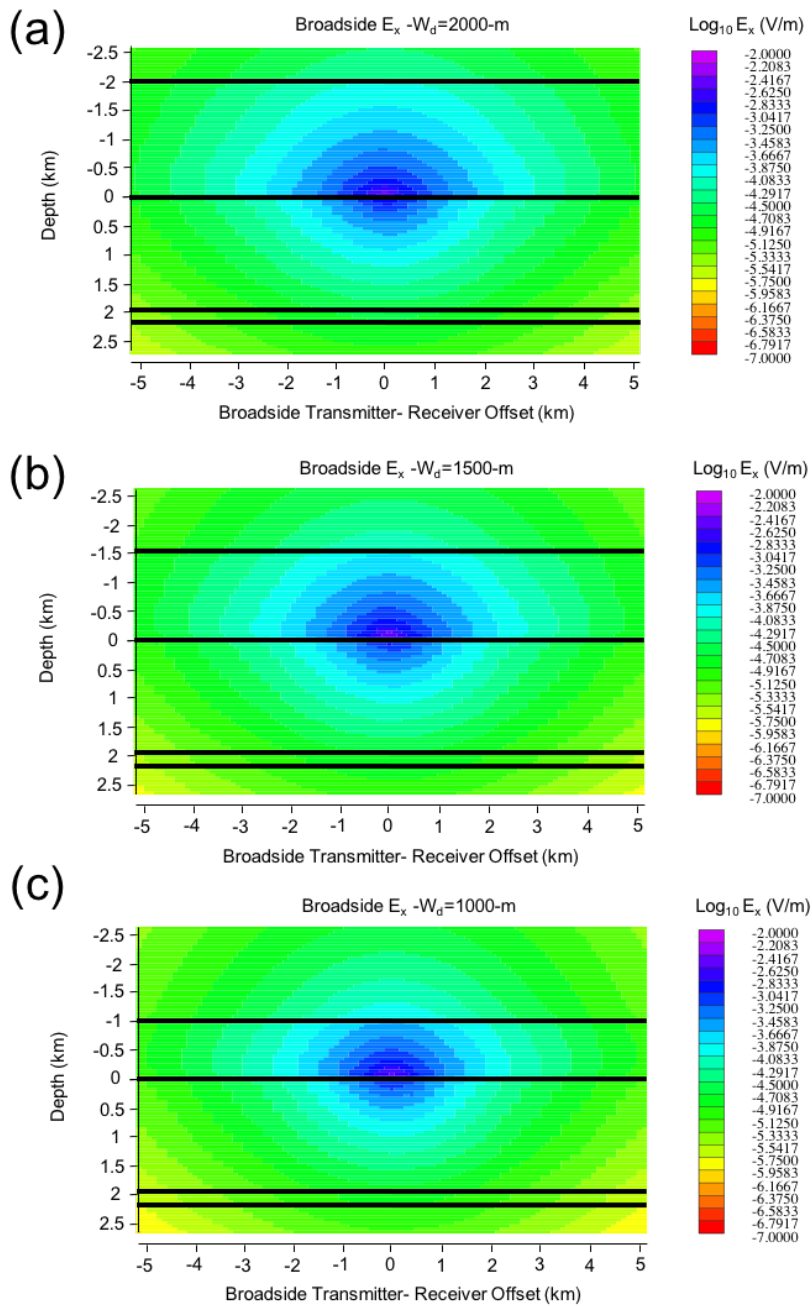
Figure 35 Broadside E$_x$ component for water depths of 2000 (a), 1500 (b), 1000 (c), 800 (d), 400 (e), 200 (f), 100 (g) and 0-m (h). The annotated lines represent the boundary between the air and water layers, the boundary between the water layer and sediment and the two boundaries between the sediment and the conductive layer as seen from top to bottom

Figure 35 Continued

(g) Broadside E_x -W_d=100-m

(h) Broadside E_x -W_d=0-m
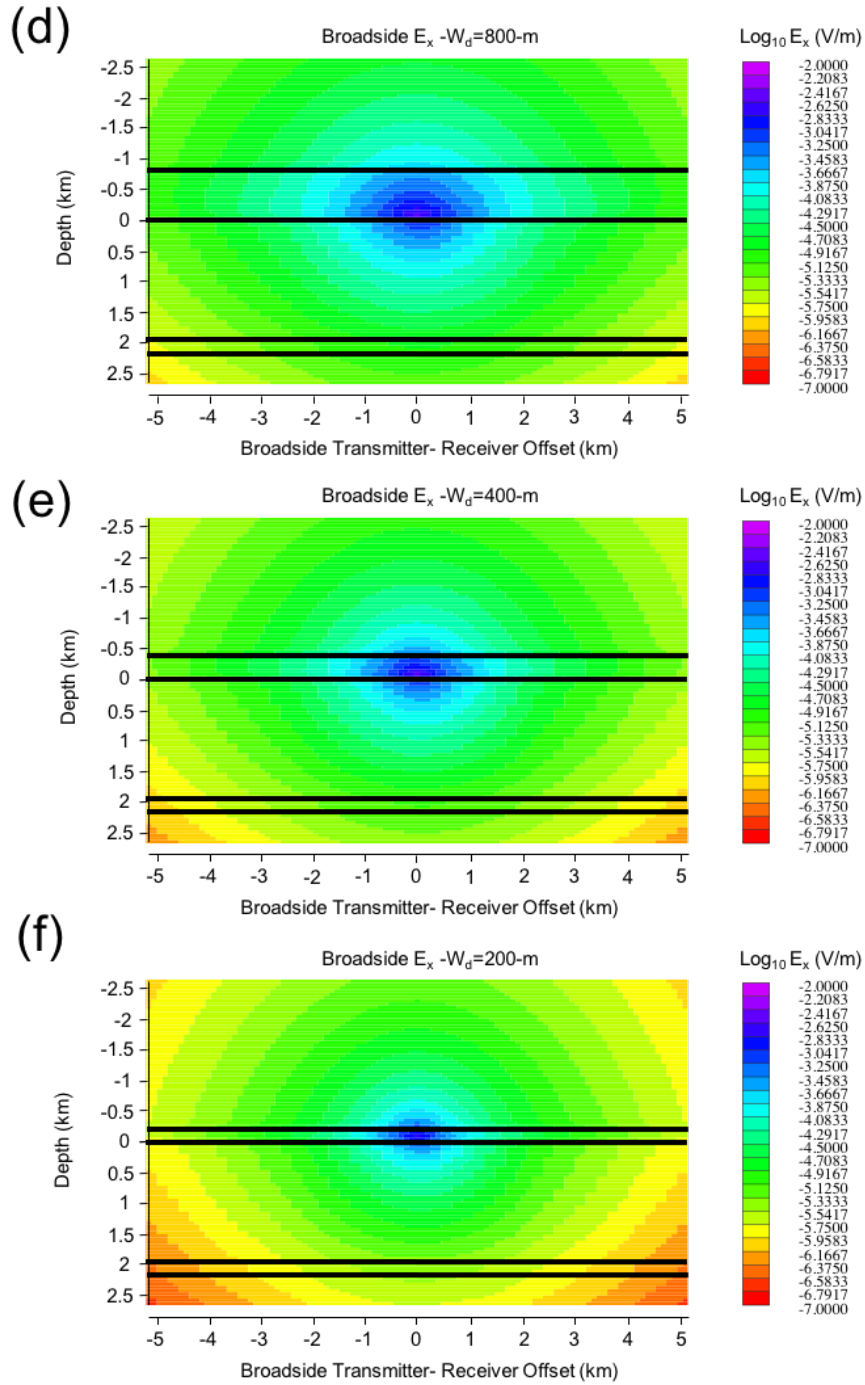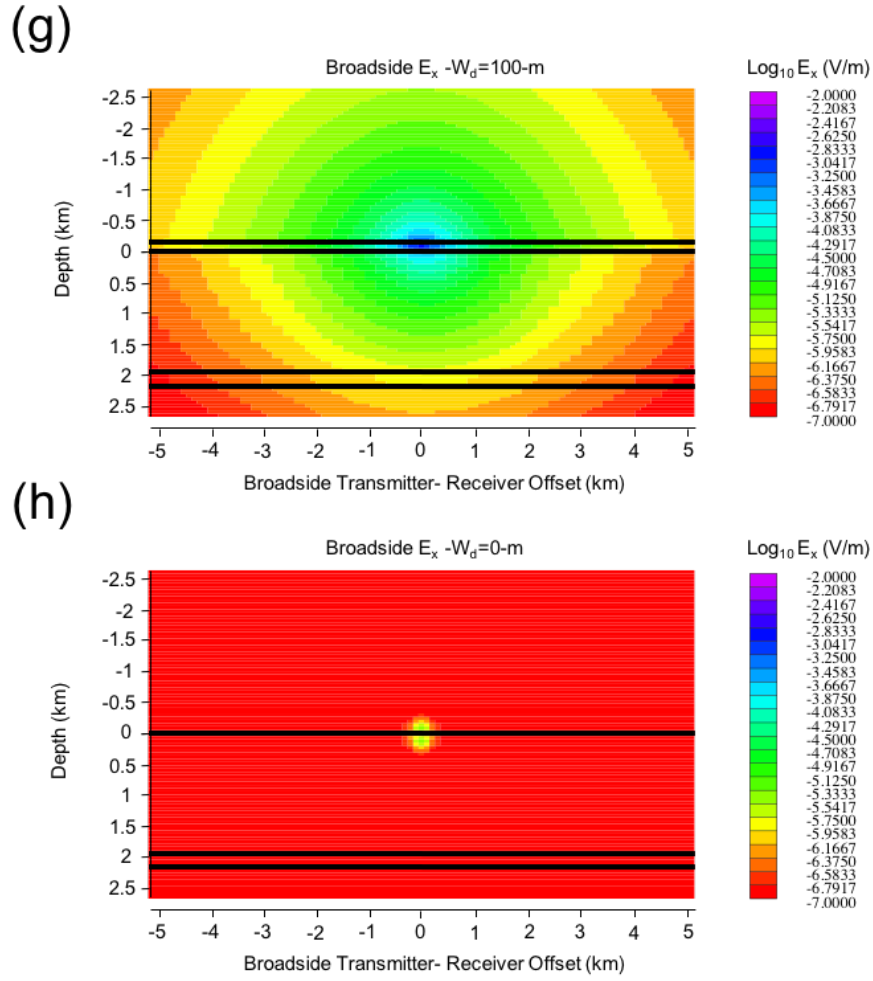
Figure 35 Continued
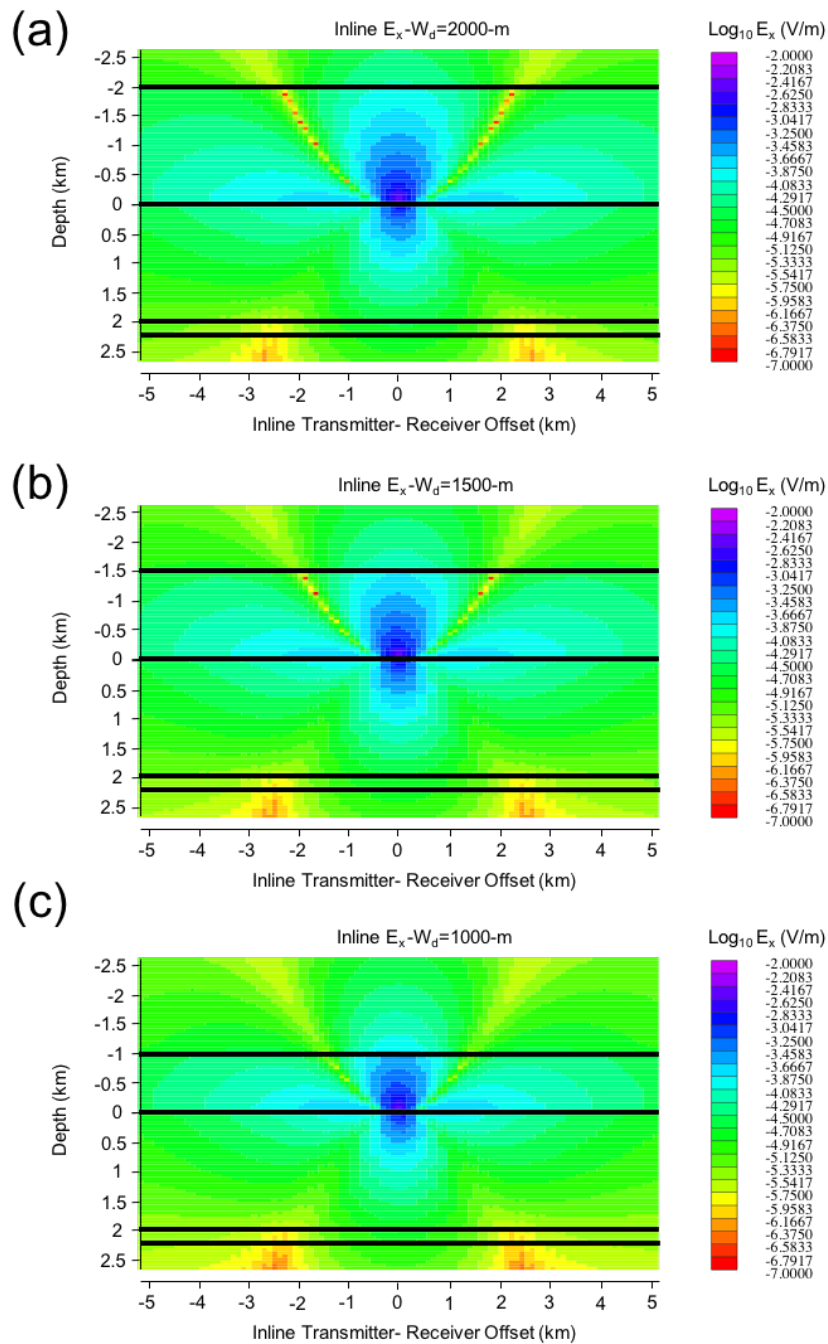
Figure 36 Inline E_x component for water depths of 2000 (a), 1500 (b), 1000 (c), 800 (d), 400 (e), 200 (f), 100 (g) and 0-m (h). The annotated lines represent the boundary between the air and water layers, the boundary between the water layer and sediment and the two boundaries between the sediment and the conductive layer as seen from top to bottom

78

Figure 36 Continued

(g)

Inline E_x-W_d=100-m

(h)

Inline E_x-W_d=0-m
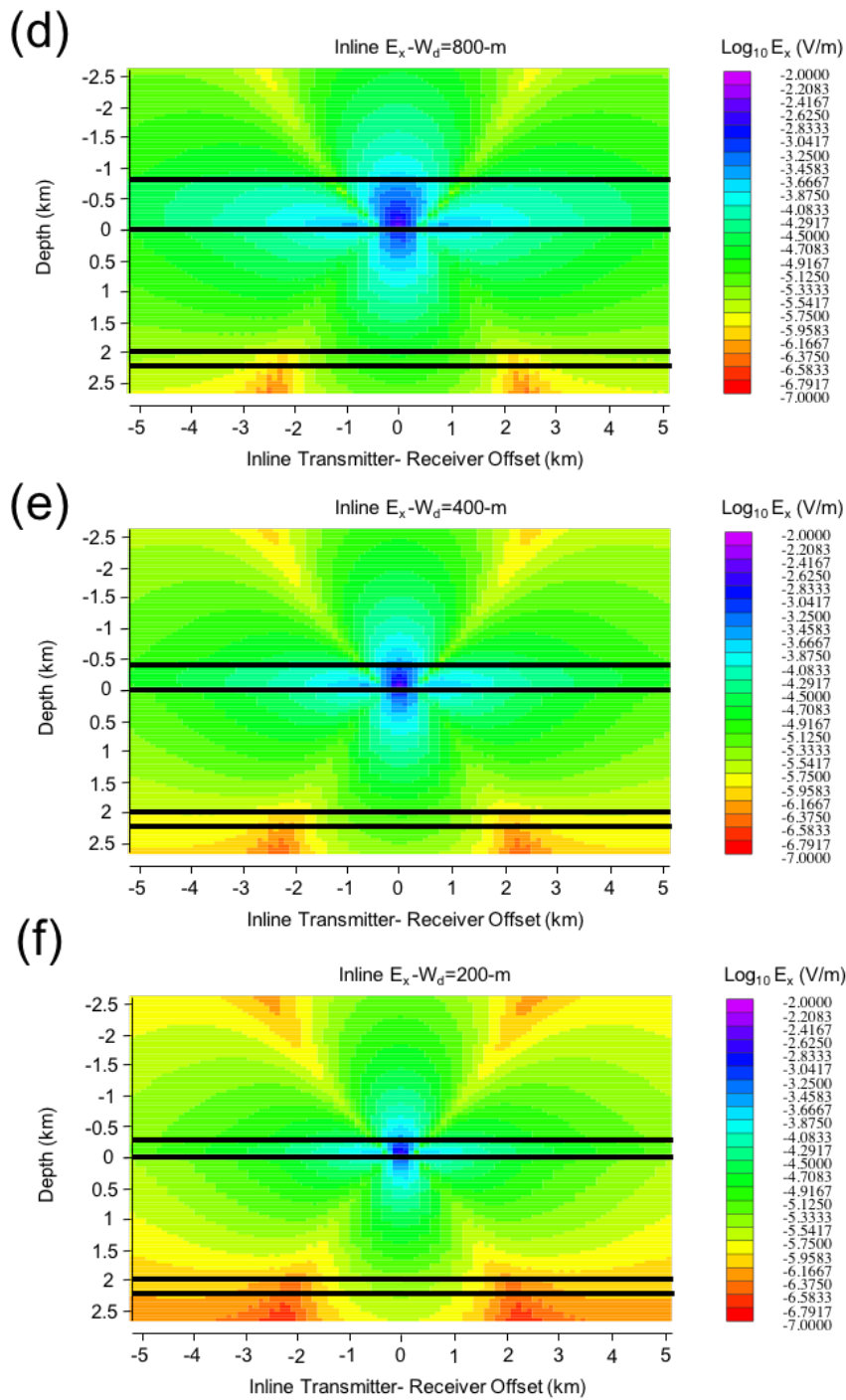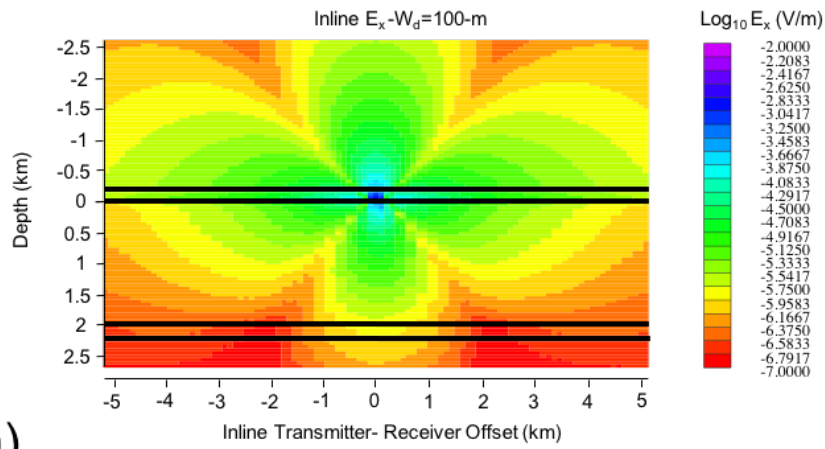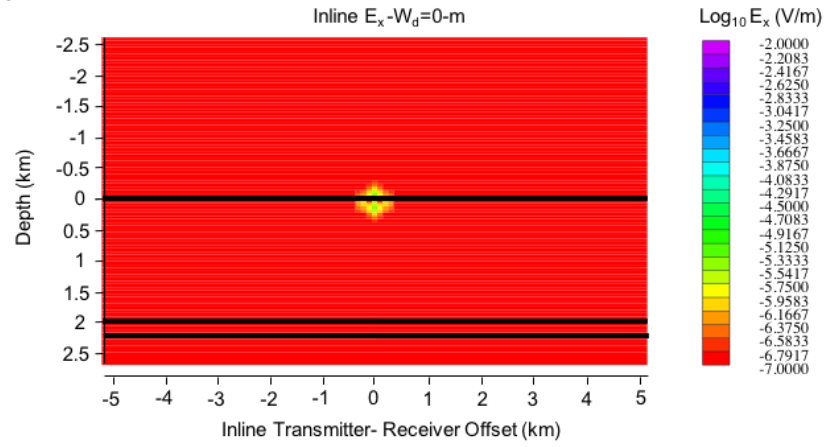
Figure 36 Continued
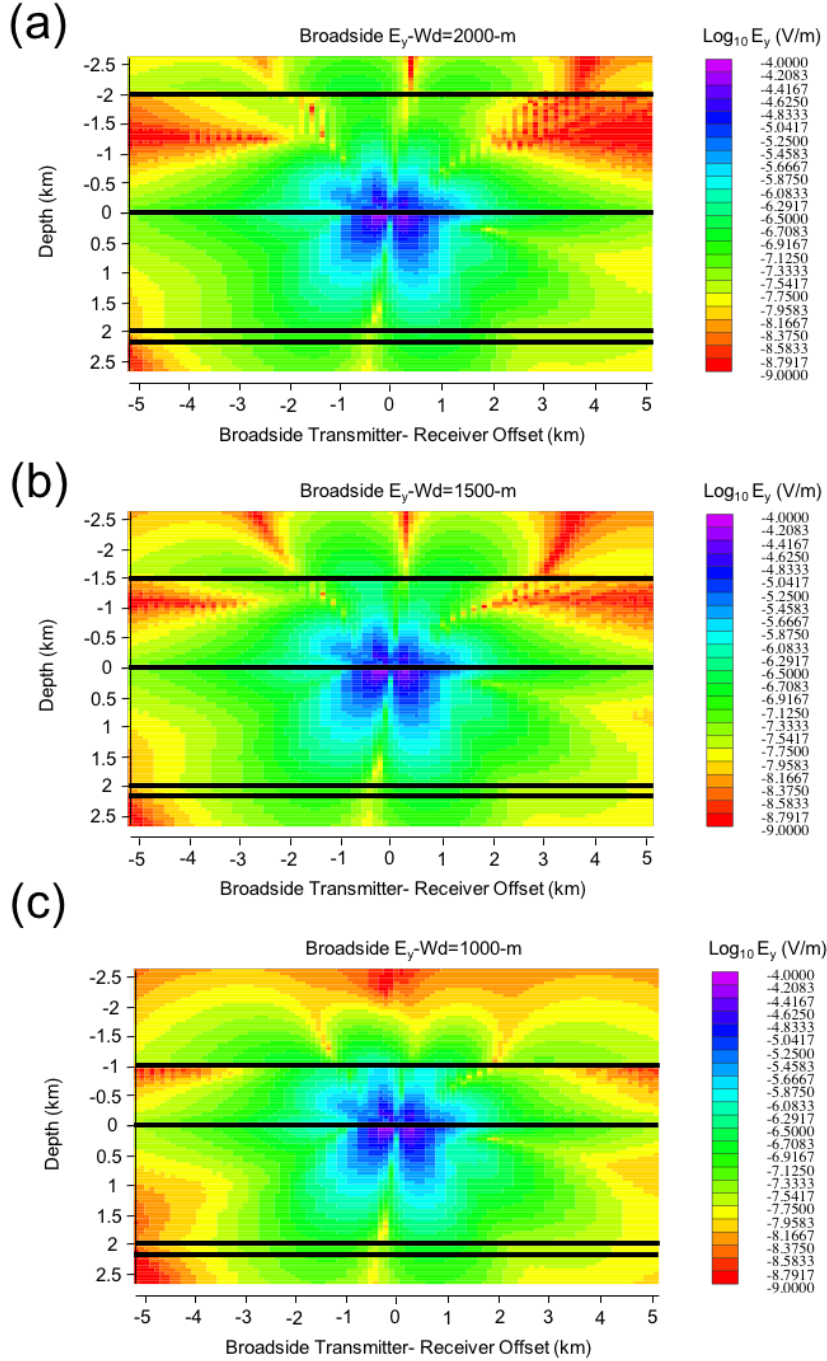
Figure 37 Broadside E$_y$ component for water depths of 2000 (a), 1500 (b), 1000 (c), 800 (d), 400 (e), 200 (f), 100 (g) and 0-m (h). The annotated lines represent the boundary between the air and water layers, the boundary between the water layer and sediment and the two boundaries between the sediment and the conductive layer as seen from top to bottom

(d) Broadside E$_y$-Wd=800-m

(e) Broadside E$_y$-Wd=400-m

(f) Broadside E$_y$-Wd=200-m

Figure 37 Continued

(g)

Broadside E$_y$-Wd=100-m

Log$_{10}$ E$_y$ (V/m)

(h)

Broadside E$_y$-Wd=0-m

Log$_{10}$ E$_y$ (V/m)

Figure 37 Continued

Figure 38 Inline E$_y$ component for water depths of 2000 (a), 1500 (b), 1000 (c), 800 (d), 400 (e), 200 (f), 100 (g) and 0-m (h). The annotated lines represent the boundary between the air and water layers, the boundary between the water layer and sediment and the top boundary between the sediment and the conductive layer as seen from top to bottom. In most cases the bottom boundary between the conductive layer and sediment is removed as not to obscure the field patterns associated with the conductive layer

Figure 38 Continued

85
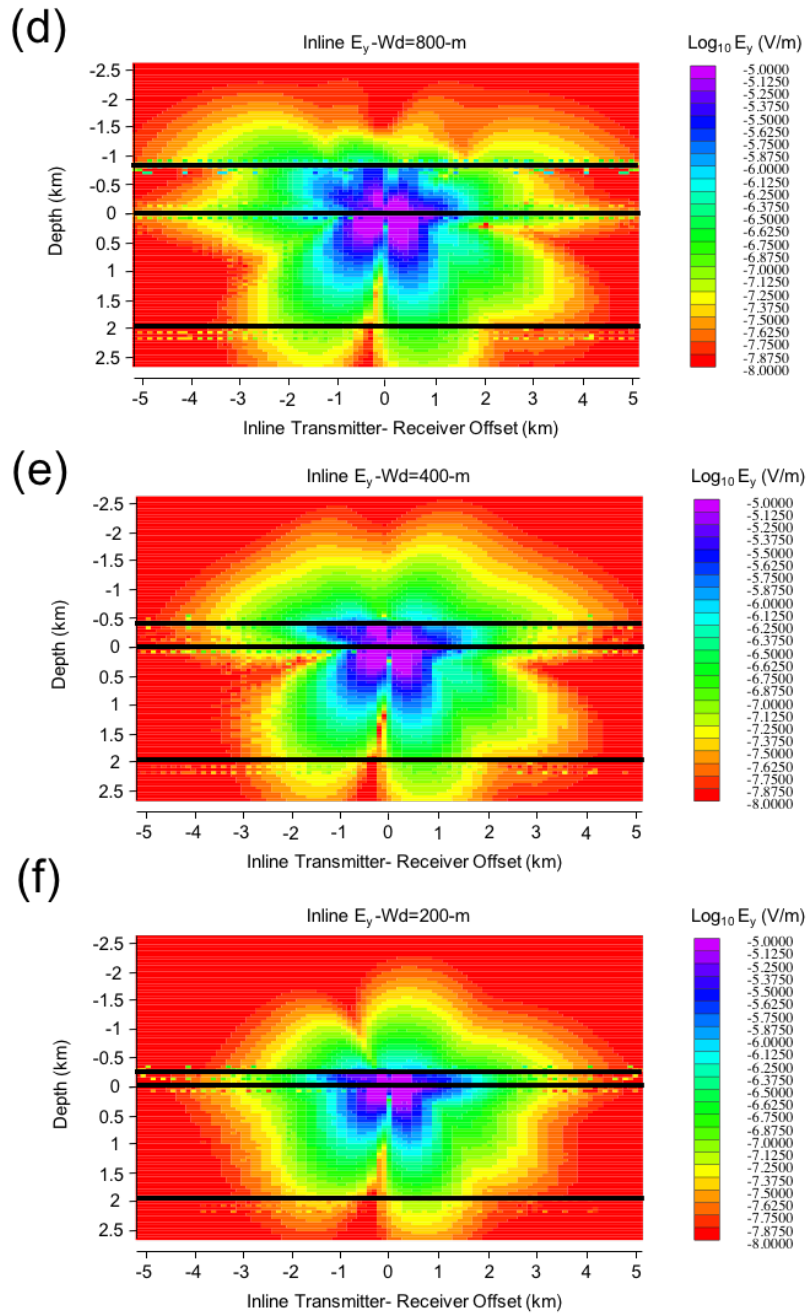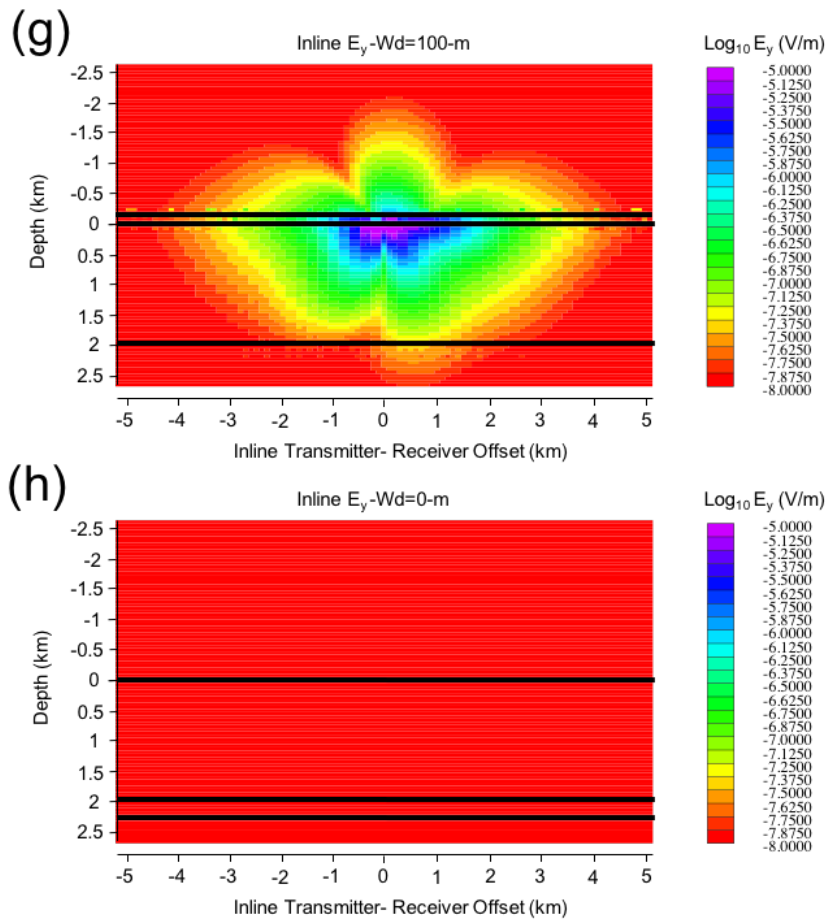
Figure 38 Continued

The terrestrial-source field patterns are shown more clearly in Figures 39 and 40. For the buried conductive layer it can be seen that the E_y inline field pattern is most distorted by the layer. No other components show such a clear distortion in the field pattern. The E_x component is aligned with the source, hence its field patterns are dominated by the source. The contribution from the source is vastly diminished for E_y, thereby better revealing the distortion caused by the buried conductive layer.

For the resistive layer case, the E_x and E_y field patterns (see Appendix A) are sensitive to water depth in both orientations. The buried resistive layer is more distinguishable in the inline patterns.

The remainder of the chapter is concerned with field patterns associated with the terrestrial source deployed in the presence of a lateral wellbore and/or fluid-filled fractures.
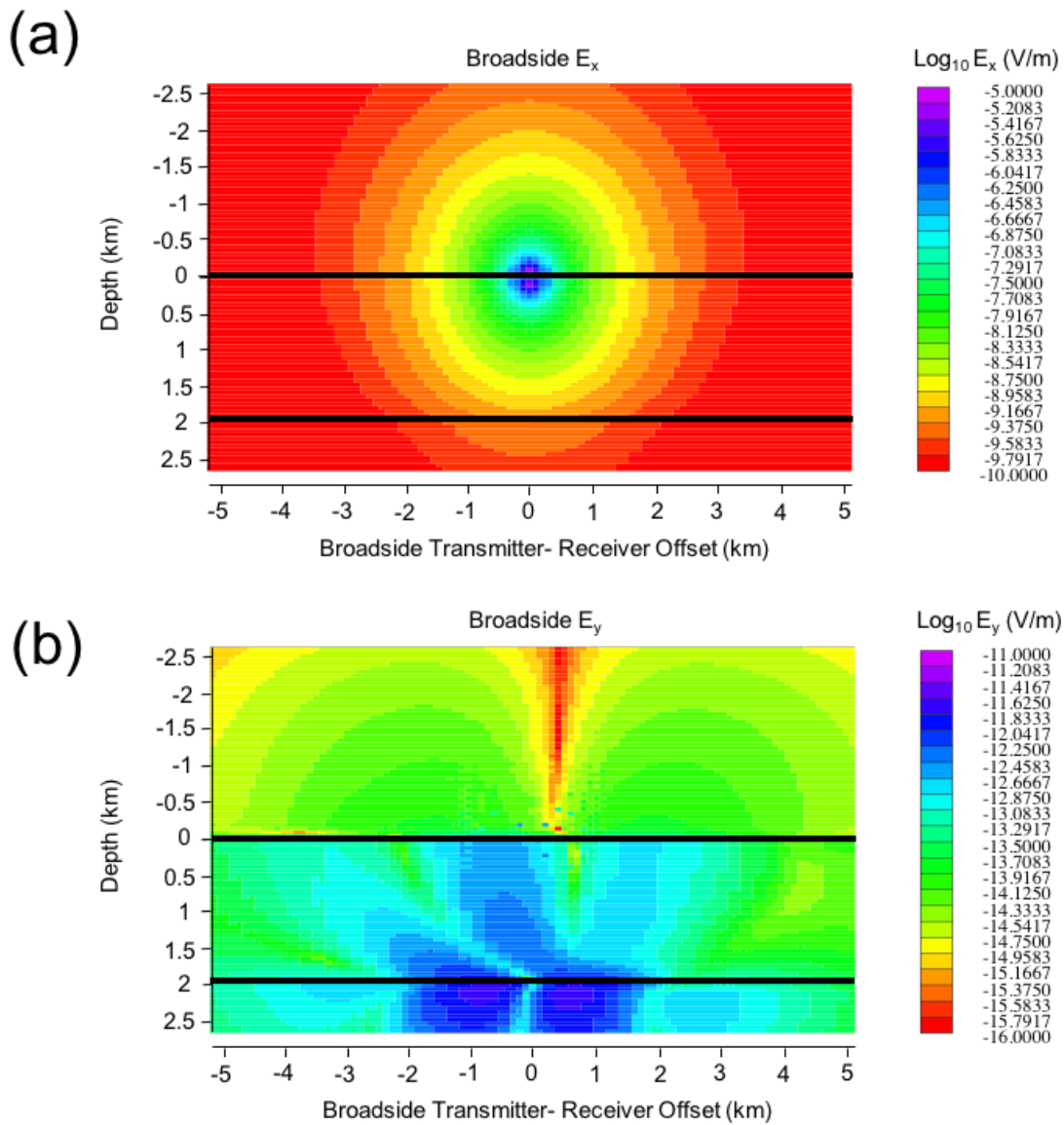
Figure 39 Broadside electric field patterns for each horizontal electric field component associated with the geoelectrical model shown in figure 32a for the terrestrial case. The annotated lines represent the boundary between the air sediment and the top boundary between the sediment and the conductive layer as seen from top to bottom. In this case the bottom boundary between the conductive layer and sediment has not been labelled to allow for an unobstructed view of the field pattern in this area
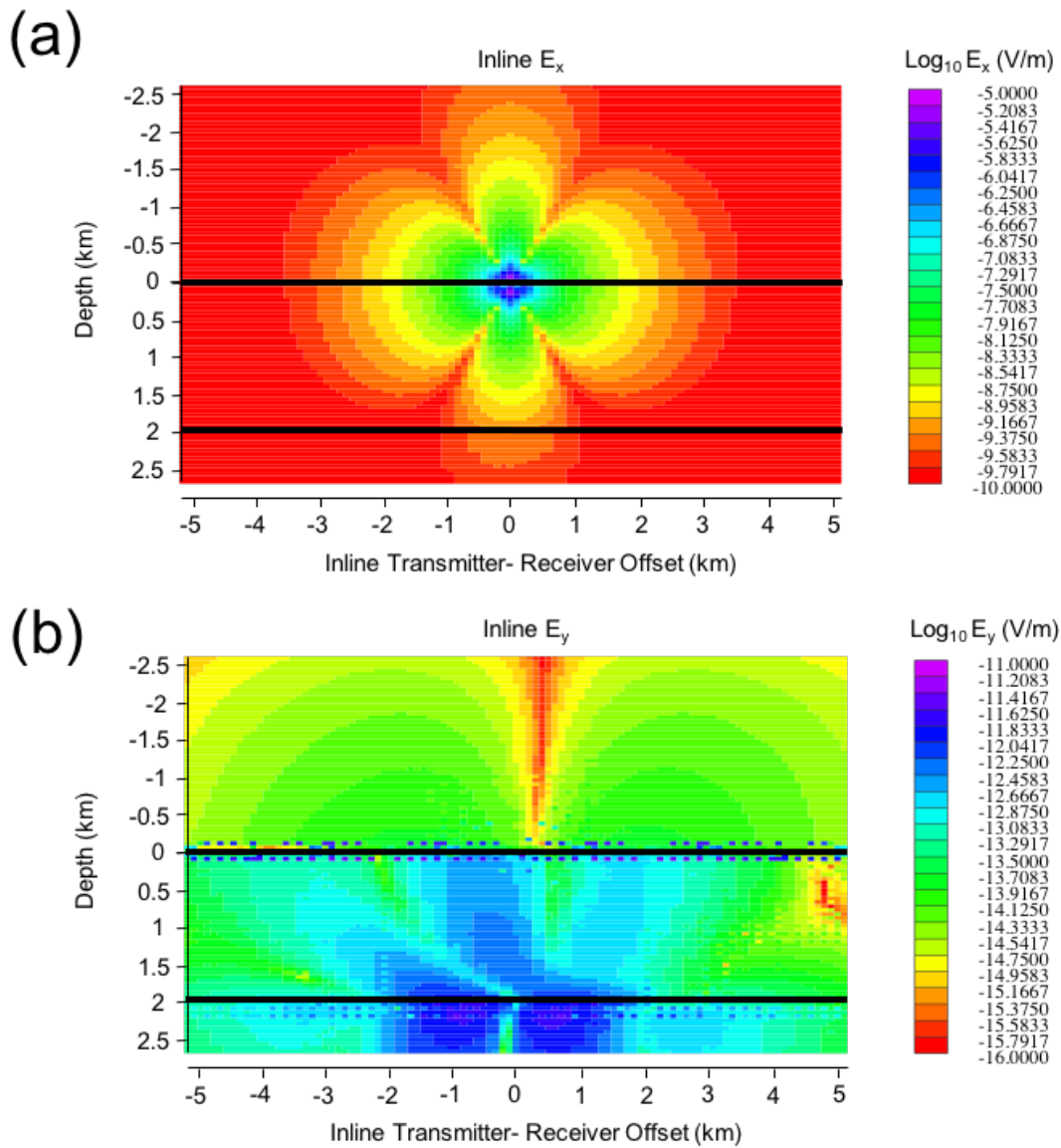
Figure 40 Inline electric field patterns for each horizontal electric field component associated with the geoelectrical model shown in figure 32a for the terrestrial case. The annotated lines represent the boundary between the air sediment and the top boundary between the sediment and the conductive layer as seen from top to bottom. In this case th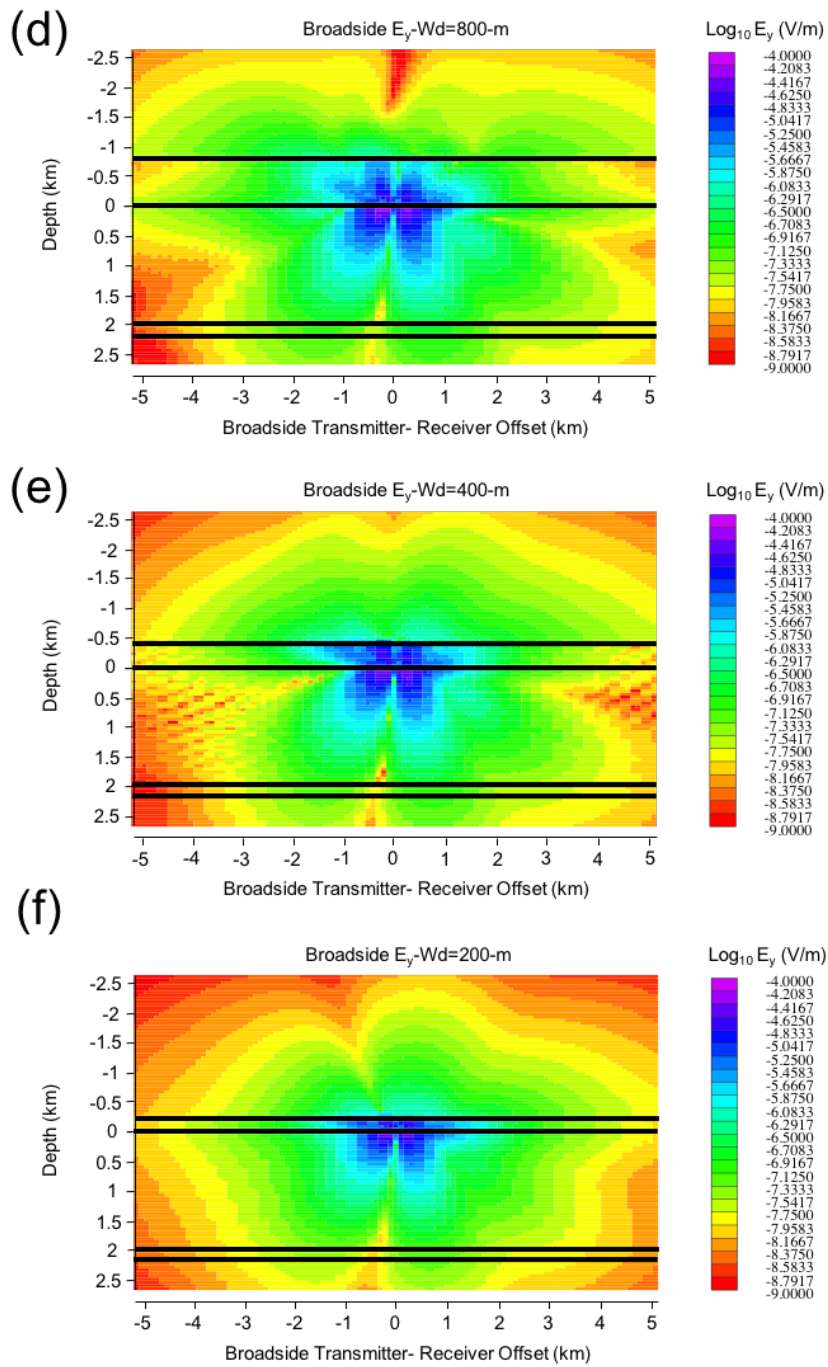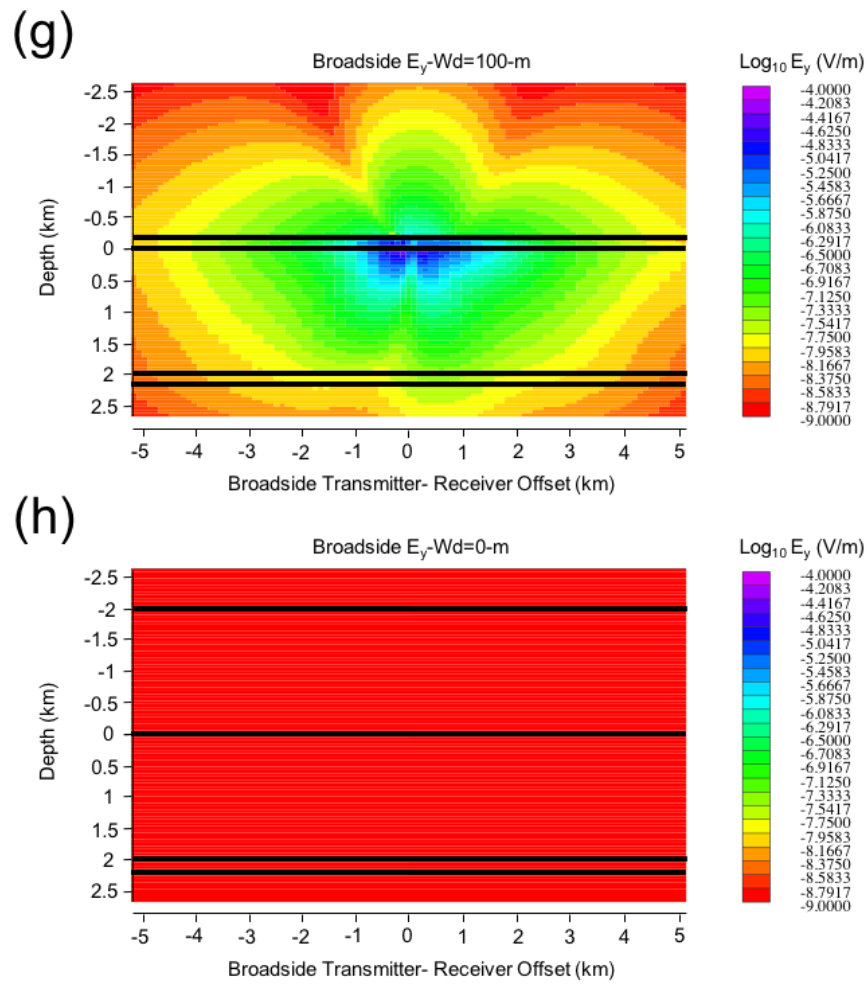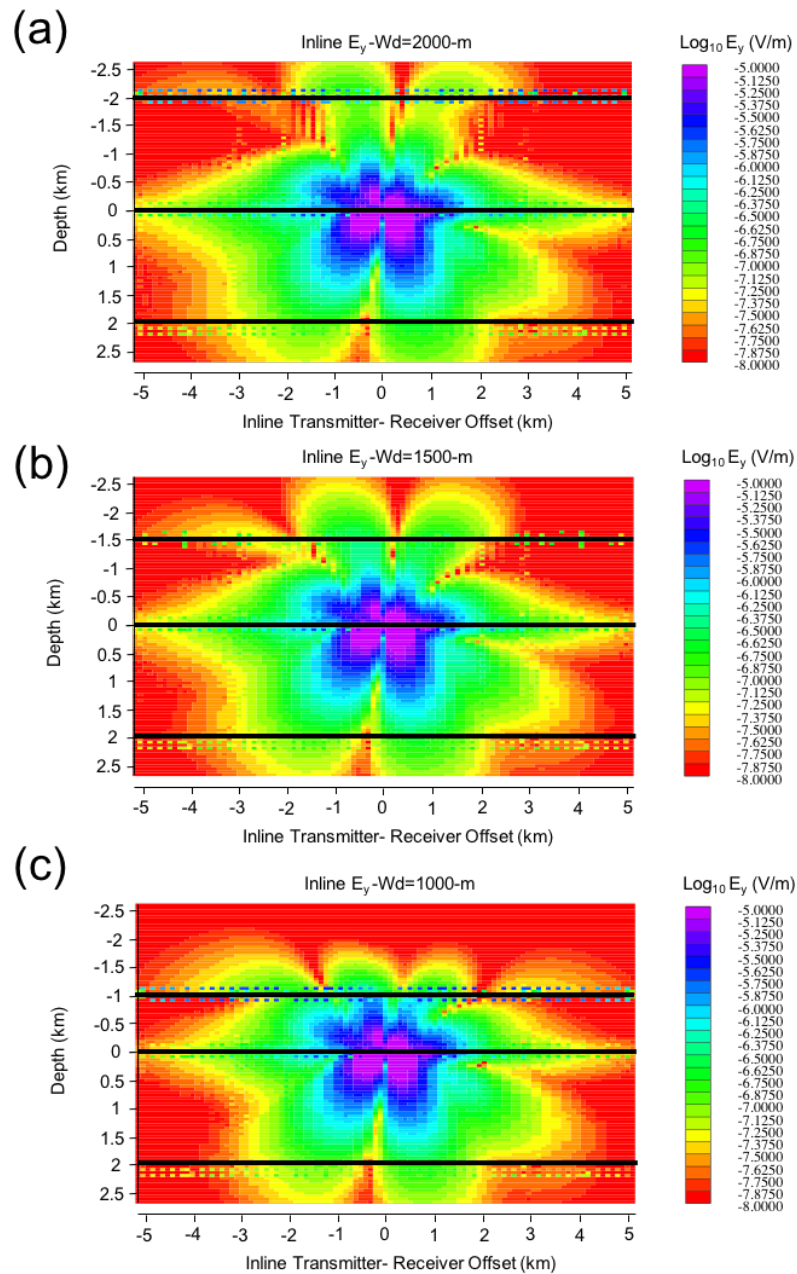e bottom boundary between the conductive layer and sediment has not been labelled to allow for an unobstructed view of the field pattern in this area.

Electric Field Patterns in the Presence of a Lateral Wellbore

The modeled lateral wellbore is a rectangular prism of infinite length with cross

section 25×25 m and conductivity 192 S/m, matching the transverse conductance of a

realistic wellbore with 2 cm wall thickness and 11 cm radius. The wellbore is buried 2

km in terrestrial sediments of conductivity 0.01 S/m. A plan view of the geoelectrical

model under consideration in this section is shown in Figure 41.
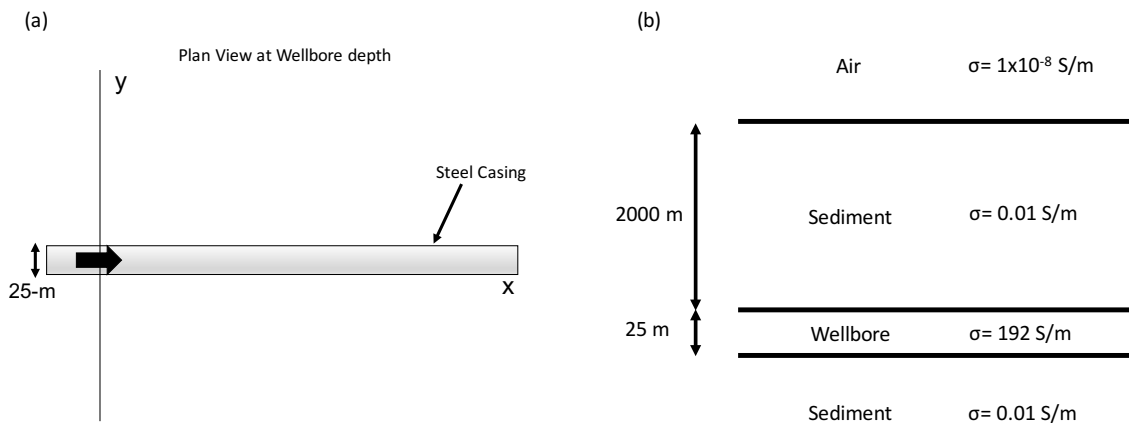
Figure 41 Plan view at 2-km depth (a) and geoelectrical model (b) for determining electric field patterns associated with the presence of a lateral wellbore

The electric field patterns in Figures 42 and 43 show the effect of the wellbore in

both inline and broadside planes. The wellbore effect is stronger in the E_y-component,

due to the absence of the dominating primary field from the transmitter in that direction,

and weaker in the E_x field patterns which are dominated by the primary field. The

wellbore can be seen in the inline plane due to its high conductivity. However the E_x

broadside pattern does not show a wellbore effect as clearly as the corresponding E_y

pattern. The wellbore effect on the E_y component is evident in the broadside (Figure 44) and inline (Figure 45) planes for three different burial depths 1, 2 and 3 km.
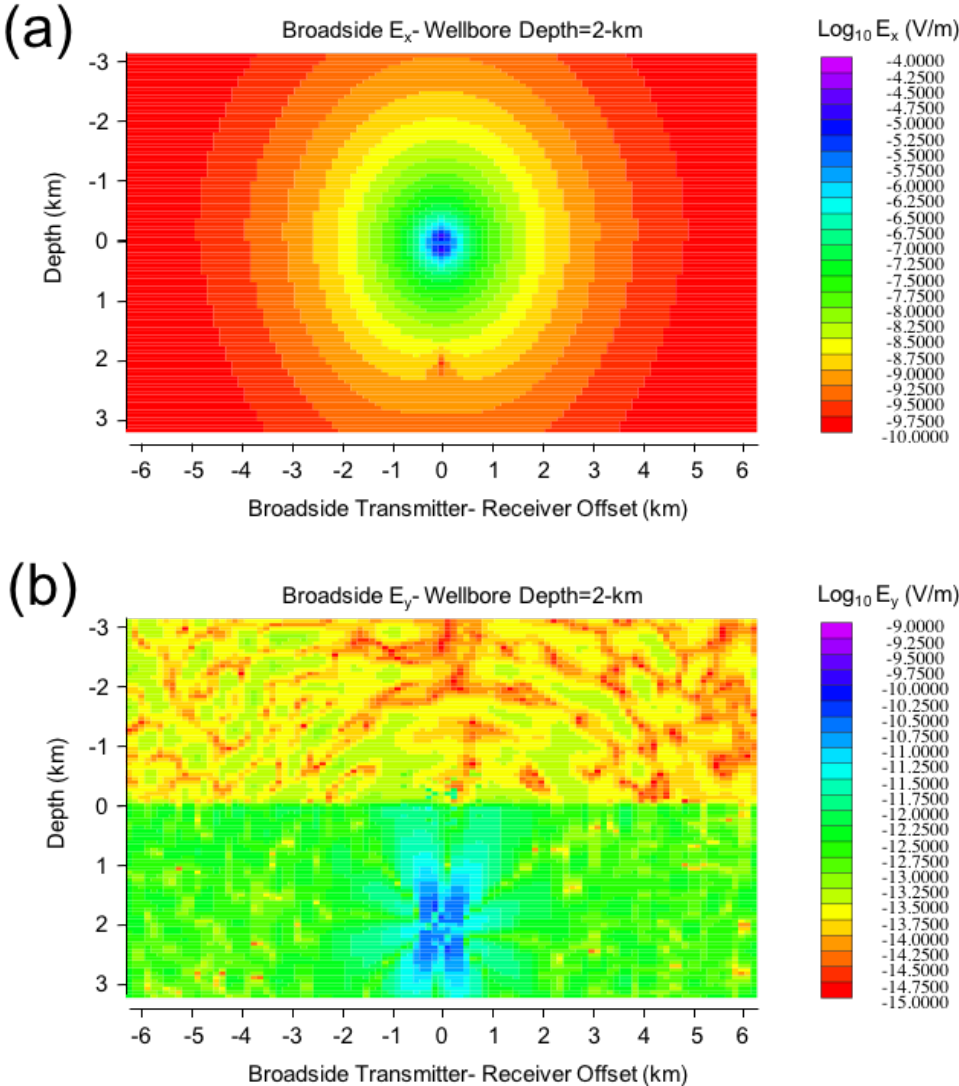
Figure 42 Broadside field patterns for E_x (a) and E_y (b)
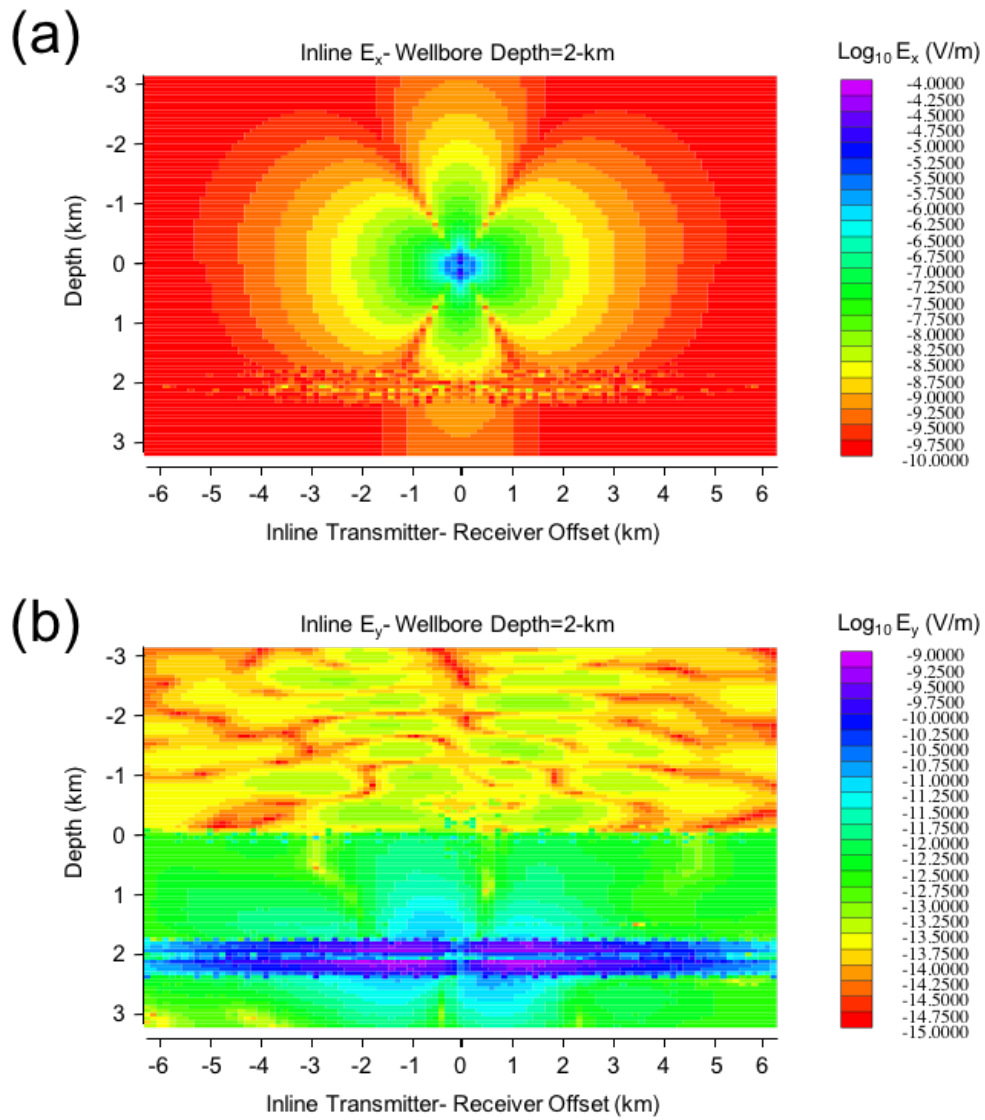
Figure 43 Inline field patterns for E_x (a) and E_y (b)
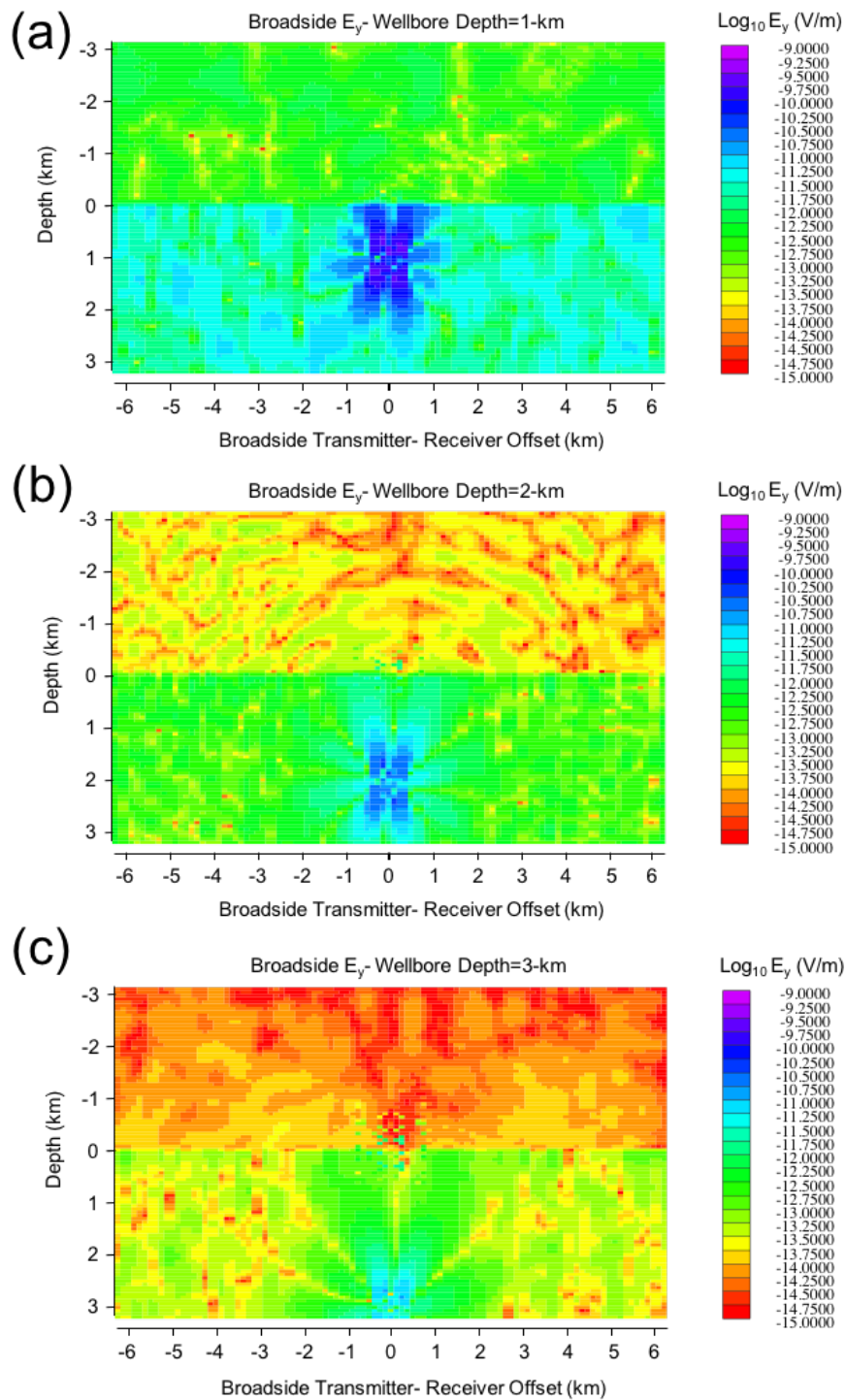
Figure 44 Y-Component electric field patterns for wellbore at 1-km (a), 2-km (b) and 3-km (c) depth for inline orientations

93
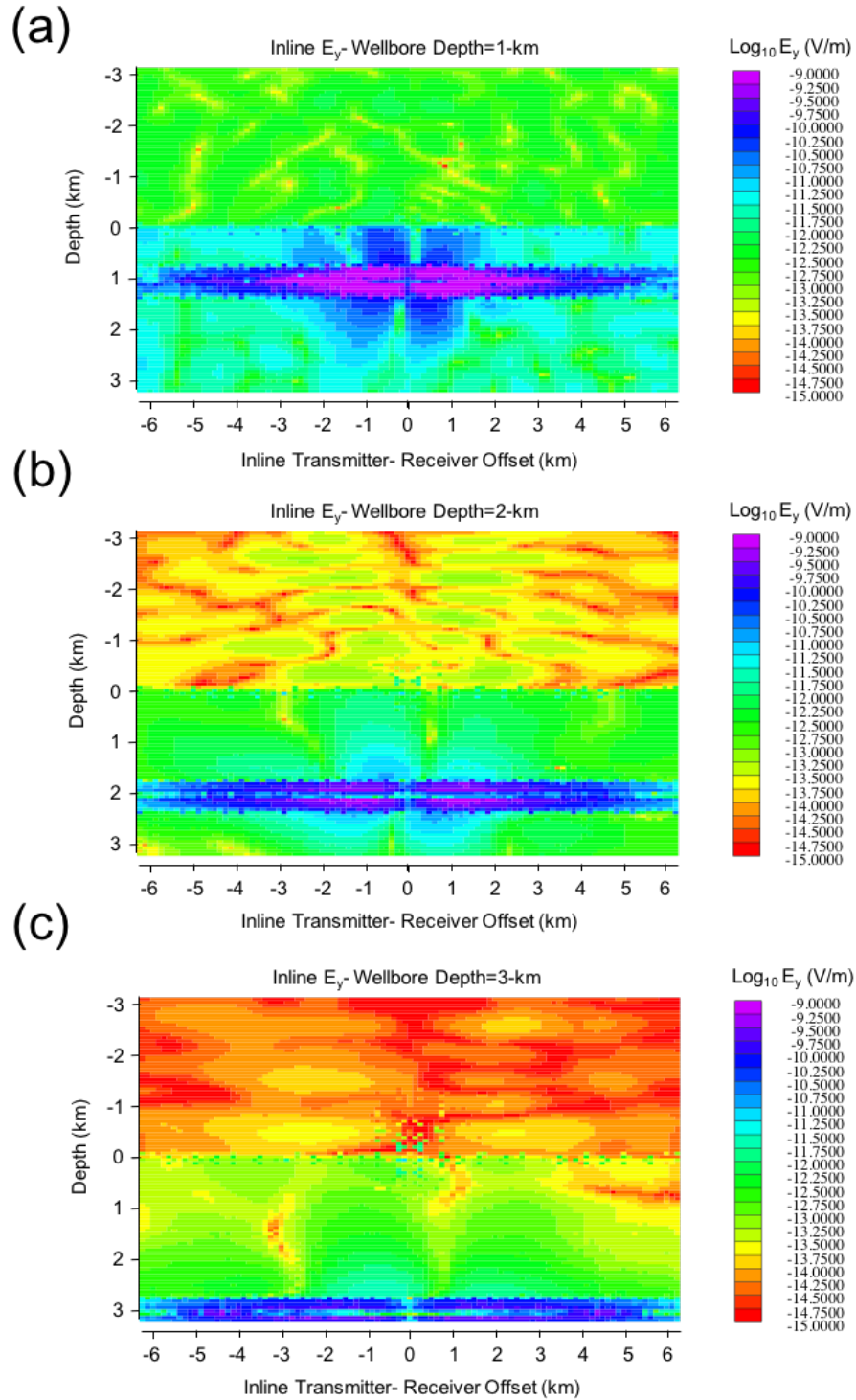
Figure 45 Y-Component electric field patterns for wellbore at 1-km (a), 2-km (b) and 3-km (c) depth for inline orientations

It is of interest to model the CSEM response of a finite-length lateral wellbore. In Figure 46, a geoelectrical model is indicated for which a wellbore "toe", or lateral termination, is present. The termination is located at various TX offsets of 1-5 km. In each case the wellbore is buried at 2 km depth within terrestrial sediment.
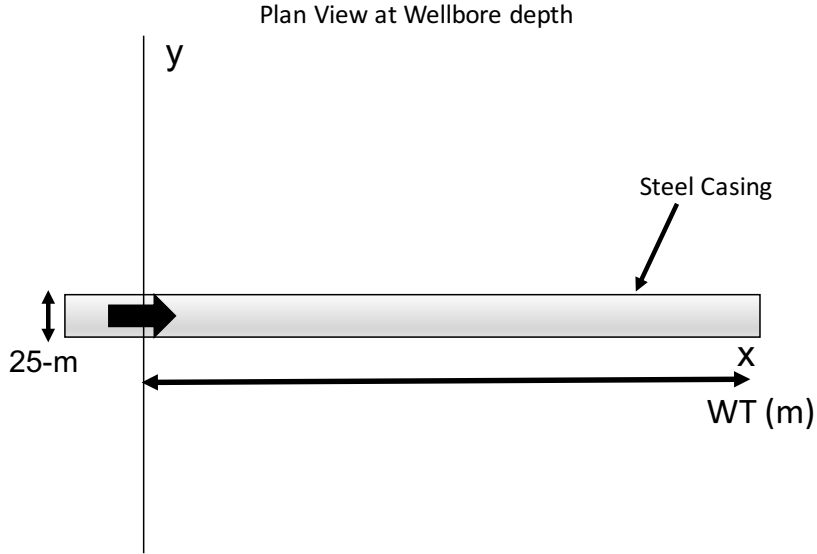
Figure 46 Plan view at 2-km depth for scenario where the wellbore is no longer infinite in the inline direction and now has a wellbore toe at a lateral distance WT from the transmitter
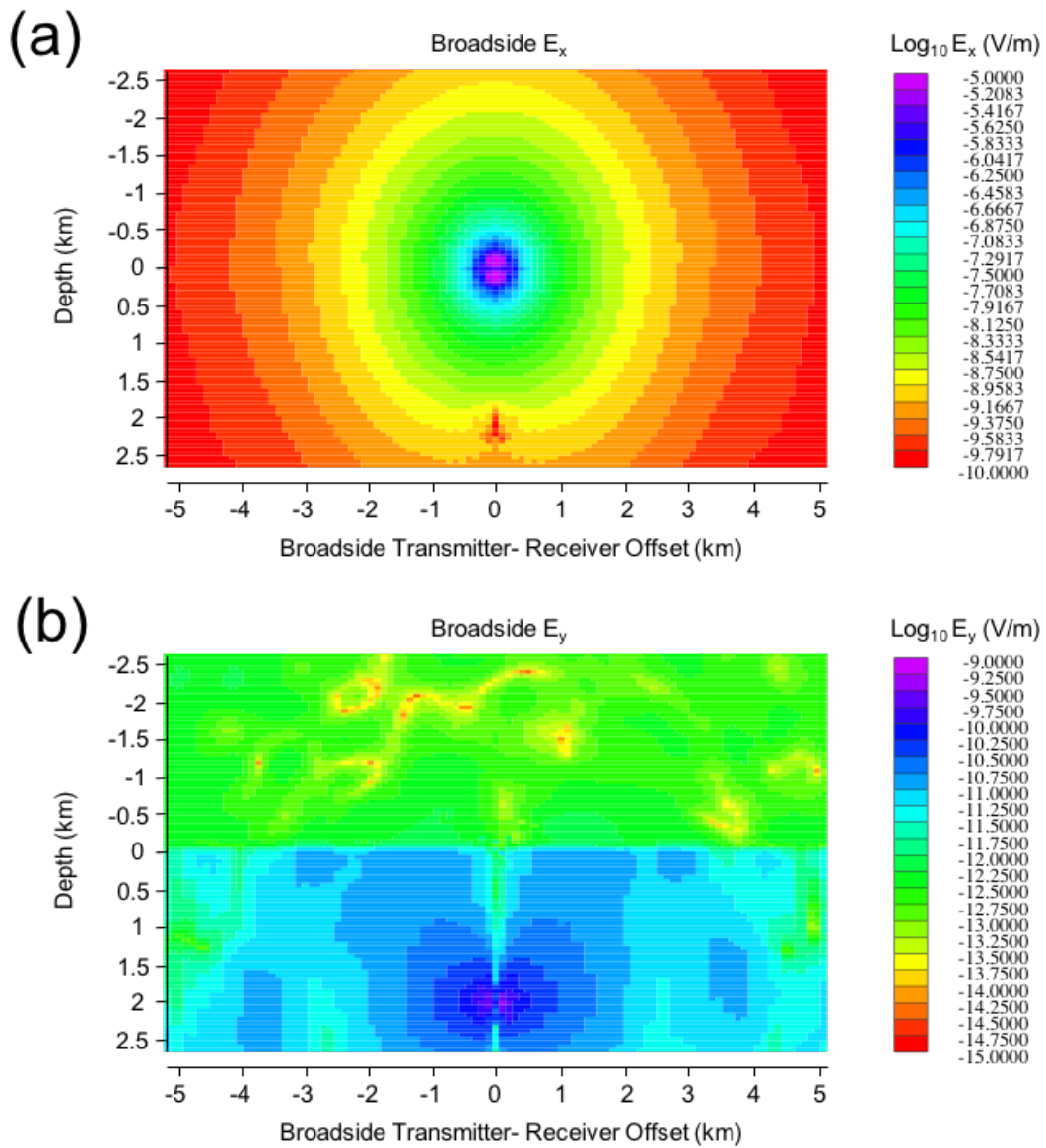
Figure 47 Broadside electric field patterns in the presence of a wellbore toe at a transmitter – toe lateral offset of 3-km. The field patterns are shown for the x (a) and y(b) components of the electric field for broadside orientation
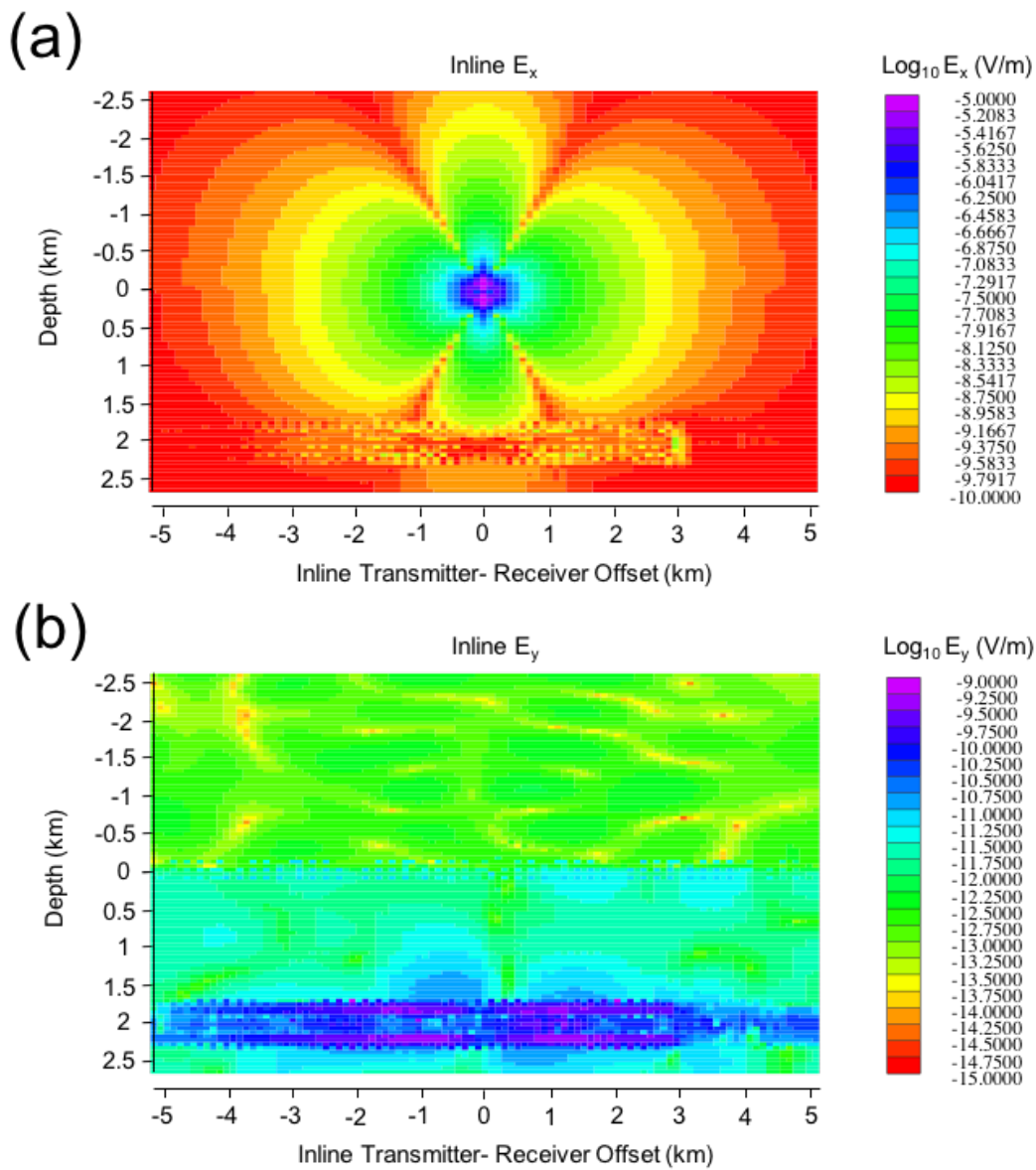
Figure 48 Inline Electric field patterns in the presence of a wellbore toe at a transmitter – toe lateral offset of 3-km. The field patterns are shown for the x (a) and y(b) components of the electric field for broadside orientation

As in the previous example, the wellbore effect is clearly revealed in the E_y field patterns (see Figures 47 and 48). The toe position, at 3 km lateral distance from the source, is most evident in the inline plane. The E_x inline field patterns show a less pronounced effect of the wellbore toe, due to competition from the high amplitudes generated by the primary field in that direction. The broadside field patterns do not exhibit a prominent effect caused by the lateral wellbore toe since these patterns reside in the $x = 0$ plane, which is 3 km distant from the toe location.

The field patterns in Figures 49 and 50 show the effect of the lateral offset between the transmitter and wellbore toe. The broadside field patterns show a decrease in amplitude with increasing offset. The inline field patterns better indicate the location of the toe. The relatively large broadside response at the toe location for small lateral transmitter-toe offsets may be explained by the wellbore termination acting as a "secondary transmitter". The operation of the electric dipole source at the surface induces an electric current along the length of the wellbore. This current is interrupted by the wellbore termination and flows, as if from a grounded source, into the surrounding geological formation.
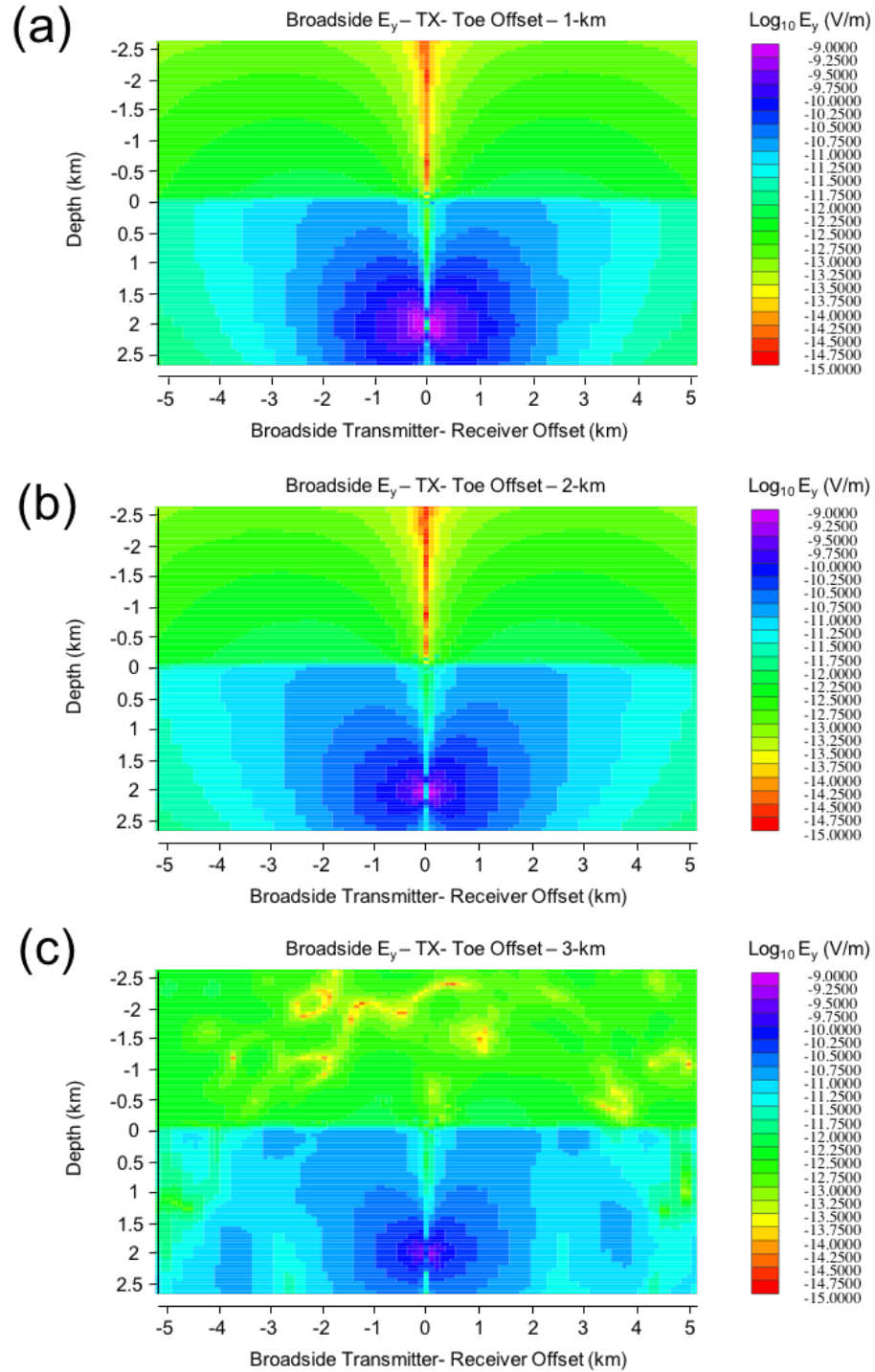
Figure 49 Y-competent electric field patterns for the broadside orientation for lateral wellbore toes located at transmitter toe offsets of 1 (a), 2 (b), 3 (c), 4 (d) and 5-km (e)
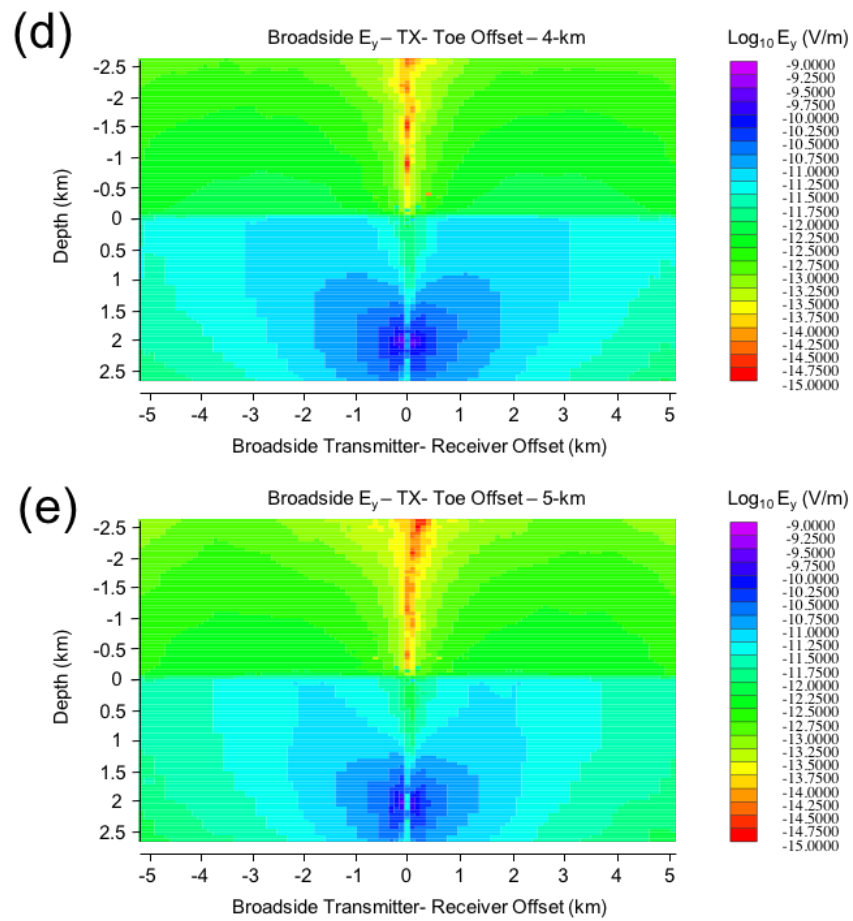
Figure 49 Continued
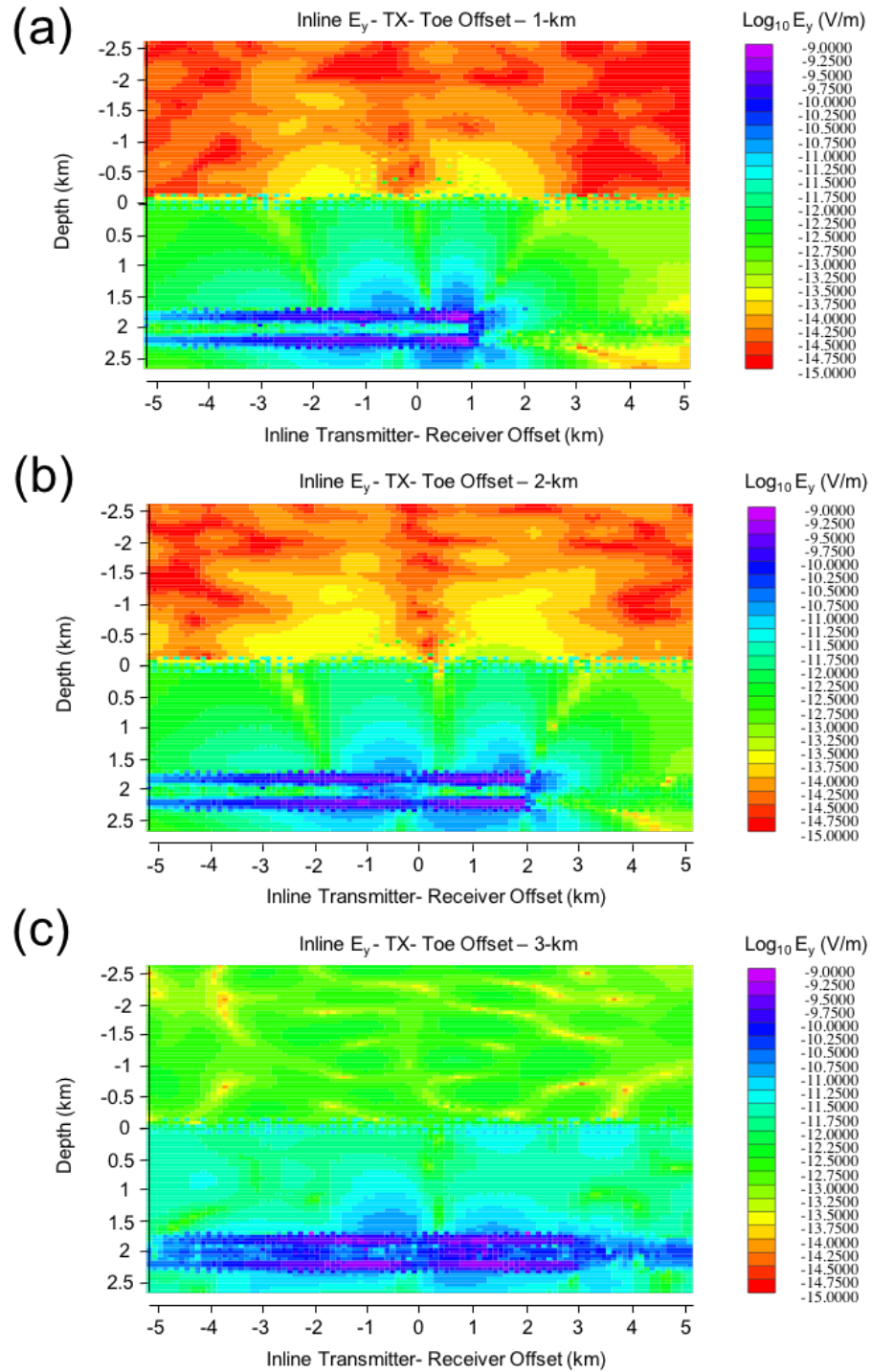
Figure 50 Y-competent electric field patterns for the inline orientation for lateral wellbore toes located at transmitter toe offsets of 1 (a), 2 (b), 3 (c), 4 (d) and 5-km (e)

(d)

Inline E$_y$ - TX - Toe Offset – 4-km

Log$_{10}$ E$_y$ (V/m)

Inline Transmitter- Receiver Offset (km)

(e)

Inline E$_y$ - TX - Toe Offset – 5-km

Log$_{10}$ E$_y$ (V/m)

Inline Transmitter- Receiver Offset (km)
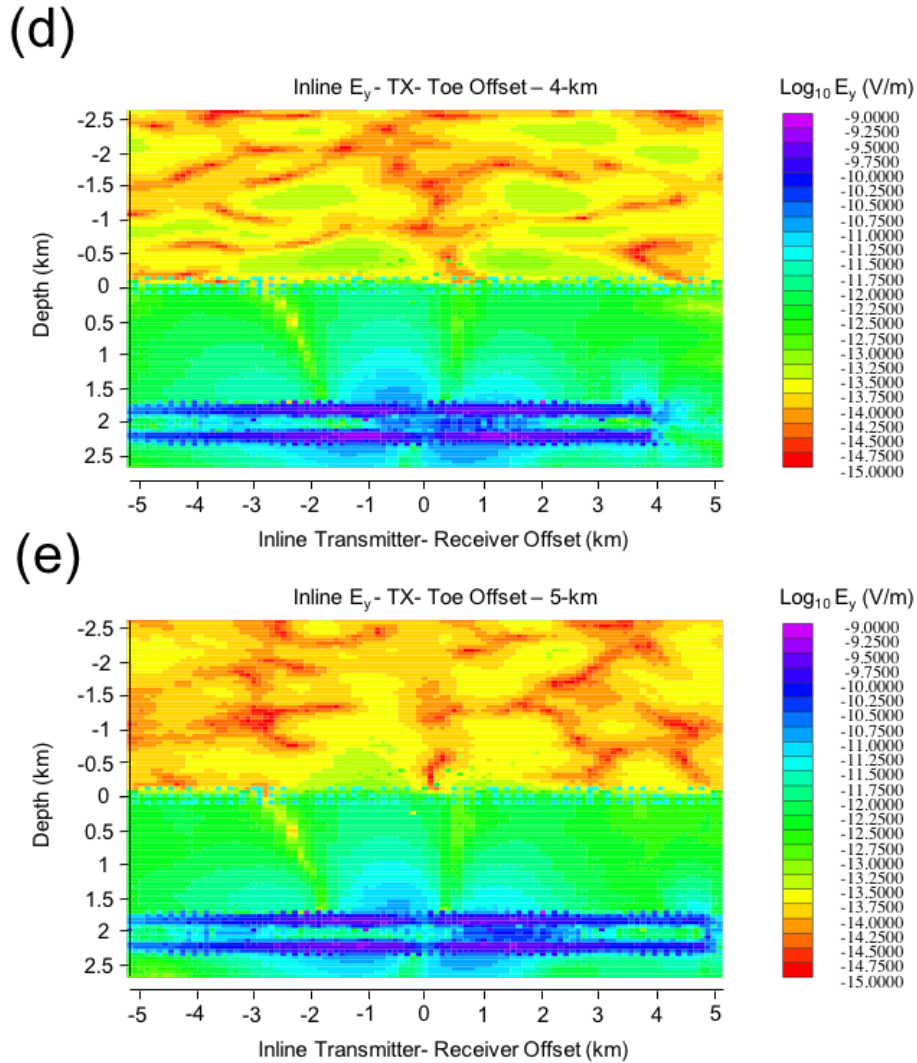
Figure 50 Continued

In the CSEM method, the source operating frequency and the conductivity of the subsurface drive the depth of investigation. The lower the operating frequency, the deeper the investigation. Figure 51 shows the E_y inline patterns in the presence of a lateral wellbore at frequencies of 0.01, 0.05, 0.1, 0.5, 1 and 1.5 Hz. In terrestrial

sediments of conductivity 0.01 S/m, these frequencies correspond to skin depths of 56,

25, 17, 7, 5, and 4 m respectively.
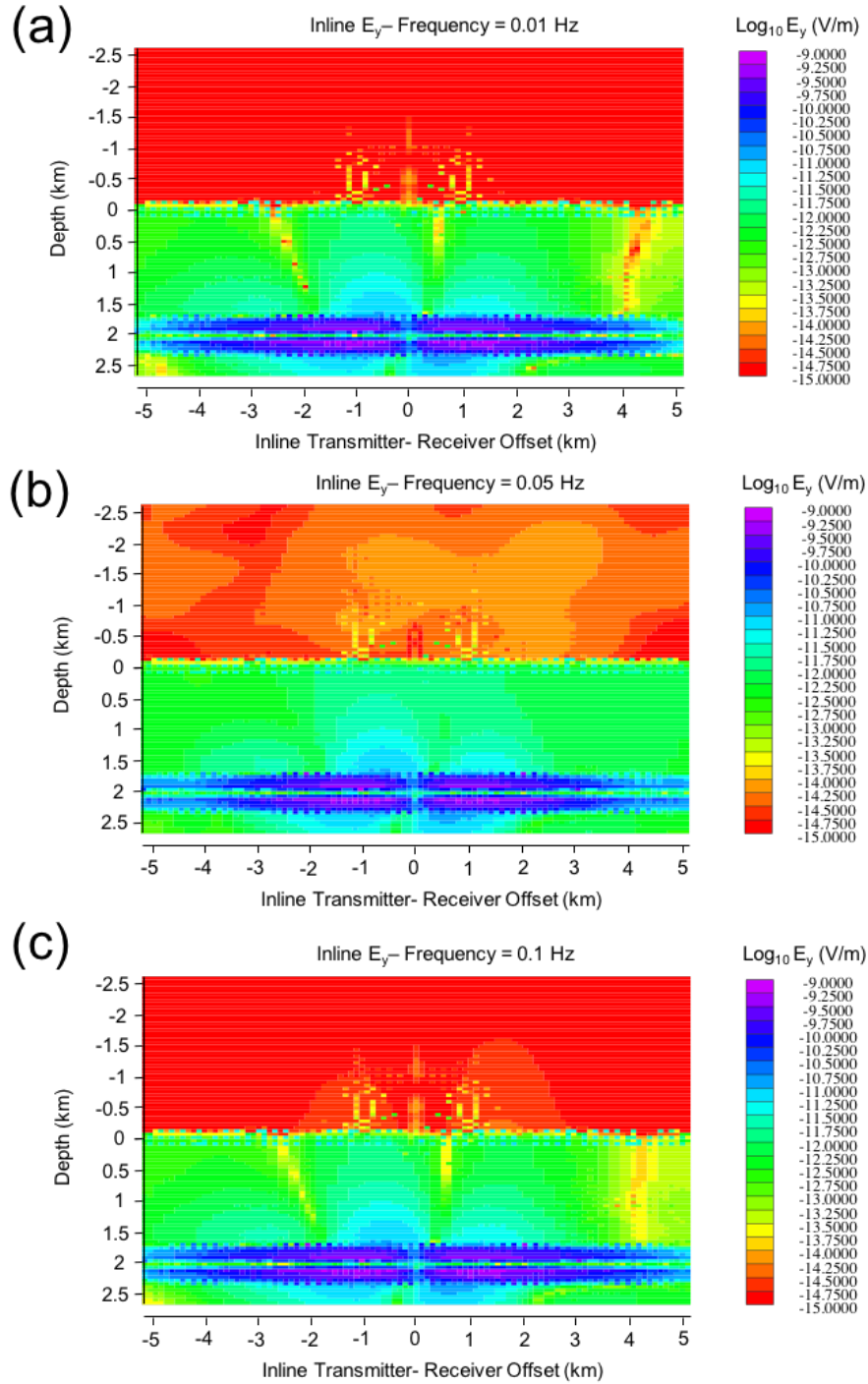
Figure 51 Y-competent electric field patterns for inline orientations for for a geoelectrical model incorporating a lateral wellbore buried beneath 2-km of terrestrial sediments at operating frequencies of 0.01(a), 0.05(b), 0.1(c), 0.5(d), 1(e) and 1.5-Hz (f)
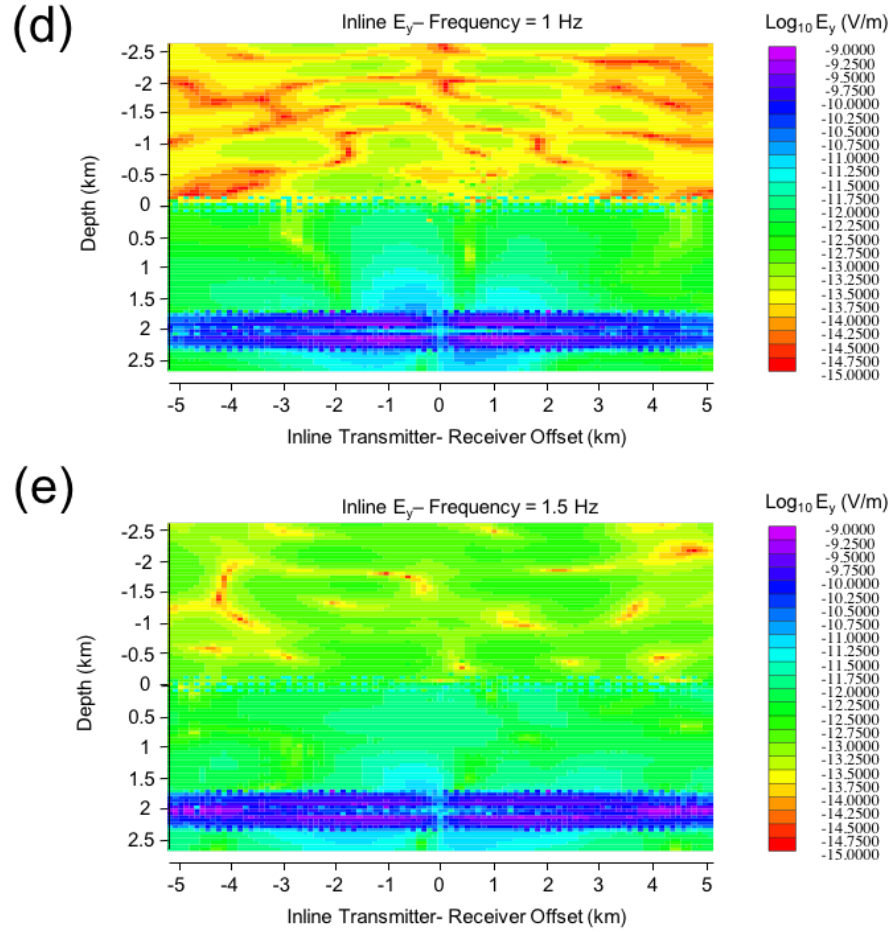
Figure 51 Continued

The field patterns show smaller amplitude in the air layer at lower frequencies due to the increased depth of signal penetration into the subsurface. Furthermore, the effect of the lateral wellbore remains well-defined across the entire frequency range.

Field Patterns Associated with Conductive Fluid-Filled Fracture Zones

I next consider the patterns associated with fluid-filled fracture zones in the absence of a wellbore. The objective is to study field patterns associated with the fluid-filled fracture zone without the interference of a lateral wellbore. In a later section, I will consider models that contain both the lateral wellbore and a fluid-filled fracture zone. The relevant geoelectrical model is shown in Figure 52. The fluid-filled fracture zone, of lateral dimensions as shown in the figure, is buried at 2 km depth and is located at lateral offset 2 km from the transmitter. The corresponding E_x, E_y inline and broadside field patterns are shown in Figures 53 and 54.
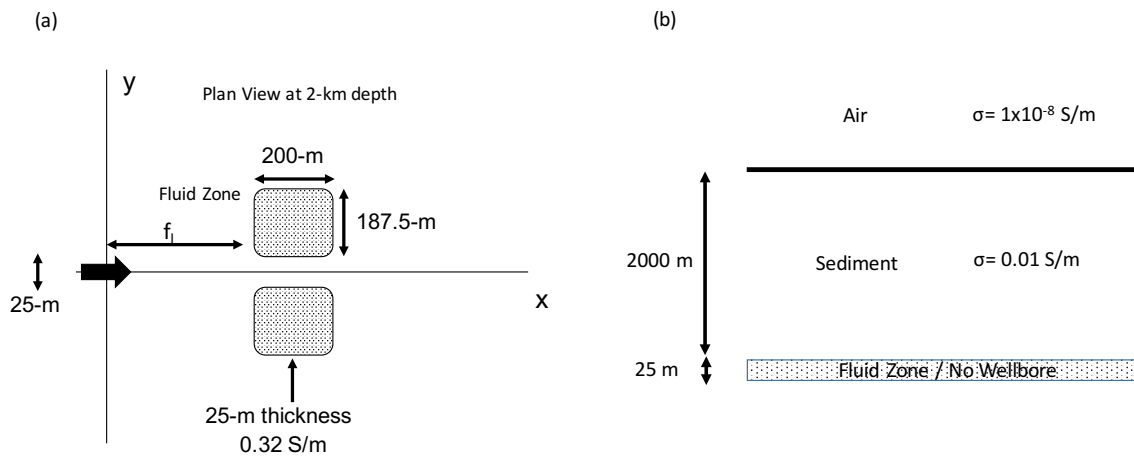
Figure 52 Plan view (a) and geoelectrical model (b) of scenario for determining fluid-filled fracture zones at 2-km depth
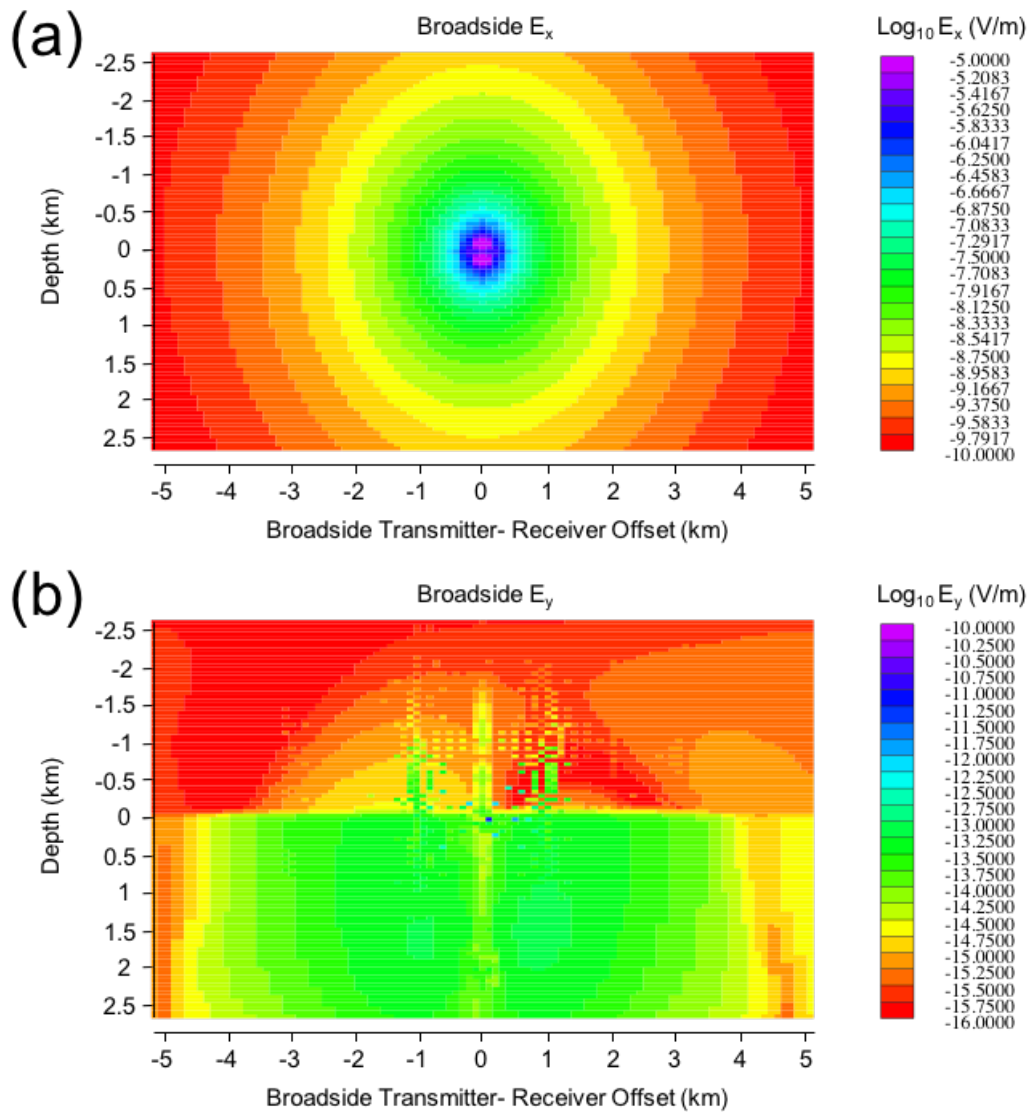
Figure 53 Broadside electric field patterns in the presence of a fluid filled fracture zone at 2-km depth and a lateral offset of 2-km to the transmitter. The field patterns are shown for the x (a) and y(b) components of the electric field
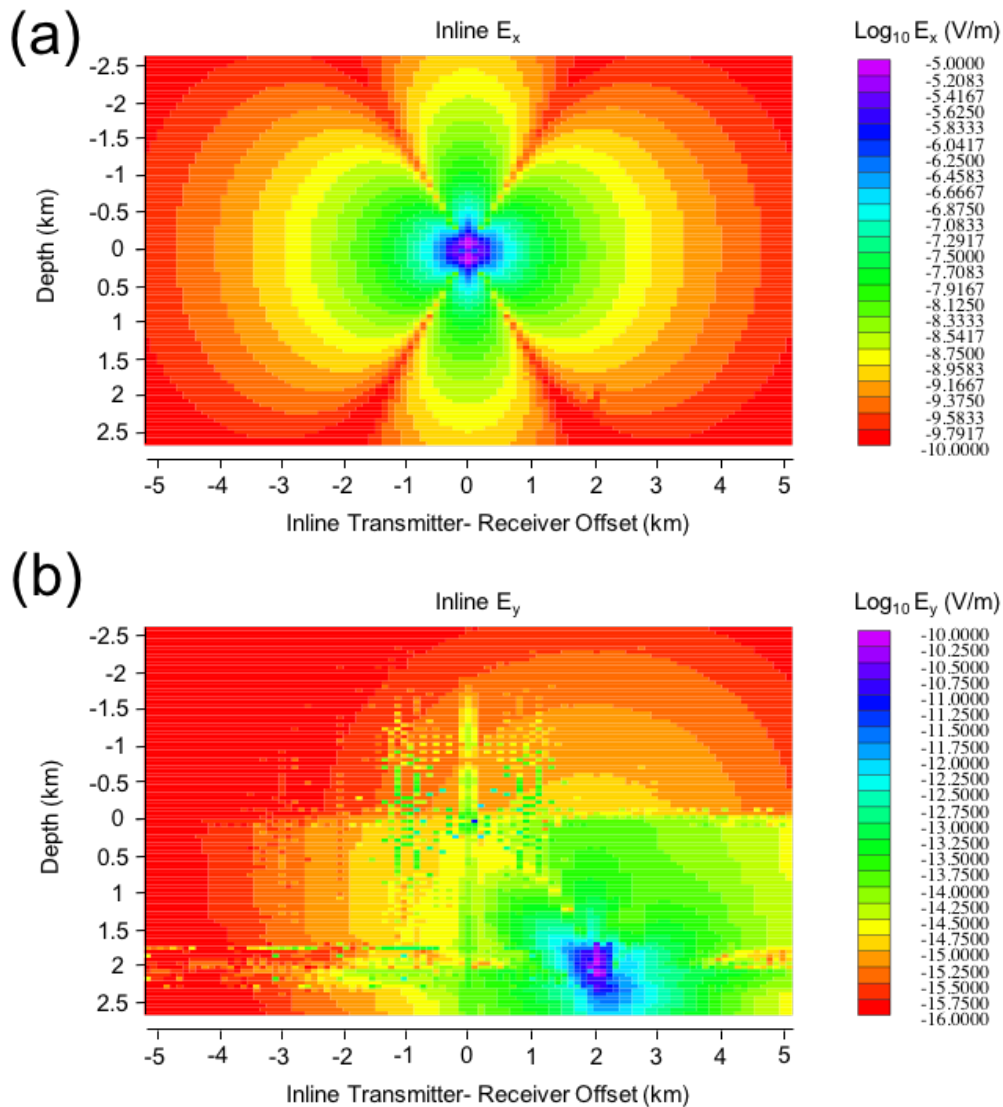
Figure 54 Inline electric field patterns in the presence of a fluid filled fracture zone at 2-km depth and a lateral offset of 2-km to the transmitter. The field patterns are shown for the x (a) and y(b) components of the electric field

The effect of the fluid-filled fracture zone is most evident in the the E_y inline

field pattern. The fluid-filled fracture zone has a much lower conductivity compared to

that of the lateral wellbore. The presence of the fluid-filled fracture zone is difficult to

discern in the E_x field patterns. Recall that the lateral wellbore could be distinguished in

those patterns. The broadside patterns provide no discernable visualization of the fluid-filled fracture zone.

The effect of the fluid-filled fracture zone on the E_y inline field patterns was evaluated as a function of its horizontal offset with respect to the transmitter. Analysis of these scenarios allows me to estimate the spatial resolution of the field patterns. The relevant field patterns are shown in Figure 55 for fluid-filled offsets ranging from 2.0-2.8 km. As the lateral offset increases in 200-m increments, the fluid signature shifts accordingly toward the location of the fluid zone. This observation suggests that the resolution of the CSEM modeling is at least equal to the 200-m interval between fluid-zone locations.
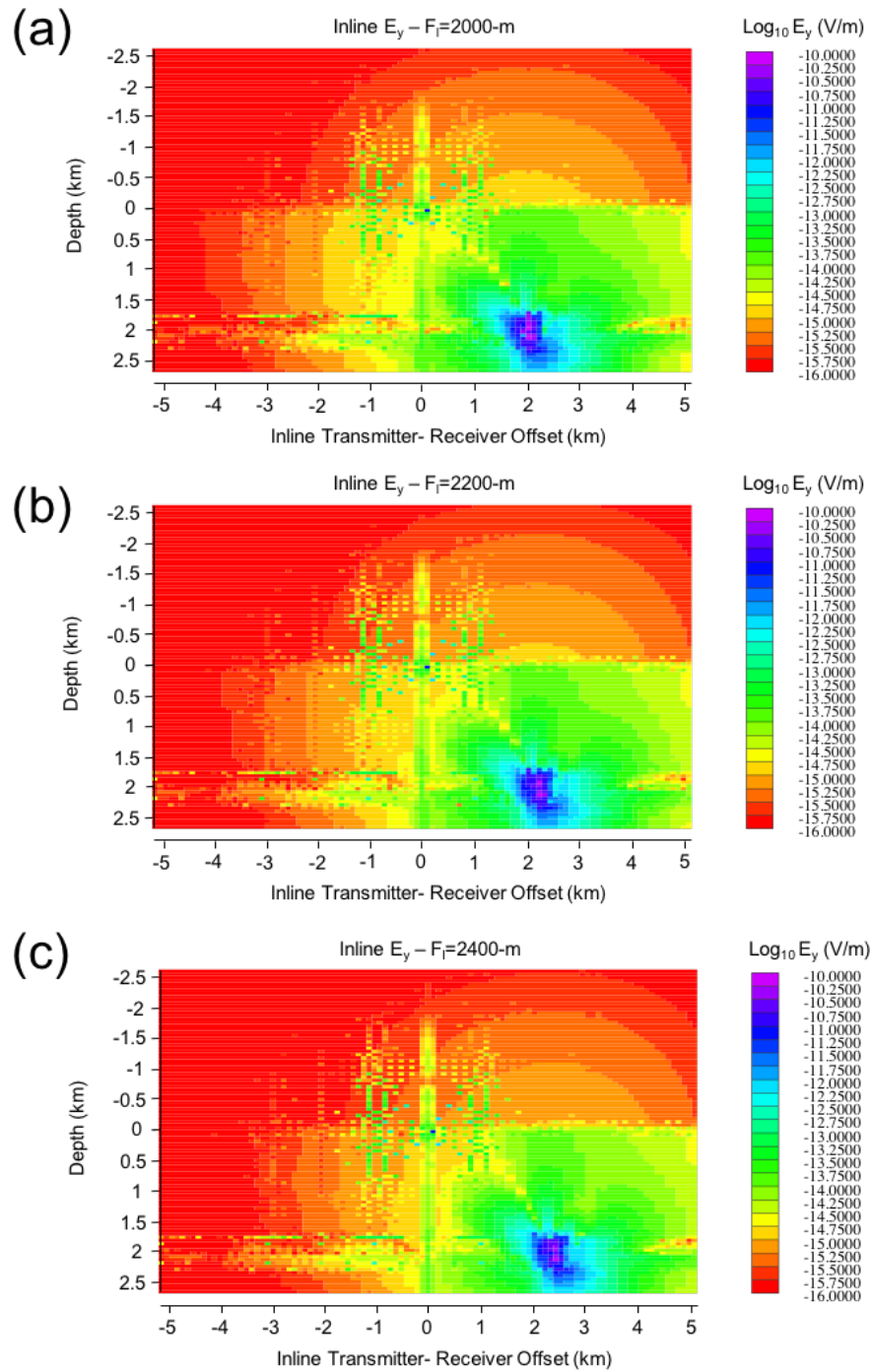
Figure 55 Y-competent electric field patterns for inline orientations for the geoelectrical model shown in figure 52 with fluid-filled fracture zones at lateral offsets of 2000(a), 2200(b), 2400(c), 2600(d) and 2800-m (e)
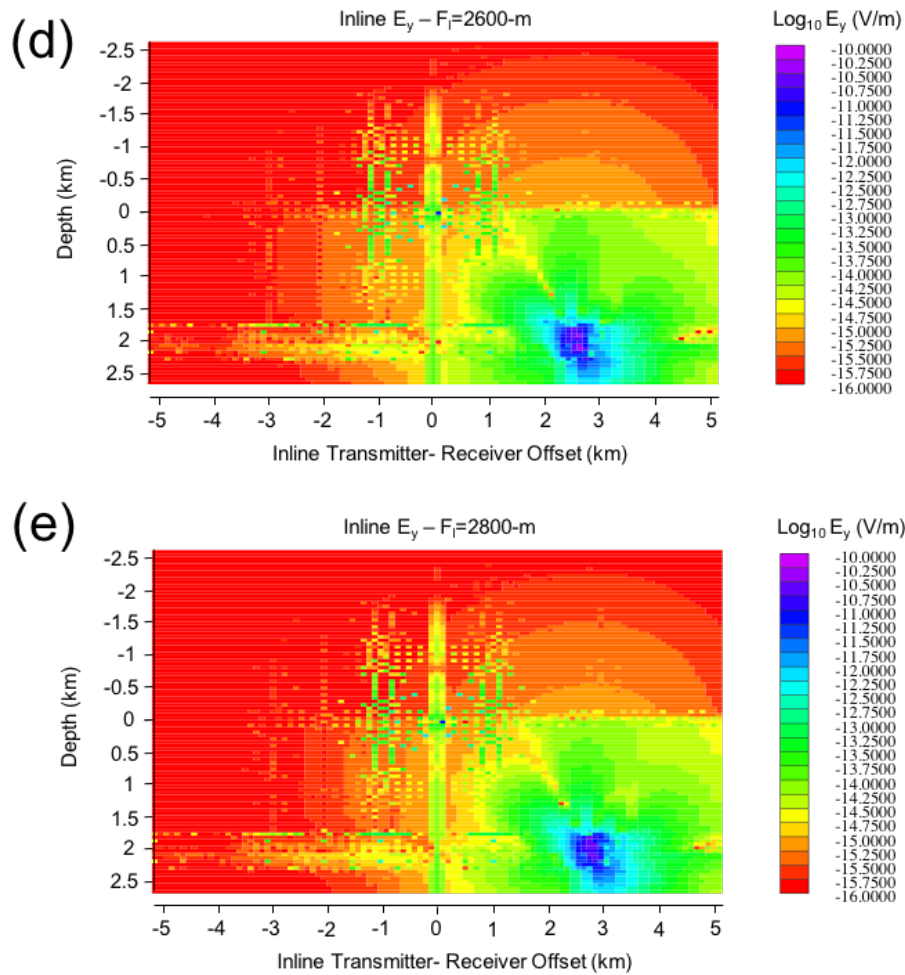
Figure 55 Continued

Following the separate and independent investigations into field patterns

associated with fluid-filled fracture zones and wellbore, I now consider idealized CSEM

modeling in which fluid is forced out of a lateral wellbore at 2 km depth into fracture

zones. The geoelectrical model is shown in Figure 56. The E_x, E_y inline and broadside

field patterns are shown in Figures 57 and 58. In all cases, the patterns are dominated by

the effect of the lateral wellbore, with further prominence of the primary field from the

transmitter in the case of the E_x patterns. To isolate the effect of the fluid on a

background structure that also contains the wellbore, the field patterns associated with

only a wellbore buried at 2 km depth were subtracted from the patterns caused by the

wellbore and the fluid. The residual E_y inline patterns are shown in Figure 59.
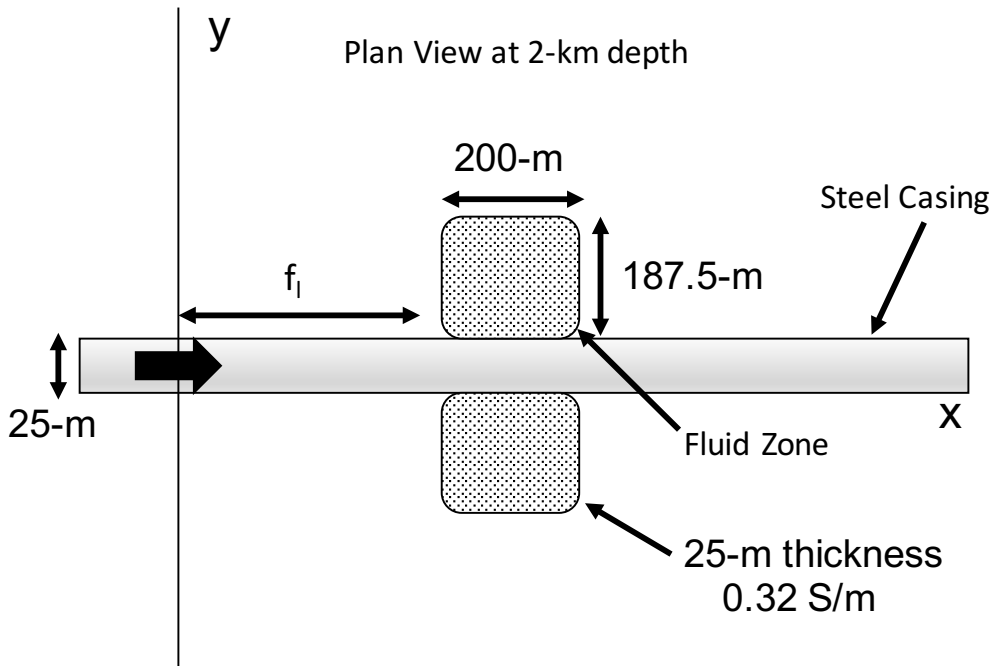
Figure 56 Plan view at 2-km depth for scenario where fluids are being forced out of a lateral wellbore at lateral distance f$_l$ from the transmitter
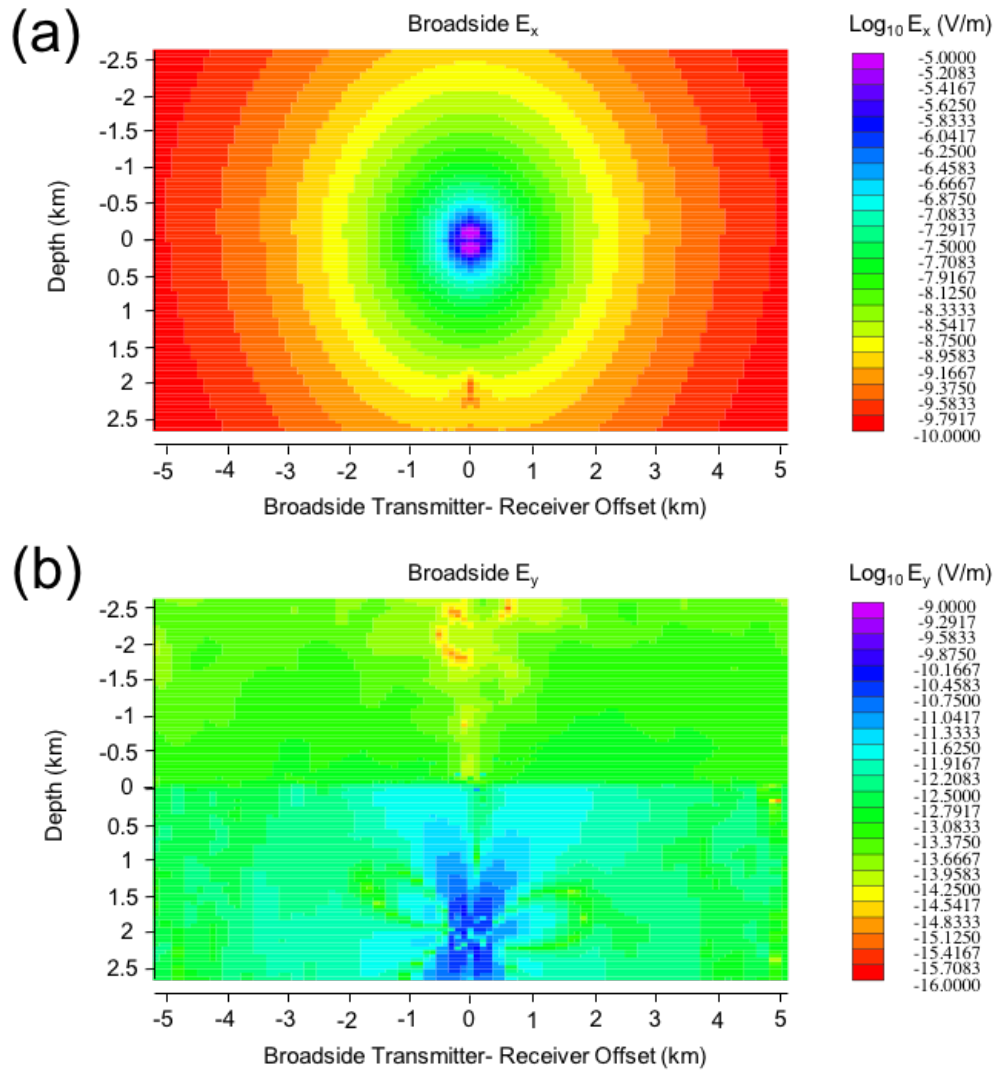
Figure 57 Broadside electric field patterns in the presence of a fluid filled fracture zone at 2-km depth and a lateral offset of 2-km to the transmitter being forced out of a lateral wellbore at 2-km depth. The field patterns are shown for the x (a) and y(b) components of the electric field for the broadside orientation

113
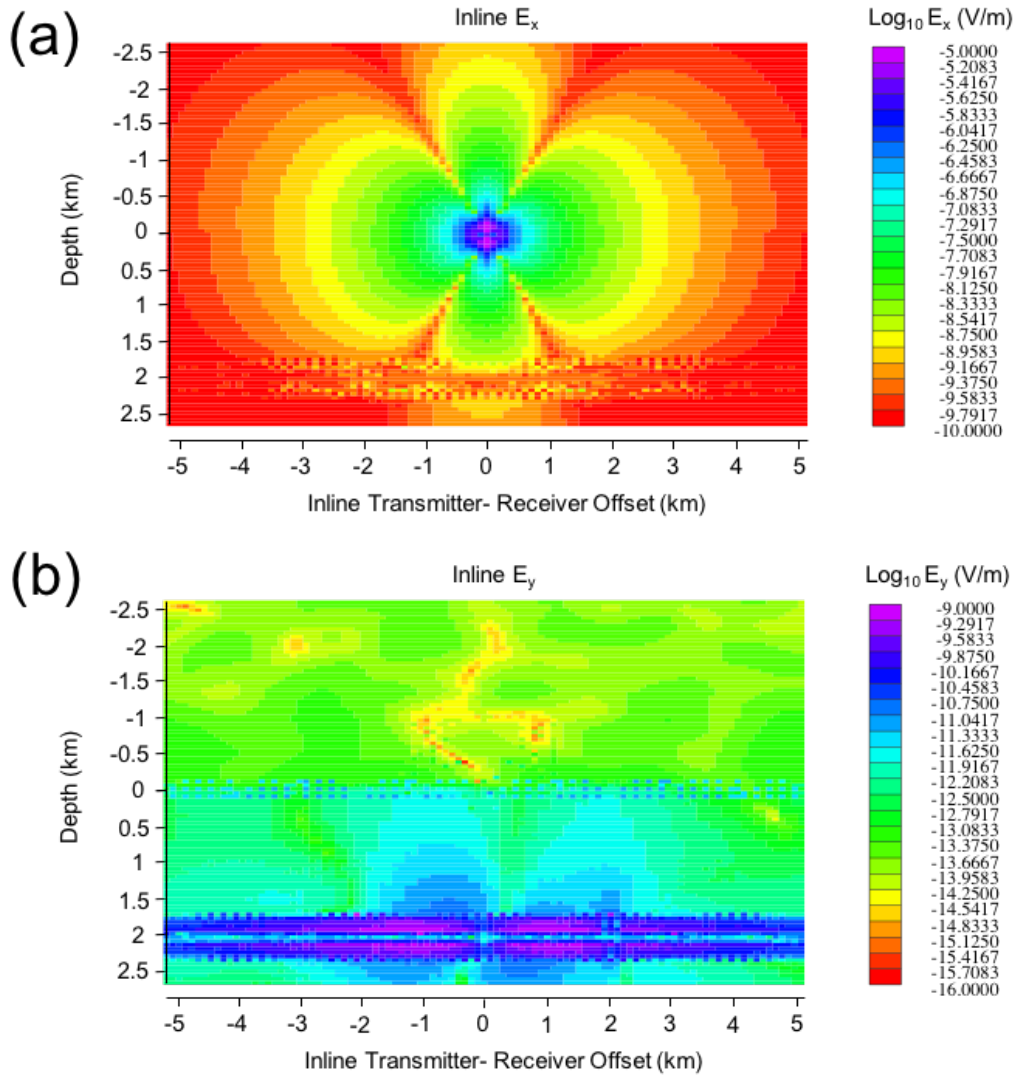
Figure 58 Inline electric field patterns in the presence of a fluid filled fracture zone at 2-km depth and a lateral offset of 2-km to the transmitter being forced out of a lateral wellbore at 2-km depth. The field patterns are shown for the x (a) and y(b) components of the electric field for the inline orientation

The field patterns after the removal of the lateral wellbore effect retain a distinct

signature of the lateral wellbore. As the lateral offset between the transmitter and fluid

filled fracture zone increases, the amplitude of the E_y component associated with the

lateral wellbore diminishes. There is an increased amplitude at 2-km lateral offset and 2-km depth that is likely to due to the fluid–filled fracture zone. These results suggest an effect in which the fluid-filled fracture zones are re-exciting the lateral wellbore, since the original wellbore-only response has been removed. Furthermore the increased amplitude caused by the fluid-filled fracture zone appears at ~2 km regardless of its location. This observation suggests that the lateral resolution of the fracture zone is degraded by its interaction with the lateral wellbore.
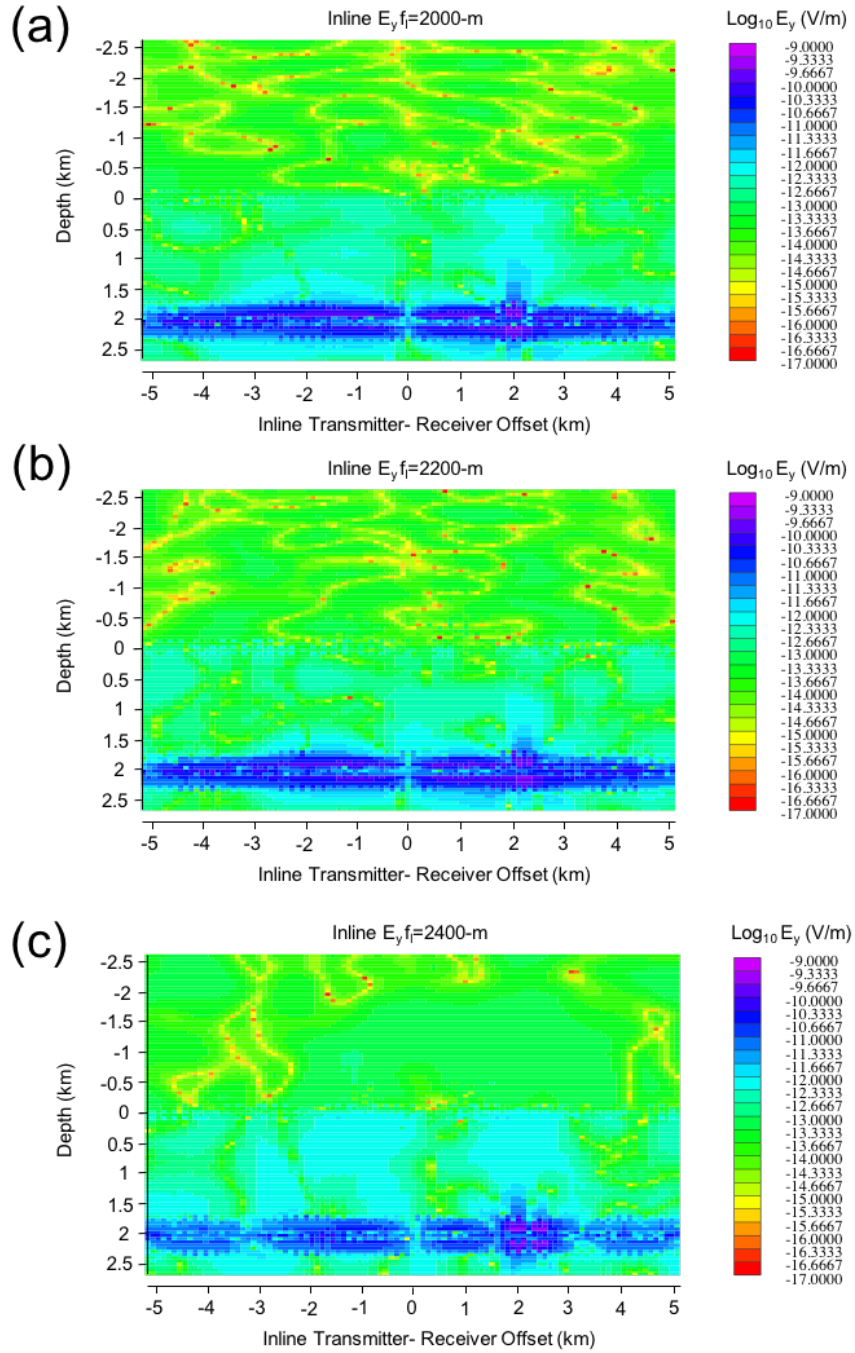
Figure 59 Y-competent electric field patterns for inline orientations for the geoelectrical model shown in figure 56 with fluid-filled fracture zones at lateral offsets of 2000(a), 2200(b), 2400(c), 2600(d) and 2800-m (e), once the electric field patterns associated with a lateral wellbore at 2-km depth have been removed
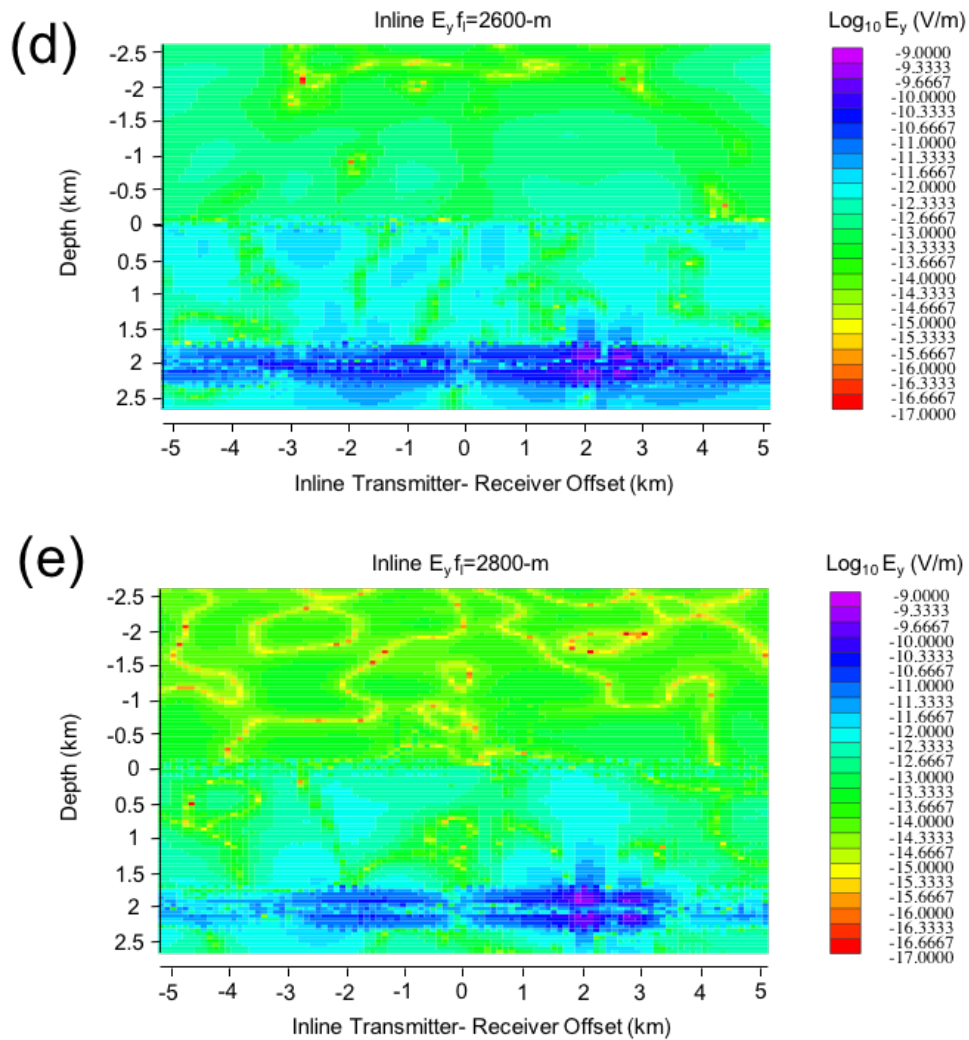
Figure 59 Continued

It is of interest to determine the influence of the conductivity of the fluid-filled fracture zone on CSEM responses. The E_y inline field patterns are shown in Figure 60 for fluid conductivities of 5, 20, 50 and 100 S/m.
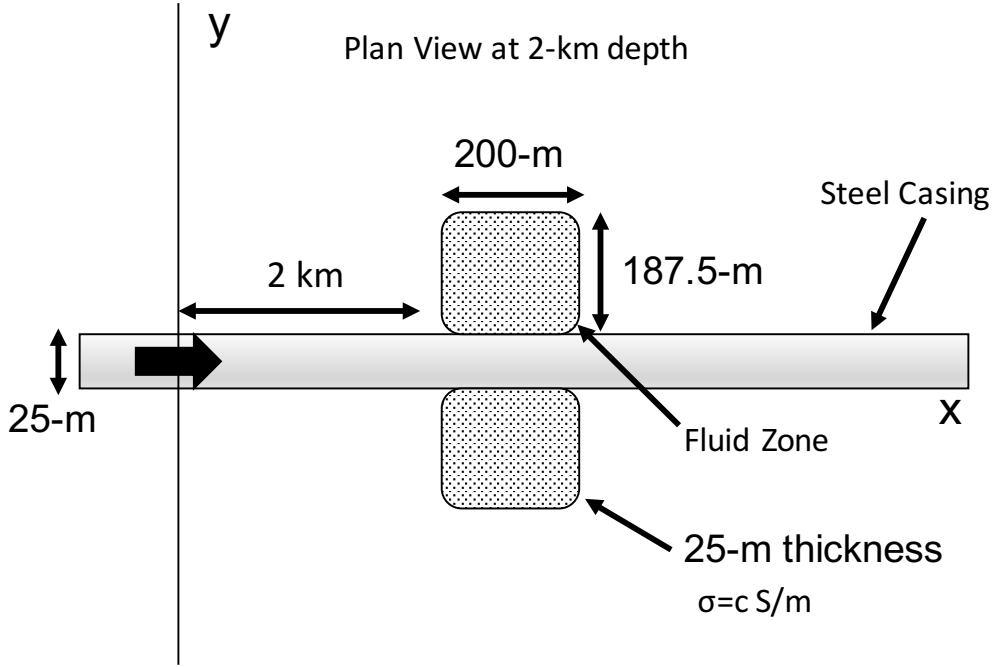
Figure 60 Plan view at 2-km depth for scenario where fluids are being forced out of a lateral wellbore at lateral distance f_l from the transmitter for various fluid conductivities
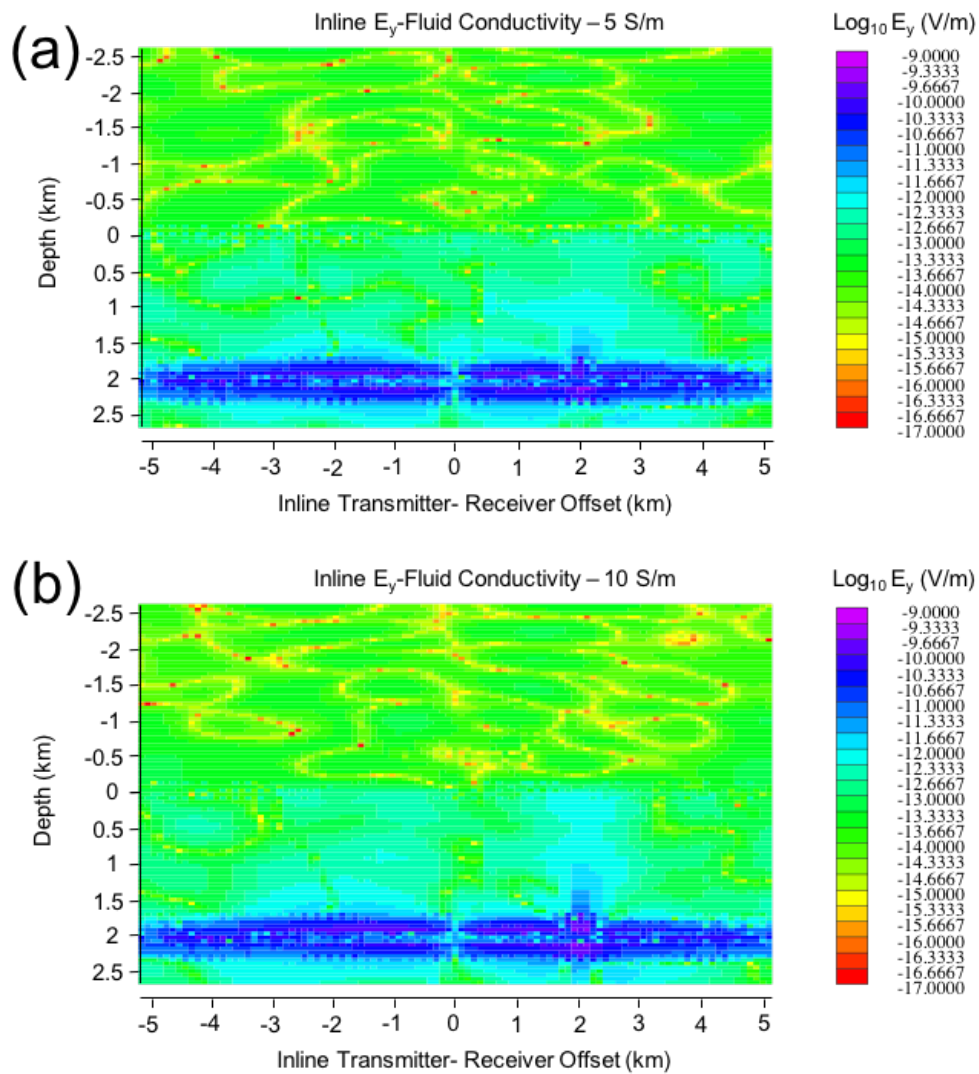
Figure 61 Y-competent electric field patterns for inline orientations for the geoelectrical model shown in figure 60 with fluid-filled fracture zones at lateral offsets of 2000-m, once the electric field patterns associated with a lateral wellbore at 2-km depth have been removed. Results are shown for fluid conductivities of 5(a), 20(b), 50(c) and 100 S/m (d)

Inline E_y-Fluid Conductivity – 50 S/m

Inline E_y-Fluid Conductivity – 100 S/m
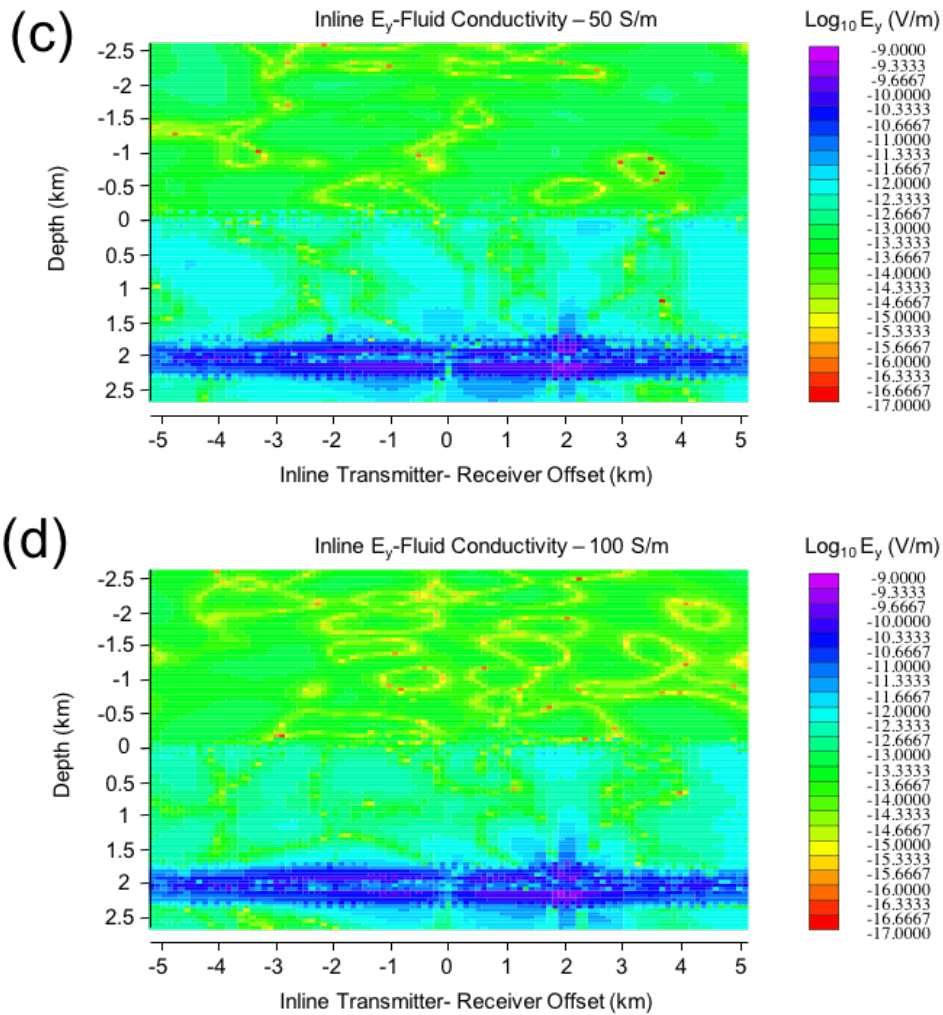
Figure 61 Continued

As fluid conductivity increases, the field amplitude associated with the fluid-

filled fracture zone is enhanced. However the enhancement is minor and and fluids of

lower conductivities generate much the same field pattern as fluids of higher

conductivity. The lateral resolution of the fluid-filled fracture zone does not appear to depend on fluid conductivity.

Discussion

The horizontal electric field patterns have been presented for different modeling scenarios associated with highly idealized CSEM monitoring of hydraulic fracturing. The vertical component E_z is not presented in most of the cases due to difficulties in recording it in practice. The E_x and E_y components of electric field are, respectively, aligned with the transmitter dipole moment and perpendicular to the moment. The E_x component is dominated by the primary field of the transmitter which obscures signatures of buried objects. The E_y component of the electric field is less affected by the primary field and can better reveal layers, wellbore and fluid-filled fracture zones. When modeling marine CSEM signatures in the presence of a buried conductive or resistive layer, I find that the E_x and E_y amplitudes diminish as the water depth decreases. The detection of buried layers is easier in terrestrial or shallow water environments. Furthermore, resistive layers generate a stronger response, particularly in the inline plane (Everett & Chave, 2019). The latter permits easier identification of buried layers, whilst the broadside field patterns respond to the known water depth. For both resistive and conductive layer, the E_y patterns better reveal the buried layers since the E_x patterns are strongly affect the primary field of the transmitter.

The presence of a lateral wellbore is best determined from the E_y patterns. The inline and broadside orientations provide different viewpoints of the highly conductive wellbore. The presence of the lateral wellbore in the E_x inline pattern is obscured by the primary field from the transmitter, and the wellbore signature is also difficult to discern in the broadside plane. The effect of the wellbore decreases with the increasing burial depth but remains evident at 3 km depth.

Where a wellbore toe is introduced, the E_y broadside pattern shows a decrease in amplitude as the wellbore toe moves to greater lateral offsets. The lateral position of the toe can be identified in the inline pattern. There an increase in electromagnetic energy at the wellbore toe since it acts as a secondary source. This explains the decreasing amplitude of the broadside field pattern as the wellbore toe is situated further from the transmitter. The toe is distant from the broadside axis leading to the observed reduction in amplitude in the broadside orientation. Lower frequencies correspond to greater depths of investigation and appear to display a less well-defined wellbore at 2 km depth, whilst higher frequencies produce a better defined wellbore signature.

Fluid-filled fracture zones without the presence of a lateral wellbore have also been modeled. Their effect is largest in the E_y inline field patterns. However, unlike the lateral wellbore signature, the effect of the fluid is not evident in the broadside pattern due to its relatively low conductivity. The fluid-filled fracture zones have a large amplitude at the location of the fluid-filled fracture zone which diminishes with offset from the transmitter. The location of the fluid-filled fracture zone can be determined to within 200 m in these visualizations.

122

When the wellbore and fluid-filled fractures are combined in one geoelectric model. the E_y field pattern is dominated by the wellbore signature. The signal associated with a lateral wellbore at 2 km depth is removed from the combined response. The anticipated result is that the fluid-filled fracture zone signal would be preserved; however, it is found that the signal is still dominated by the effect of the lateral wellbore. There is an increase in amplitude corresponding to the approximate location of the fluid-filled fracture zones; however, the location of the fluid-filled fracture zone is not well-resolved. The persistence of a wellbore signal is suggested to be caused by an interaction of the wellbore and the fluid via their mutual inductance. As the fluid-zone lateral offset increases, the residual electric field associated with the wellbore decreases in amplitude and becomes less well-defined. Increasing the conductivity of the fluid injected has only a slight effect at the location of the fluid-filled fracture zone.

CHAPTER VII

CONCLUSIONS

This dissertation has described highly idealized modeling related to monitoring hydraulic fracturing of unconventional reservoirs using a surface-based controlled-source electromagnetic technique. My work builds upon early terrestrial CSEM modeling studies showing that the electromagnetic response from a grounded–wire dipole source depends sensitively on the transverse resistance (resistivity-thickness) product of a thin oil-bearing layer. The work benefits from recent advances made in CSEM numerical simulations. While the objective of the practical oilfield technology, which is still at an early stage of development, is to image fluid movement away from the wellbore, the objective of my dissertation project is to develop better fundamental understanding which in the future could enable more reliable terrestrial CSEM monitoring. Such an understanding may assist petroleum engineers to detect hydraulic fracture fluids and, if CSEM simulations are coupled to an accurate geomechanical model, eventually to infer the subsurface flow pathways of the electrically conductive injected fluids. However, it must be noted that working oilfields are noisy, complex environments that will always present severe challenges to robust and reliable interpretation of geophysical data.

The 3-D finite element algorithm used to compute the CSEM responses is modified from earlier work that solves Maxwell's equations as formulated in terms of Coulomb-gauged potentials on a cylindrical mesh. The software has been previously

validated for 1-D, 2-D and 3-D structures. I have modified the algorithm to compute

solutions on a rectangular mesh. The change in mesh geometry is useful to represent

geological and other anomalous structures in the subsurface by assigning dimensions and

conductivities to simple slab-like regions.

The rectangular mesh developed for this work was refined insofar as possible

subject to the computational limitations of the resources available . Furthermore the ratio

of mesh lateral to vertical extent proved to be an important consideration. A ratio of 2:1

provided results which were in best agreement with previously published solutions in

marine and terrestrial settings. I confirmed the integrity of the mesh using diagnostics

including 2-D cross-section visualizations and quality factor histograms. A high quality

factor represents well-formed tetrahedra, whilst a low quality factor represents poorly-

formed, long and thin tetrahedra.

Local mesh refinement is used to discretize subsurface bodies whose spatial

dimensions are less than the node spacing. Local refinement enables the analyst to

incorporate long slender objects, such as a wellbore, into the mesh. However, local mesh

refinement requires additional computational memory since the locally refined area

becomes smaller and the overall number of nodes becomes larger. These considerations

also add runtime to the calculation of secondary Coloumb-gauged potentials. A user

must consider time-efficiency and available computational memory when performing

local mesh refinement.

The finite element solver becomes unstable for large conductivity contrasts

between slabs, or between a slab and the host into which it is embedded. This is

important for modeling the CSEM response of a lateral wellbore. A conductance argument is used to discretize a highly conductive, thin steel cased wellbore. By matching its transverse conductance to that of an object with a larger cross-sectional area, I determine the equivalent conductivity of the larger body, hoping this would give an approximation of the CSEM response of the small body. The conductance argument assigns a 25×25-m cross sectional area and reduced conductivity to the modeled wellbore. The conductivity argument produces a family of "equivalent" models that exhibit response curves that are similar in shape but not amplitude. Care must be taken to interpret such responses since I found that they do not exactly reproduce the response of a realistic wellbore.

My numerical results show that a lateral wellbore, modeled using the conductance argument, generates a strong response from a surface-based electric dipole transmitter. Fluid-filled fracture zone responses are of considerably lower amplitude compared to wellbore responses. In both cases, inline responses provide greater signal variability along the profile than broadside responses. The inline response provides information regarding the wellbore depth of burial and the lateral position of fluid zones, when they are modeled separately. Knowledge of the host sediment geoelectrical properties is also important, There is a large difference in amplitude for fluid zone responses in terrestrial vs. marine sediments The former produces a larger fluid-zone response.

Scenarios incorporating both a lateral wellbore and associated fluid zones produce responses with little discernable information regarding the lateral location of a

126

fluid zone. The overall response is dominated by the presence of the highly conductive

wellbore. Upon removing the wellbore response, it is found that the inline responses are

considerably larger than in scenarios with only the fluid zones present. This suggests that

the wellbore acts as an efficient secondary source. Despite the lack of information

regarding the lateral position of the fracture zone, the fluid-zone signature is somewhat

preserved. An important aspect of future work would be to better understand the

complicating effects of mutual inductance between the lateral wellbore and fluid-filled

fracture zones.

The E_x field patterns are dominated by the primary field of the transmitter which

obscures signatures of buried objects. The E_y field patterns are less affected by the

primary field and can better reveal heterogeneities. In a marine setting, E_x and E_y

amplitudes diminish with water depth levels. Resistive layers produce stronger responses

than conductive layers, particularly in the inline vertical plane. The lateral wellbore

signature is most prominent in the E_y field patterns. The signature decreases with

increasing burial depth but remains evident at 3 km burial depth. There is an increase in

electromagnetic energy at the wellbore toe since it acts as a secondary source.

Fluid-filled fracture zones have also been modeled in isolation. Their effect is

largest in the E_y inline field patterns. However, unlike the lateral wellbore signature, the

effect of the fluid is not evident in the broadside pattern. This is due to the relatively low

conductivity of the fluid. The fluid-zone patterns exhibit an anomaly at the correct

location but its amplitude diminishes with offset from the transmitter. The location of

the fluid zone may be determined within 200 m from my field-pattern visualizations.

127

The wellbore and fluid-filled fractures have been combined in a single geoelectric model, and the CSEM response of the composite model has been computed. The E_y field pattern is dominated by the wellbore signature. This is due to the high conductivity of the wellbore. The signal associated with a lateral wellbore at 2 km depth is then removed from the composite response. The naive anticipated result is that the fluid-zone response would be be isolated. However, the residual signal remains dominated by the effect of the lateral wellbore. The persistence of a wellbore signal is suggested to be caused mainly by effects of mutual inductance between the wellbore and the fluid. Further research is required to rigorously test this hypothesis, and to determine any effects of the galvanic coupling between the welbore and the fluid.

All modeling scenarios explored in this dissertation are highly idealized cases wherein the fluid in the fracture zones is assumed to spread geometrically without any fluid-mechanical or geomechanical constraints applied to determine realistic flow paths. Physics-based modelling of the movement of electrically conductive fluid should be performed to generate feasible flow patterns and hence produce more realistic CSEM signatures of the fluid motion. Furthermore, the modeling described herein does not incorporate background noise levels. These are highly variable at oilfields and are difficult to predict. Field studies generally use a long-wire grounded source of large transmitter moment. Such a source can generate a strong signal which, if sufficiently powerful, could overcome a given noise level. The concomitant increase in signal-to-noise ration (SNR) may or may not be sufficient to allow detection of temporal changes in fluid-filled fracture zones during hydraulic fracture operations.

Although it is beyond the scope of this dissertation, CSEM forward modeling efficiency may be improved by porting the algorithms described here to FORTRAN MPI standards, allowing for parallelization using software such as OpenMP. This procedure would enable increased time efficiency, which may make further local mesh refinement of the wellbore and surrounding fluid-filled areas more feasible in more computational memory-rich environments. The stability of the finite-element algorithm may also be improved with more robust preconditioning of the finite-element matrix.

Finally, despite the focus here on terrestrial CSEM for development of unconventional petroleum resources, it is worth mentioning there are many other applications of the technology. The work is applicable with appropriate modifications, for example, to investigate geothermal fluids or groundwater flow as well as CO_2 sequestration and pipeline leak detection. CSEM technology could also be used to infer pathways of conductive nuclear waste through fractures in resistive host rock. The method could also be applicable to subsurface investigations of other planetary bodies. CSEM could be used, for example, as a low-frequency electromagnetic tool for detecting groundwater beneath the surface of Mars.

REFERENCES

(EIA), U. E. I. A., 2016. *Lower 48 states shale plays*. [Online]

Available at: https://www.eia.gov/maps/images/shale_gas_lower48.pdf

(EIA), U. E. I. A., 2017. *U.S Oil Production in three cases*. [Online]

Available at: https://www.eia.gov/todayinenergy/detail.php?id=29932

Aldridge, D. F. et al., 2015. Is a steel-cased borehole an electrical transmission line?. *SEG Technical Program Expanded Abstracts*, pp. 736-741.

Alvarez, P. et al., 2017. Discriminating between commercial and residual hydrocarbon saturation integrating pre-stack seismic and CSEM. *79th EAGE Conference & Exhibition*.

Alvarez, P. et al., 2017. Integrated seismic and CSEM reservoir characterization for de-risking prospects in the Hoop area of the Barents Sea, Norway. *SEG Technical Program Expanded Abstracts*, pp. 3309-3313.

Attias, E. et al., 2014. A marine controlled-source electromagnetic study for the characterization of methane hydrate and free gas reservoirs at the Nyegga CNE03 pockmark, Norwegian Sea. *AGU Fall Meeting Abstract*.

Ayani, M., Mallick, S., Hunziker, J. & MacGregor, L., 2017. Inversion of frequency domain marine controlled-source electromagnetic data using genetic algorithm. *SEG Technical Program Expanded Abstracts*, pp. 1252-1256.

Badea, E. A., Everett, M. E., Newman, G. A. & Biro, O., 2001. Finite-element analysis of controlled-source electromagnetic induction using Coulomb-guaged potentials. *Geophysics,* 66(3), pp. 786-799.

Bannister, P., 1968. Determination of the electrical conductivity of the sea bed in shallow waters. *Geophysics,* 33(6), pp. 995-1003.

Barret, W. M., 1939. *Electrical apparatus and method for geologic studies*. United States of America, Patent No. 2172688.

Bloomer, S., Kowalczyk, P., Constable, S. & Keisuke, E., 2016. Test results and applications of an AUV-borne controlled source electromagentic (CSEM) system. *IEEE/OES Autonomous Underwater Vehicles (AUV),* pp. 90-94.

Bouchara, S. et al., 2015. CSEM based Anisotropy trends in the Barents Sea. *SEG Technical Program Expanded Abstracts,* pp. 879-883.

Brown, V., Key, K. & Singh, S., 2012. Seismically regularized controlled-source electromagnetic inversion. *Geophysics,* 77(1), pp. E57-E65.

Cagniard, L., 1953. Basic theory of the magnetotelluric method of geophysical prospecting. *Geophysics,* Volume 18, pp. 605-635.

Calderon-Moctezuma, A., Gomez-Trevino, E. & Gallardo, L., 2017. Splotting marine controlled-source electromagnetic responses into sea and subseafloor contributions: Grounding the air wave. *Geophysics,* 82(6), pp. E315-E323.

Chave, A. D., 2009. On the electromagentic fields produced by marine frequency domain controlled sources. *Geophysical Journal International,* Volume 179, pp. 1429-1457.

Chave, A. D. & Cox, C. S., 1982. Controlled electromagentic sources for measuring electrical conductivity beneath the oceans. 1. Forward problem and model study. *Journal of Geophysical Research,* Volume 87, pp. 5327-5338.

Chave, A. D., Flosadottir, A. & Cox, C. S., 1990. Some comments on seabed propagation of ULF/ELF electromagnetic fields. *Radio Science,* 25(5), pp. 825-836.

Chave, A. D., Mattsson, J. & Everett, M. E., 2017. On the physics of frequeny domain controlled source electromagentics in shallow water,2:transverse anisotropy. *Geophysics Journal International,* 211(2), pp. 1046-1061.

Colombo, D., Rovetta, D. & Turkoglu, E., 2018. CSEM-regularized seismic velocity inversion: A multiscale, hierarchial workflow for subsalt imaging. *Geophysics,* 83(5), pp. B241-B252.

Constable, S., 2010. Ten years of marine CSEM for hydrocarbon exploration. *Geophysics,* 75(5), pp. 75A67-75A81.

Constable, S., Kannberg, P. K. & Weitemeyer, K., 2016. Vulcan: A deep-towed CSEM reciever. *Geochem, Geophys, Geosyst,* Volume 17, pp. 1042-1064.

Constable, S. & Srnka, L. J., 2007. Special Section - Marine Controlled Source Electromagnetic Methods. An introduction to marine controlled-source electromagentic methods for hydrocarbon exploration. *Geophysics,* 72(2), pp. WA3-WA12.

Cuevas, N. & Pezzoli, M., 2018. On the effect of the metal casing in surface-borehole electromagentic methods. *Geophysics*, 83(3), pp. E173-E187.

Dunham, M. W., Ansari, S. & Farquharson, C. G., 2018. Application of 3D marine controlled-source electromagnetic finite-element forward modeling to hydrocarbon exploration in the Flemish Pass Basin offshore Newfoundland, Canada. *Geophysics,* 83(2), pp. WB33-WB49.

Edwards, R. N. & Chave, A. D., 1986. A transient dipole-dipole method for mapping the conductivity of the seafloor. *Geophysics,* Volume 51, pp. 984-987.

Everett, M. E., 2013. *Near-Surface Applied Geophysics*. s.l.:Cambridge University Press.

Everett, M. E. & Chave, A. D., 2019. Energy flow in terrestrial controlled-source electromagnetic geophysics. *European Journal of Physics,* Volume 40.

Everett, M. E. & Chave, A. D., 2019. On the pysical principles underlying electromagentic induction. *Geophysics,* 84(5), pp. 1-12.

Everett, M. E. & Edwards, R. N., 1993. Transient marine electromagentics: The 2.5-D forward problem. *Geophysical Journal International,* Volume 113, pp. 545-561.

Fernandes, R. A. S., 2008. *The effects of cultural noise on controlled osurce electromagentic responses of subsurface fractures in resistive terrain*, s.l.: Texas A&M University.

Flosadottir, A. H. & Constable, S., 1996. Marine controlled source eletromagnetic sounding 1. Modeling and experimental design. *Journal of Geophysical Research,* Volume 101, pp. 5507-5517.

Freund, R. W., Golub, G. H. & N, M. N., 1992. Interactive solutions of linear systems. In: *Iseries, A., Ed., Acta Numerica.* s.l.:Cambridge University Press, pp. 57-100.

Goswami, B. et al., 2013. CSEM survey of a methane vent site, offshore west Svalbard margin for Arctic gas hydrate quantification. *Stavanger, Polar Petroleum Potential Geosciences.*

Guo, Z., Dong, H. & Kristensen, A., 2017. Image-guided regularization of marine electromagnetic inversion. *Geophysics,* 82(4), pp. 1-66.

Heagy, L., Cockett, R., Oldentberg, D. & Wilt, M., 2015. Modelling electromagentic problems in the presence of cased wells. *SEG Technical Program Expanded Abstracts,* pp. 699-703.

Hibbs, A., 2015. Evaluation of deep subsurface resistivity imaging form hydrofracture monitoring.

Hickey, M. S., Everett, M. E., Helwig, S. L. & Mogilatov, V. S., 2010. The effects of rough terrain on land-based controlled-source electromagnetic exploration using a long horizontal dipole source. *SEG Technical Program Expanded Abstracts,* pp. 3914-3918.

Hickey, M. S., Trevino III, S. & Everett, M. E., 2015. Monitoring and imaging the dynamics and extent of hydraulic fracturing fluid movement using ground-based electromagnetics, with application to the Eagle Ford shale. *Unconventional Resources Technology Conference Paper*.

Hickey, M. S., Trevino III, S. & Everett, M. E., 2017. Monitoring hydraulic fracturing fluid movement using ground-based electromagnetics, with applications to the Anadarko basin and the Delaware basin/NW Shelf. *Unconventional Resources Technology Conference Paper*.

Hoverston, G. M. et al., 2015. Field test of sub-basalt hydrocarbon exploration with marine controlled source electromagnetic and magnetotelluric data. *Geophysical Prospecting,* Volume 63, pp. 1284-1310.

Keller, G. V., 1969. Electromagnetics may be the key to direct oil finding. *World Oil,* pp. 85-88.

Kim, J., Um, E. S. & Moridis, G. J., 2014. Fracture propagation, fluid flow and geomechanics of water-based hydraulic fracturing in shale gas systems and electromagnetic monitoring of fluid migration. *SPE Hydraulic Fracturing Technology Conference Paper*.

Kohnke, C., Lui, L., Streich, R. & Swidinsky, A., 2018. A method of moments approach to model the electromagnetic response of multiple steel casings in a layered earth. *Geophysics,* 83(2), pp. WB81-WB96.

Liu, S. & Joe, B., 1996. Quality local refinement of tetrahedral meshes based on 8-subtetrahedron subdivision. *Mathematics of Computation,* 65(215), pp. 1183-1200.

MacGregor, L. M., Constable, S. & Sinha, M. C., 2001. Electrical resistivity structure of the Valu Fa Ridge, Lau Basin, from marine controlled-source electromagentic sounding. *Geophysical Journal International,* Volume 146, pp. 217-236.

Myer, D. et al., 2012. Marine CSEM of the Scarbrough gas field, Part 1: Experimental design and data uncertrainty. *Geophysics,* 77(4), pp. E281-E299.

Myer, D., Key, K. & Constable, S., 2015. Marine CSEM of the Scarbrough gas field, Part 2: 2D inversion. *Geophysics,* 80(3), pp. E187-E196.

Newman, G. A. & Alumbaugh, D. L., 1995. Frequency-domain modelling of airborne electromagnetic responses using staggered finite differences. *Geophysical Prospecting,* Volume 43, pp. 1021-1042.

Parker, R. & Shure, L., 1988. *PLOTXY: A versatile plot program*. s.l.:s.n.

Passalacqua, H., 1981. *Electromagnetic fields due to a this resistive layer,* s.l.: Colorado School of Mines.

Passalacqua, H., 1983. Electromagnetic fields due to a thin resistive layer. *Geophysical Prospecting,* Volume 31, pp. 945-976.

Patzer, C., Tietze, K. & Ritter, O., 2017. Steel-cased wells in 3-D controlled source EM modelling. *Geophysical Journal International,* Volume 209, pp. 813-826.

Puzyrev, V. et al., 2017. Three-dimensional modeling of the casing effect in onshore controlled-source electromagnetic surveys. *Surveys in Geophysics,* Volume 38, pp. 527-545.

Rust, W. M., 1938. A historical review of electrical prospecting methods. *Geophysics,* Volume 3, pp. 1-6.

Schaller, A. et al., 2017. A land-based controlled-source electromagnetic method for oil field exploration: An example from the Schoonebek oil field. *Geophysics,* 83(2), pp. Wb1-WB17.

Schlumberger , C., Schlumberger, M. & Leonardon, E. G., 1934. Electrical exploration of water-covered areas. *Transactions of the American Institute of Mining and Metallurgical Engineers*, Volume 110, pp. 122-134.

Sherman, D., Kannberg, P. & Constable, S., 2017. Surface towed electromagentic system for mapping of subsea Arctic permafrost. *Earth and Planetary Science Letters*, Volume 460, pp. 97-104.

Sinha, M. C. et al., 1990. An active source EM sounding system for marine use. *Marine Geophysical Research,* Volume 12, pp. 59-68.

Stalnaker, J., 2004. *A finite element approach to the 3D CSEM modeling problem and applications to the study of target interaction adn topography,* s.l.: Texas A&M University.

Streich, R., 2016. Controlled-source electromagentic approaches for hydrocarbon exploration and monitoring on land. *Surveys in Geophysics,* Volume 37, pp. 47-80.

Thiel, S., 2017. Electromagnetic monitoring of hydraulic fracturing: Relationship to permeability, seismicity and stress. *Surveys in Geophysics,* Volume 38, pp. 1133-1169.

Tietze, K. et al., 2016. Borehole controlled-source electromagentics for hydrocarbon saturation monitoring in the Bockstedt oil field, onshore northwest Germany. *Abu Dhabi International Petroleum Exhibition and Conference Paper*.

Tietze, K., Ritter, O. & Veeken, P., 2015. Controlled-source electromagnetic monitoring of reservoir oil saturation uing a novel borehole-to surface configuration. *Geophysical Prospecting,* Volume 63, pp. 1468-1490.

Um, E. S. & Alumbaugh, D. L., 2007. Special section-Marine controlled-source electromagnetic methods. On the physics of the marine controlled-source electromagentic method. *Geophysics,* 72(2), pp. WA13-WA26.

Um, E. S. & Kim, J., 2016. Application of electrical and electromagnetic geophysical methods for detecting hydraulically-active fractured zones. *American Rock Mechanics Association Extended Abstract*.
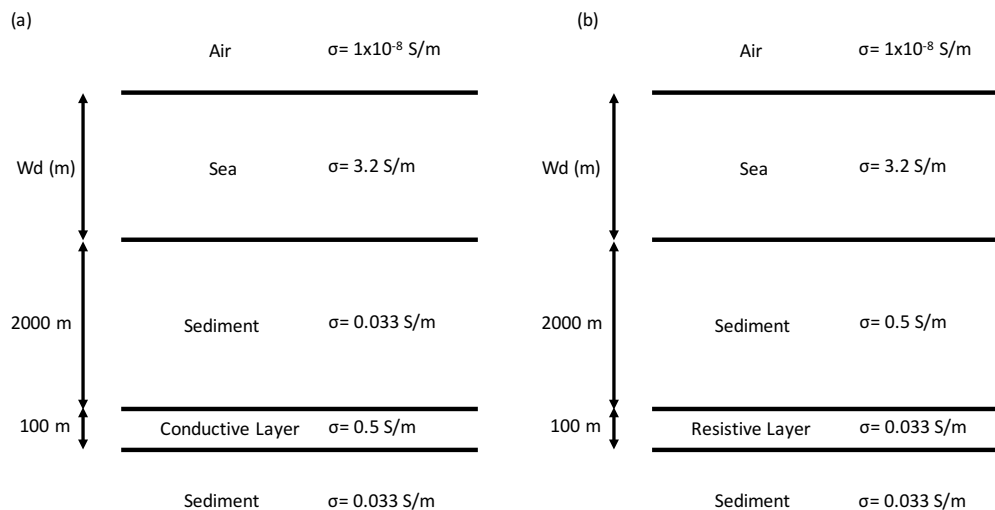
Unsworth, M. J., Travis, B. J. & Chave, A. D., 1993. Electromagnetic induction by a finite electric dipole source over a 2-D earth. *Geophysics,* Volume 58, pp. 198-214.

Vozoff, K., 1990. Magnetotellurics: Principles and practice. *Proceedings of the Indian Academy of Sciences-Earth and Planetary Sciences,* 99(4), pp. 441-471.

Ward, S. H. & Hohmann, G. W., 1987. Electromagnetic theory for geophysical applications. In: *Electromagnetic methods in applied geophysics*. s.l.:s.n., pp. 131-311.

Weiss, C. J. et al., 2016. Electromagnetic measurements in an active oilfield environment. *Geophysics,* Volume 72(6), pp. A93-A97.

Weiss, C. J., 2007. The fallacy of the 'shallow-water problem' in marine CSEM exploration. *AGU Fall Meeting Abstract*.

Weiss, C. J. & Wilson, G. A., 2017. Modeling the electrical response of oilfield infrastructure. *SEG Technical Program Expanded Abstracts,* pp. 1064-1069.

Weitemeyer, K., Constable, S., Shelander, D. & Haines, S., 2017. Mapping the resistivity structure of Walker Ridge 313 in the Gulf of Mexico using the marine CSEM method. *Marine and Petroleum Geology,* Volume 88, pp. 1013-1031.

Yang, Y. et al., 2018. Denoising controlled-source electromagnetic data using least-squares inversion. *Geophysics,* 83(4), pp. 1942-2156.

APPENDIX A

MODELING RESULTS FOR DIMINISHING WATER DEPTHS-BURIED

RESISITVE LAYER

In order to understand electromagnetic field patterns associated with buried steel casings and associated fluid ejection, I first consider the patterns associated with conventional layered earth models. I use the geoelectrical models shown in figure 62 to represent a buried conductive or resistive layer. Furthermore I consider these models for diminishing water depths ranging from a deep-water marine case of water depth 2 km to a terrestrial setting, which is the limiting case of zero water depth. This appendix discusses the field patterns associated with figure 62b For information regarding a buried conductive layer please see chapter 6.

(a)			(b)		
	Air	$\sigma = 1\times10^{-8}$ S/m		Air	$\sigma = 1\times10^{-8}$ S/m
Wd (m)	Sea	$\sigma = 3.2$ S/m	Wd (m)	Sea	$\sigma = 3.2$ S/m
2000 m	Sediment	$\sigma = 0.033$ S/m	2000 m	Sediment	$\sigma = 0.5$ S/m
100 m	Conductive Layer	$\sigma = 0.5$ S/m	100 m	Resistive Layer	$\sigma = 0.033$ S/m
	Sediment	$\sigma = 0.033$ S/m		Sediment	$\sigma = 0.033$ S/m

Figure 62 Geoelctrical model for cases with varying water depths including a buried conductive layer (a) and resistive buried layer (b)

I calculate various electromagnetic field components and visualize the field patterns in two dimensions on different orientations of a vertical plane. The inline and broadside planes, in particular, provide complementary images of the associated field patterns. Figures 63 & 64 shows the layered-earth field patterns associated at water depth 1 km for the resistive layer case. The components $E_x E_y, E_z$ in the inline and broadside vertical planes are shown.
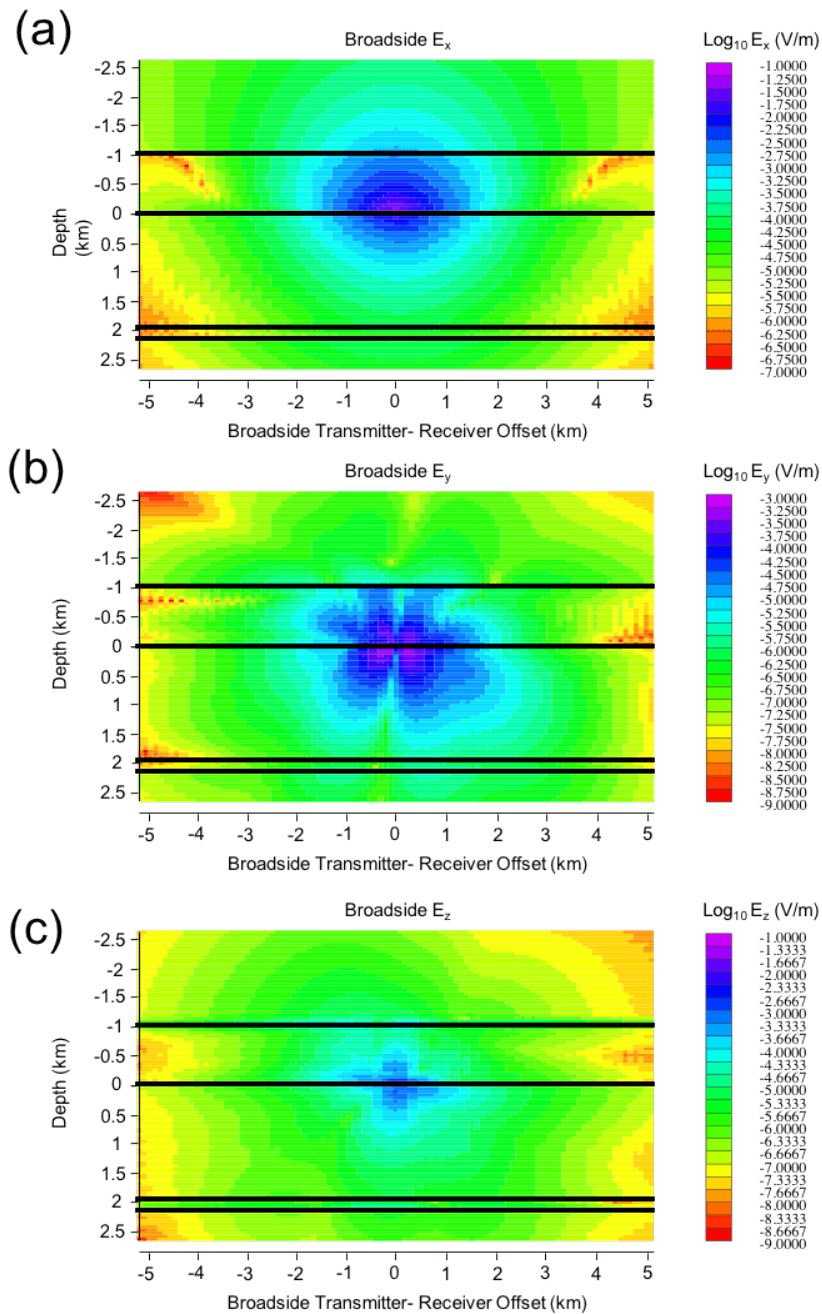
Figure 63 Broadside electric field patterns for each electric field component associated with the geoelectrical model shown in figure 63b for a water depth of 1-km. The annotated lines represent the boundary between the air and water layers, the boundary between the water layer and sediment and the two boundaries between the sediment and the resistive layer as seen from top to bottom

142
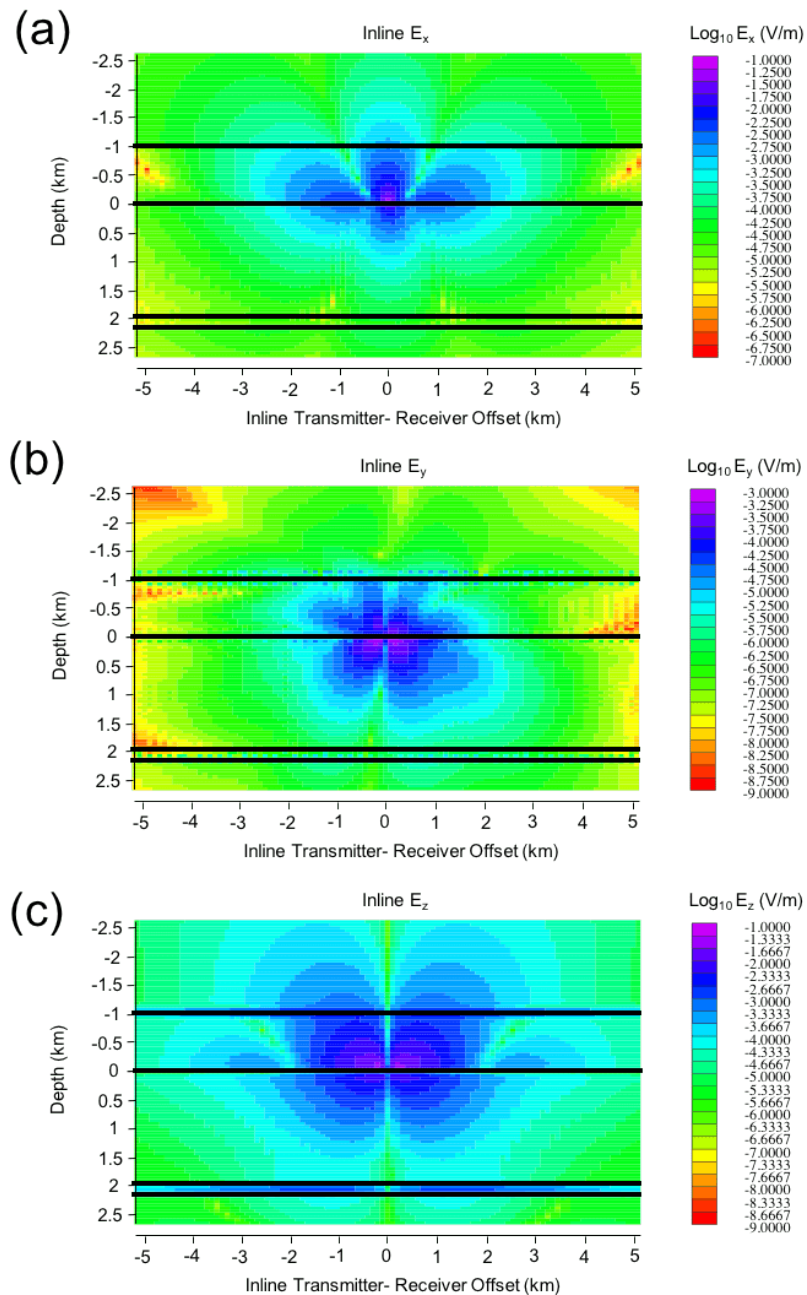
Figure 64 Inline electric field patterns for each electric field component associated with the geoelectrical model shown in figure 63b for a water depth of 1-km. The annotated lines represent the boundary between the air and water layers, the boundary between the water layer and sediment and the two boundaries between the sediment and the resistive layer as seen from top to bottom

143

Figures 63-64 show the field patterns associated with the geoelectrical model of figure 62b for variable water depth. There are advantages to examining each electric field component and orientation of view when attempting to detect the effects of layering in the field patterns. For instance, the resistive layer is more recognizable in the inline orientation.
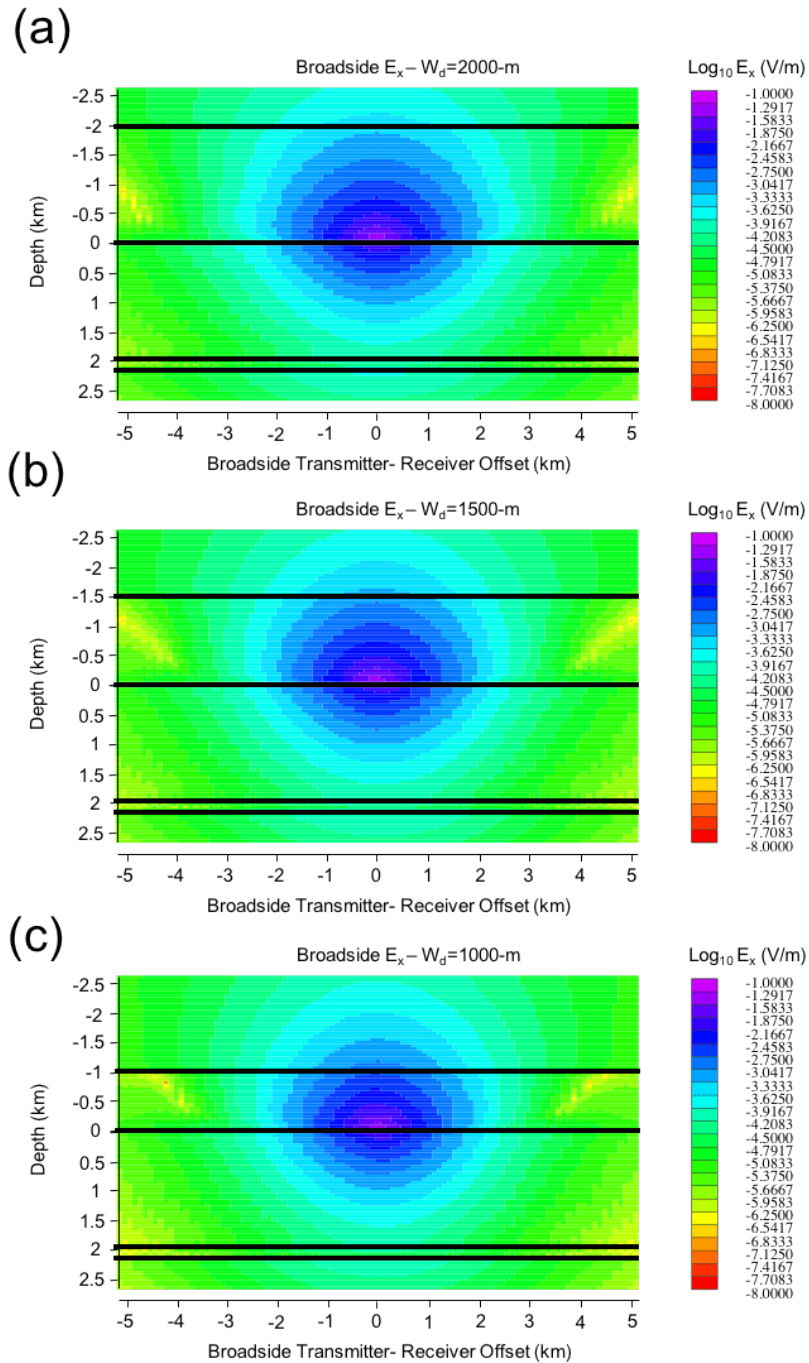
Figure 65 Broadside E$_x$ component for water depths of 2000 (a), 1500 (b), 1000 (c), 800 (d), 400 (e), 200 (f), 100 (g) and 0-m (h). The annotated lines represent the boundary between the air and water layers, the boundary between the water layer and sediment and the two boundaries between the sediment and the resistive layer as seen from top to bottom
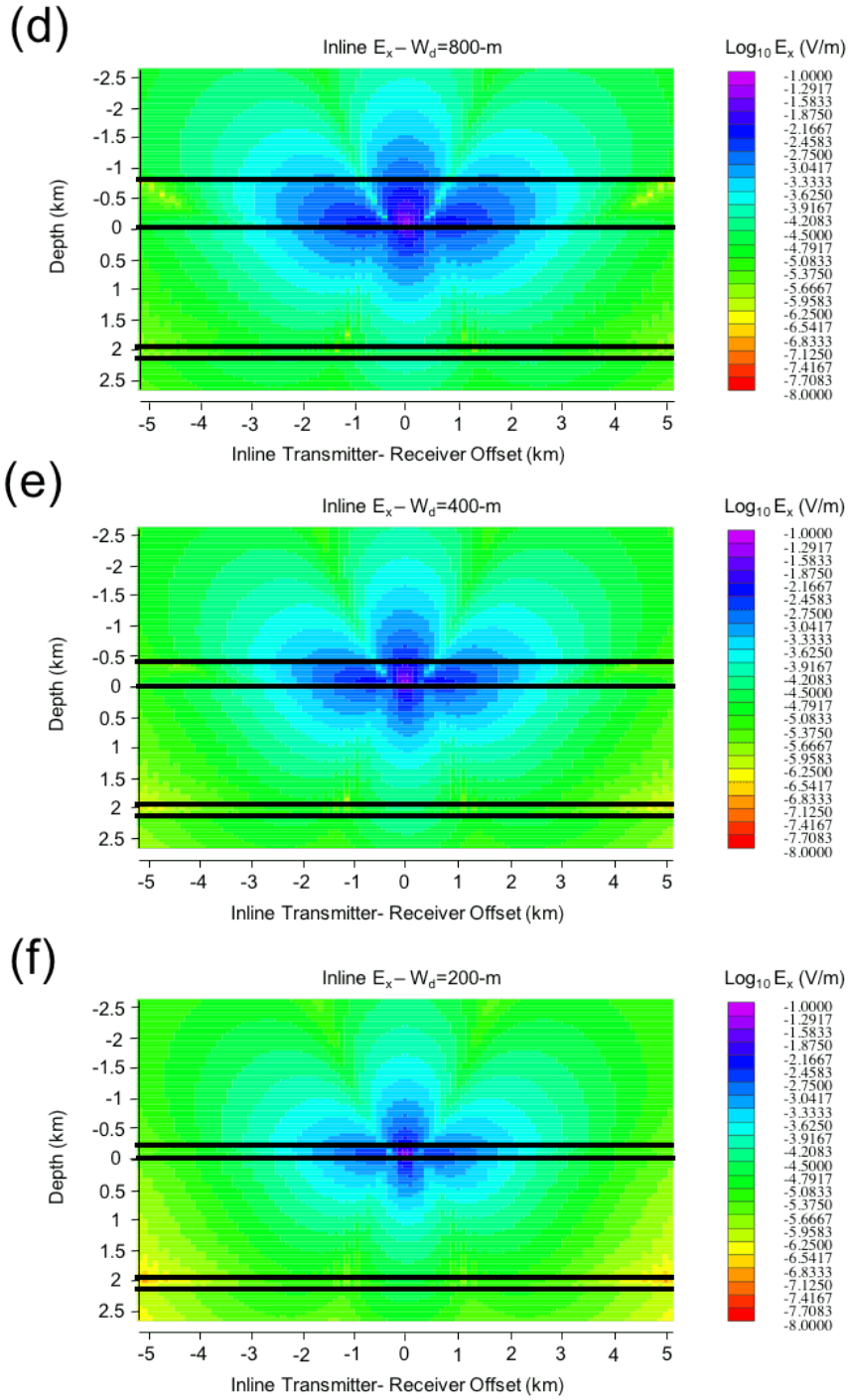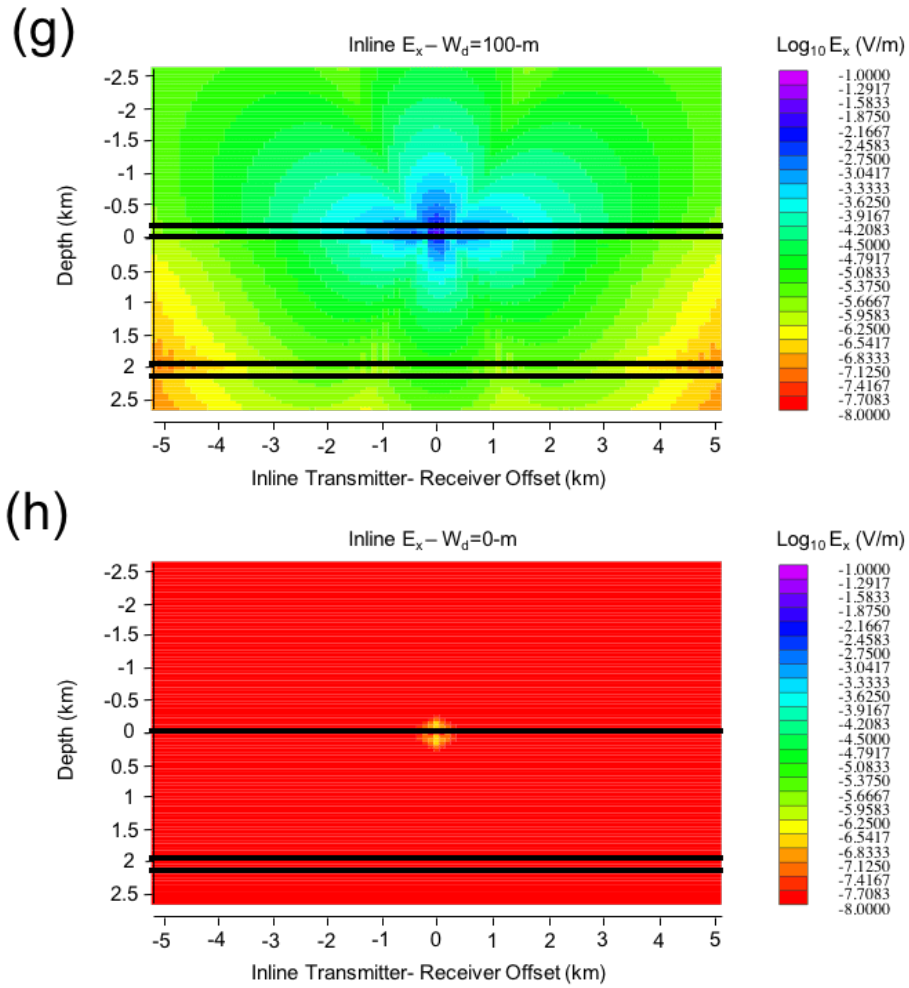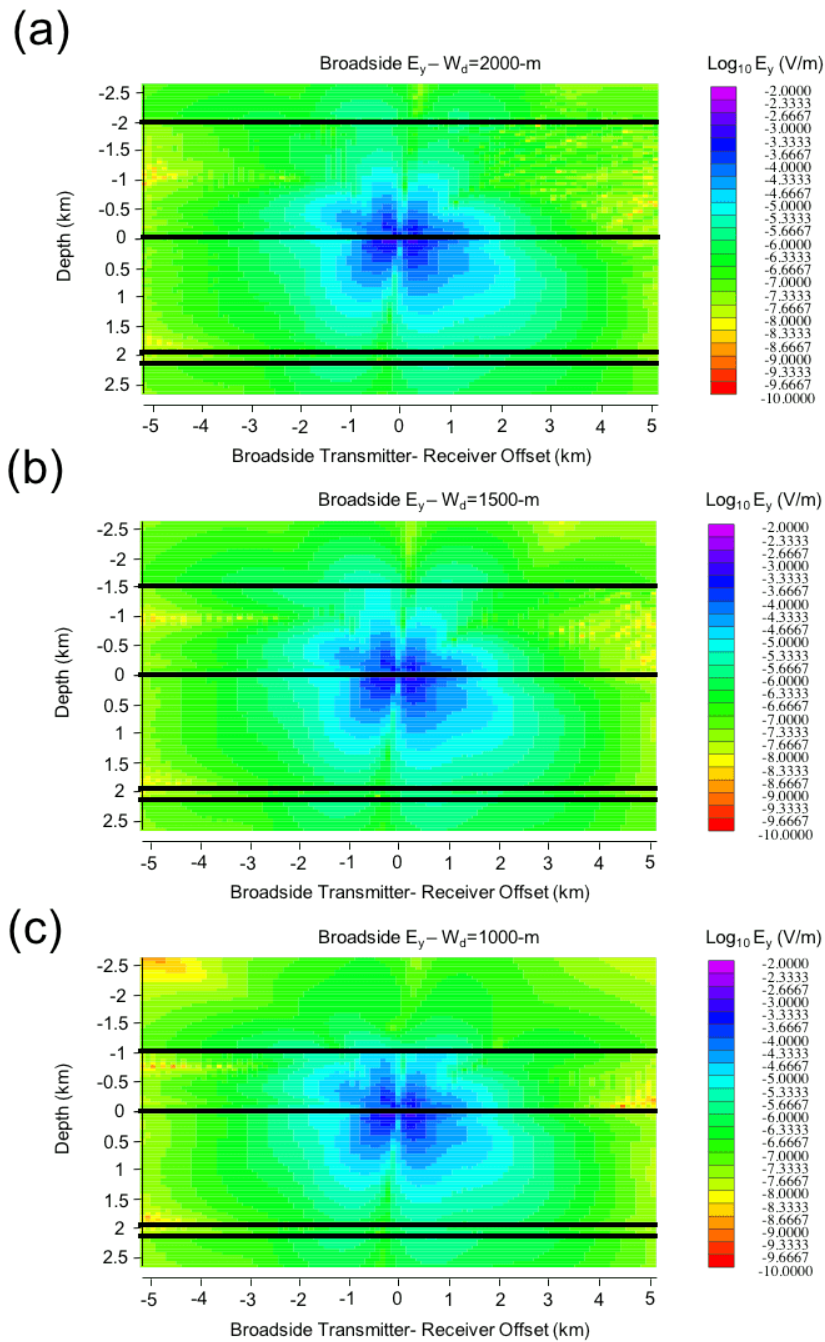
145
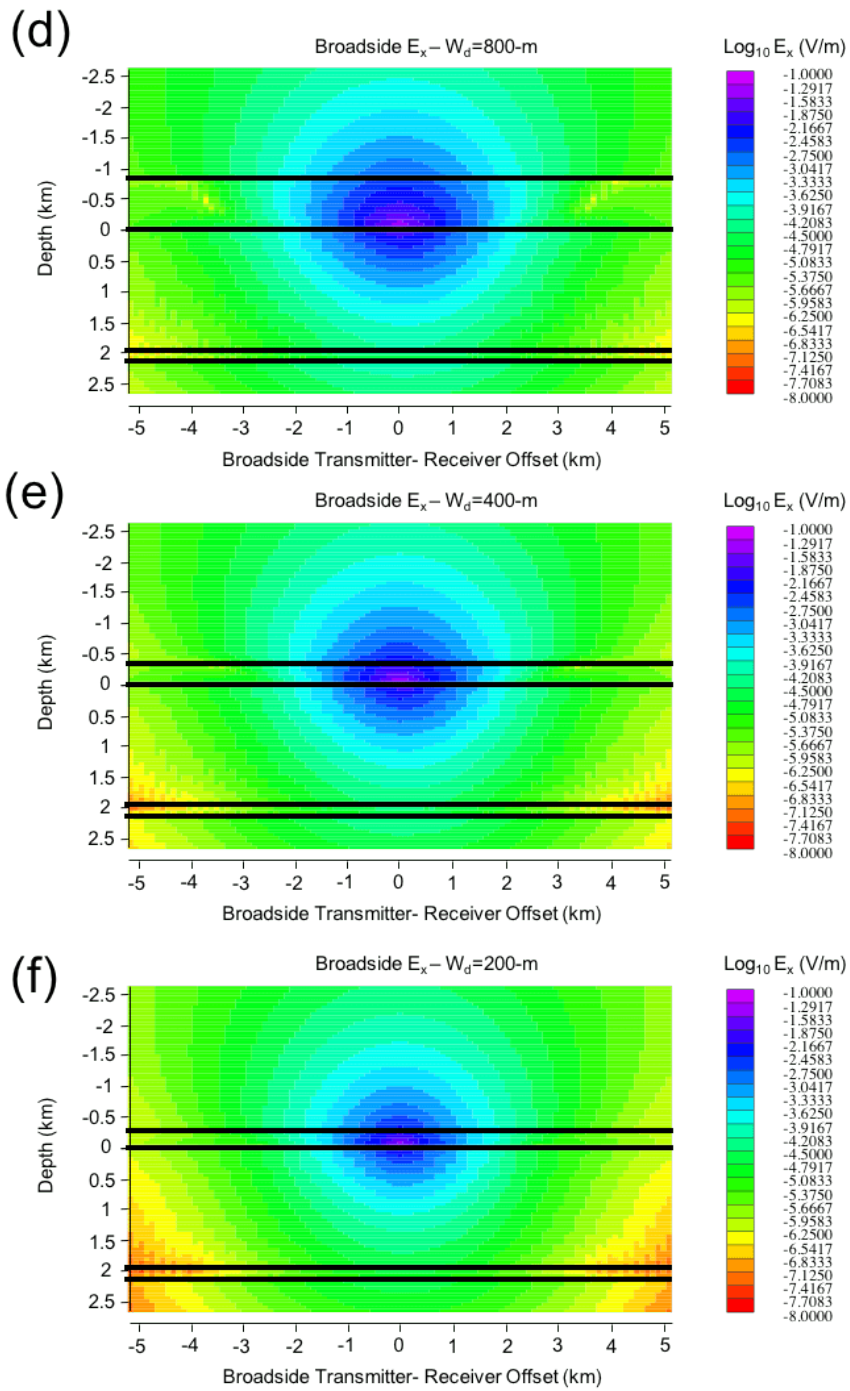
Figure 65 Continued
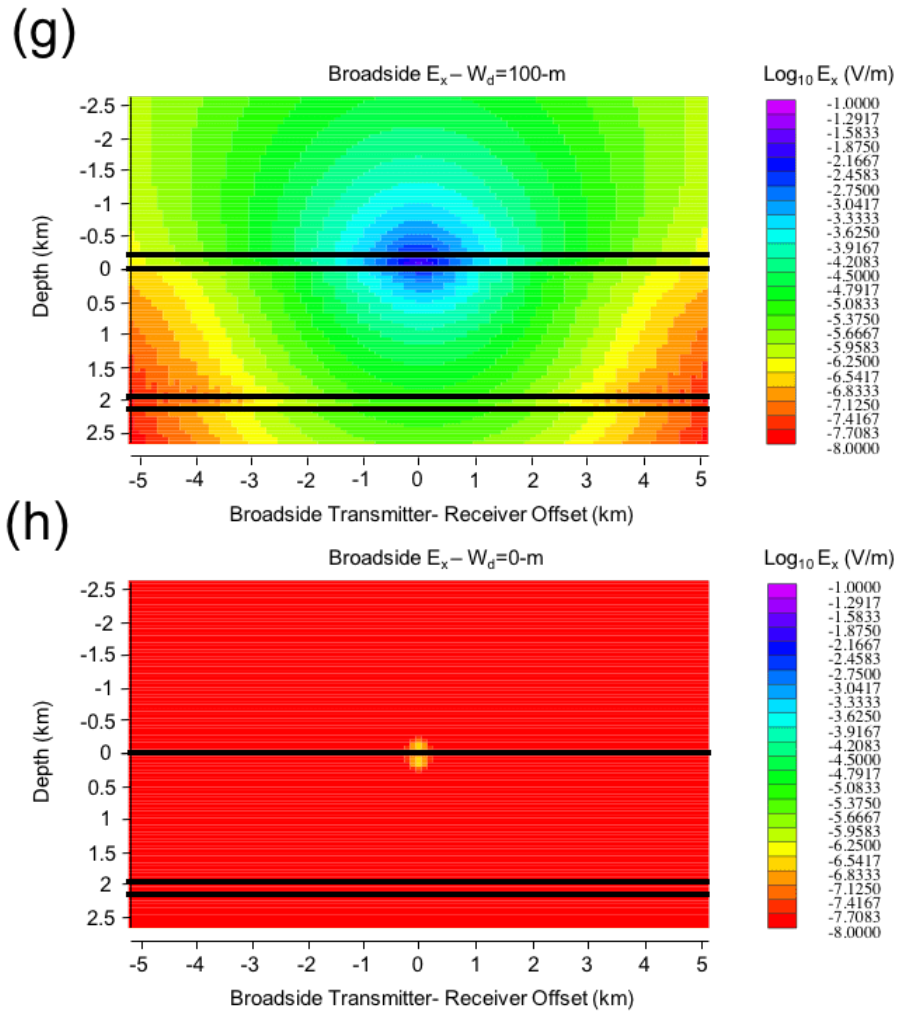
Figure 65 Continued
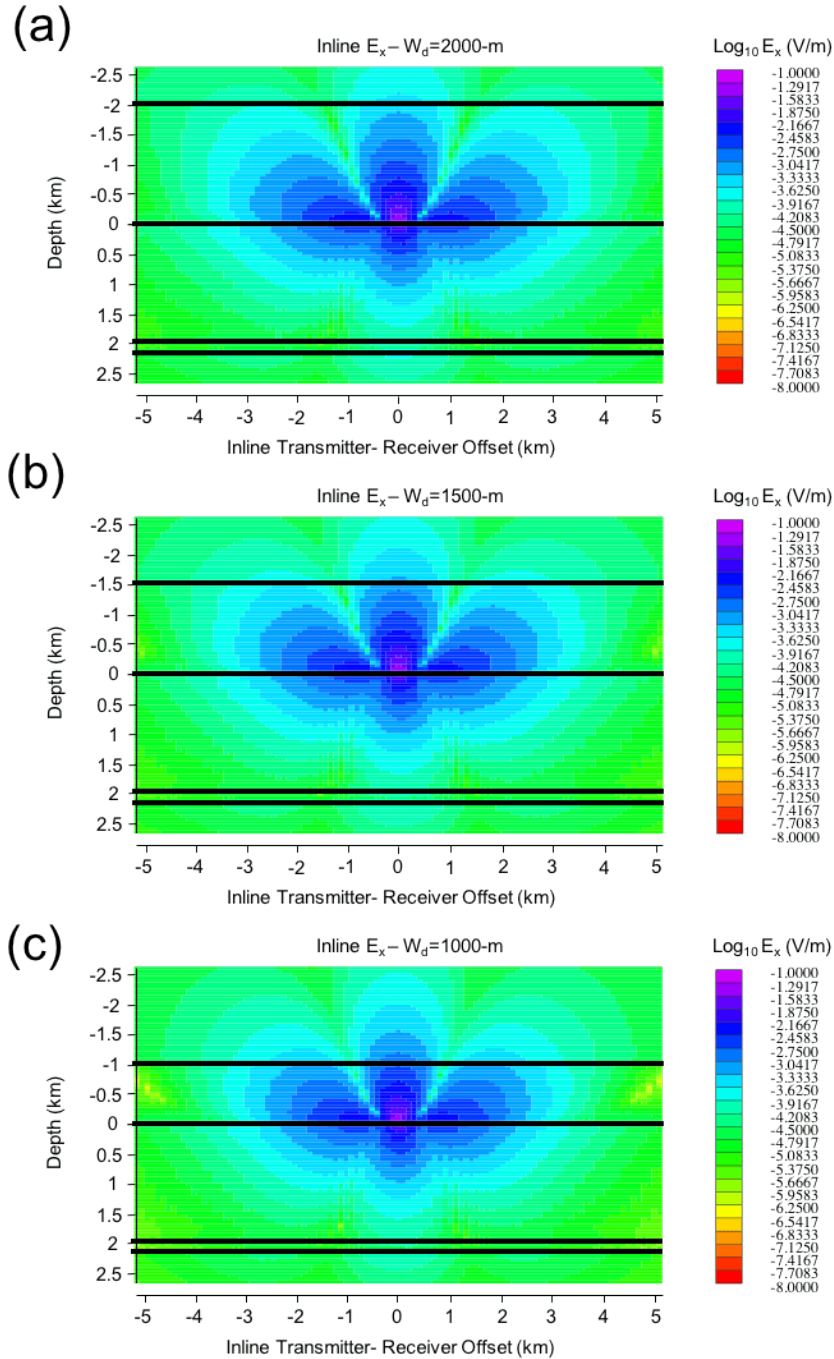
Figure 66 Inline E_x component for water depths of 2000 (a), 1500 (b), 1000 (c), 800 (d), 400 (e), 200 (f), 100 (g) and 0-m (h). The annotated lines represent the boundary between the air and water layers, the boundary between the water layer and sediment and the two boundaries between the sediment and the resistive layer as seen from top to bottom
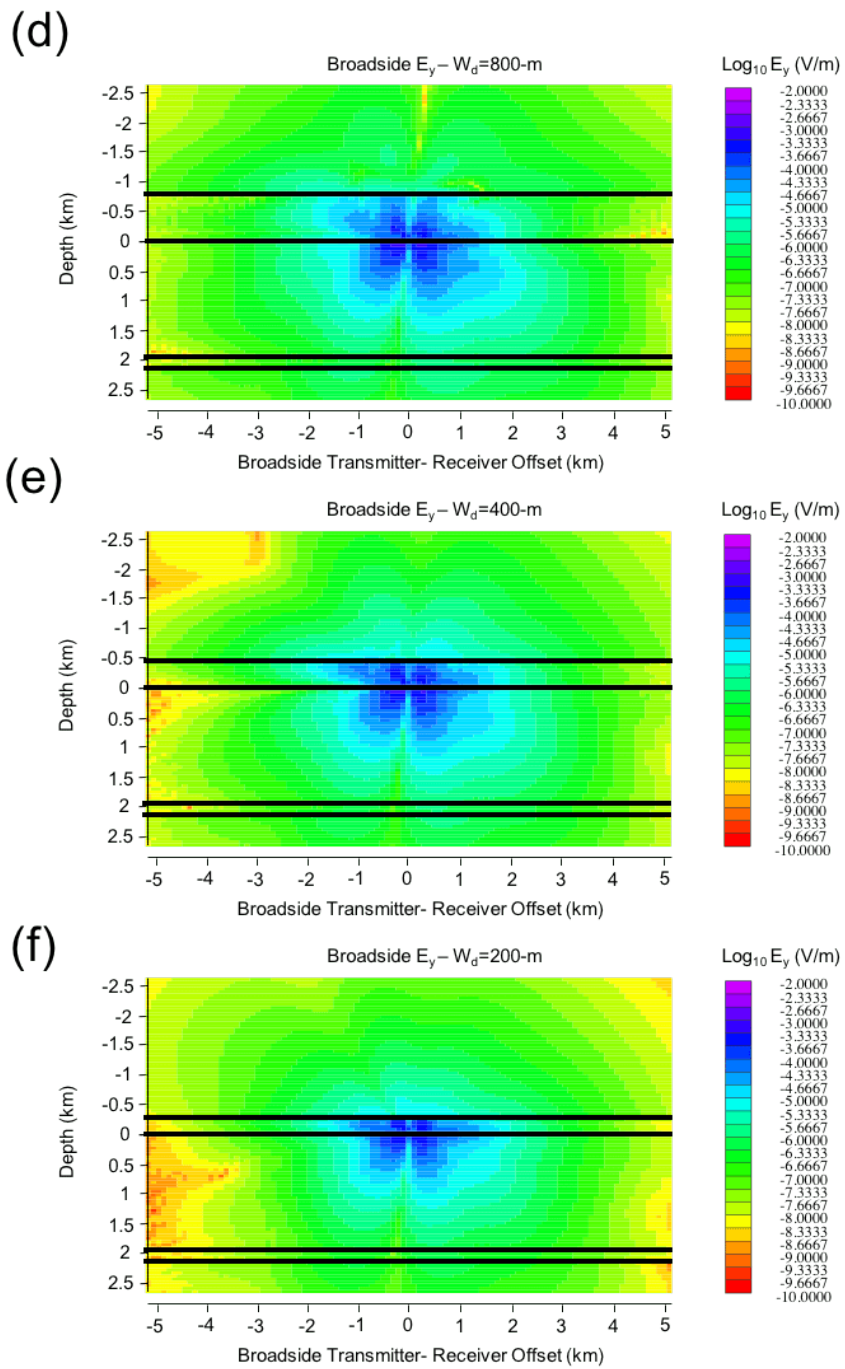
Figure 66 Continued

Figure 66 Continued

Figure 67 Broadside E_y component for water depths of 2000 (a), 1500 (b), 1000 (c), 800 (d), 400 (e), 200 (f), 100 (g) and 0-m (h). The annotated lines represent the boundary between the air and water layers, the boundary between the water layer and sediment and the two boundaries between the sediment and the resistive layer as seen from top to bottom
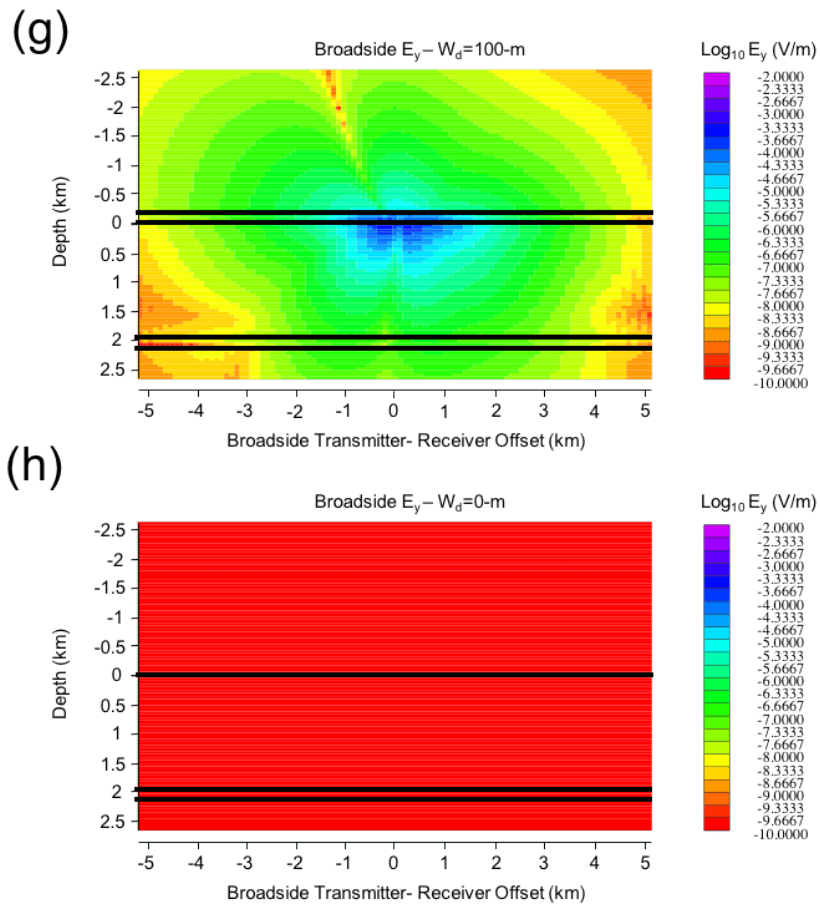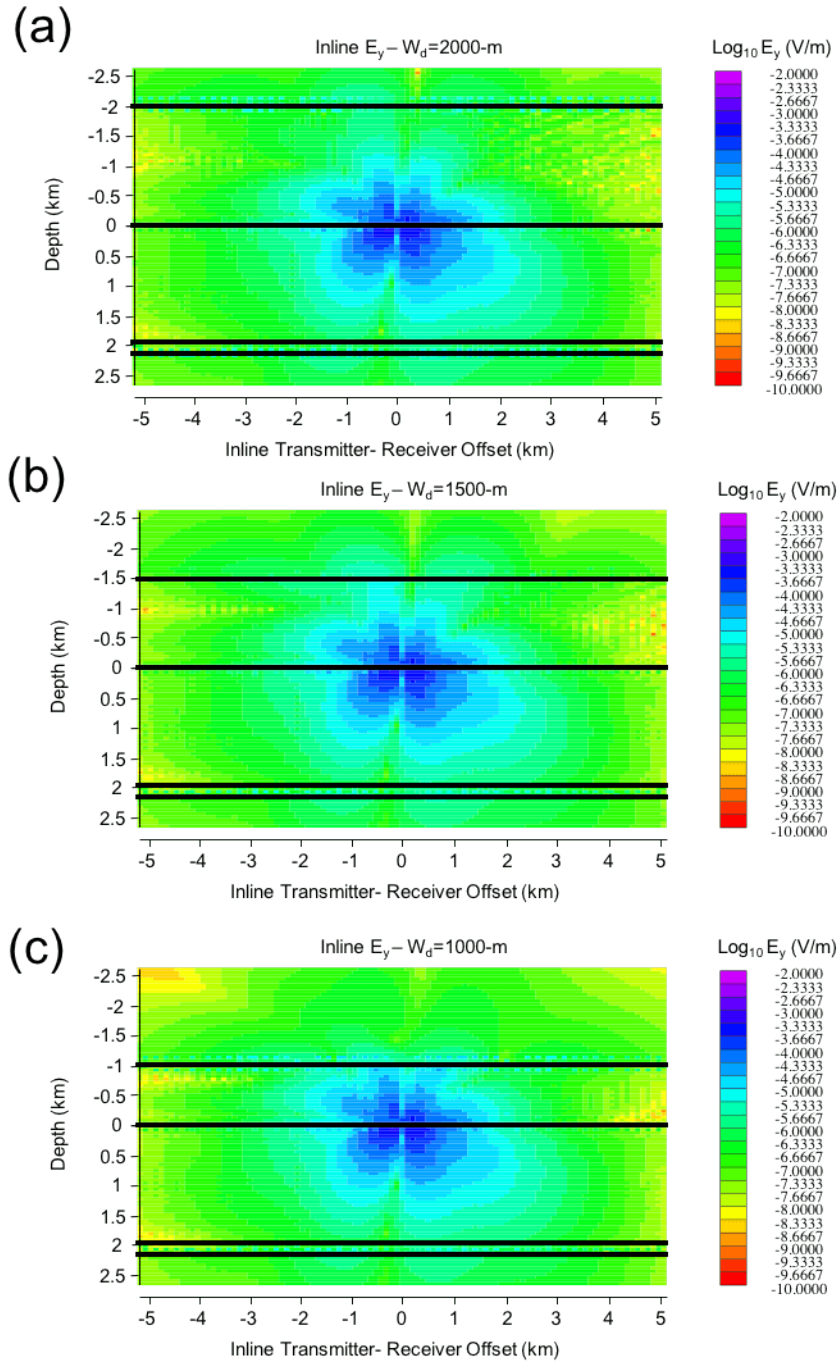
151

Figure 67 Continued

Figure 67 Continued

Figure 68 Inline E_y component for water depths of 2000 (a), 1500 (b), 1000 (c), 800 (d), 400 (e), 200 (f), 100 (g) and 0-m (h). The annotated lines represent the boundary between the air and water layers, the boundary between the water layer and sediment and the two boundaries between the sediment and the resistive layer as seen from top to bottom
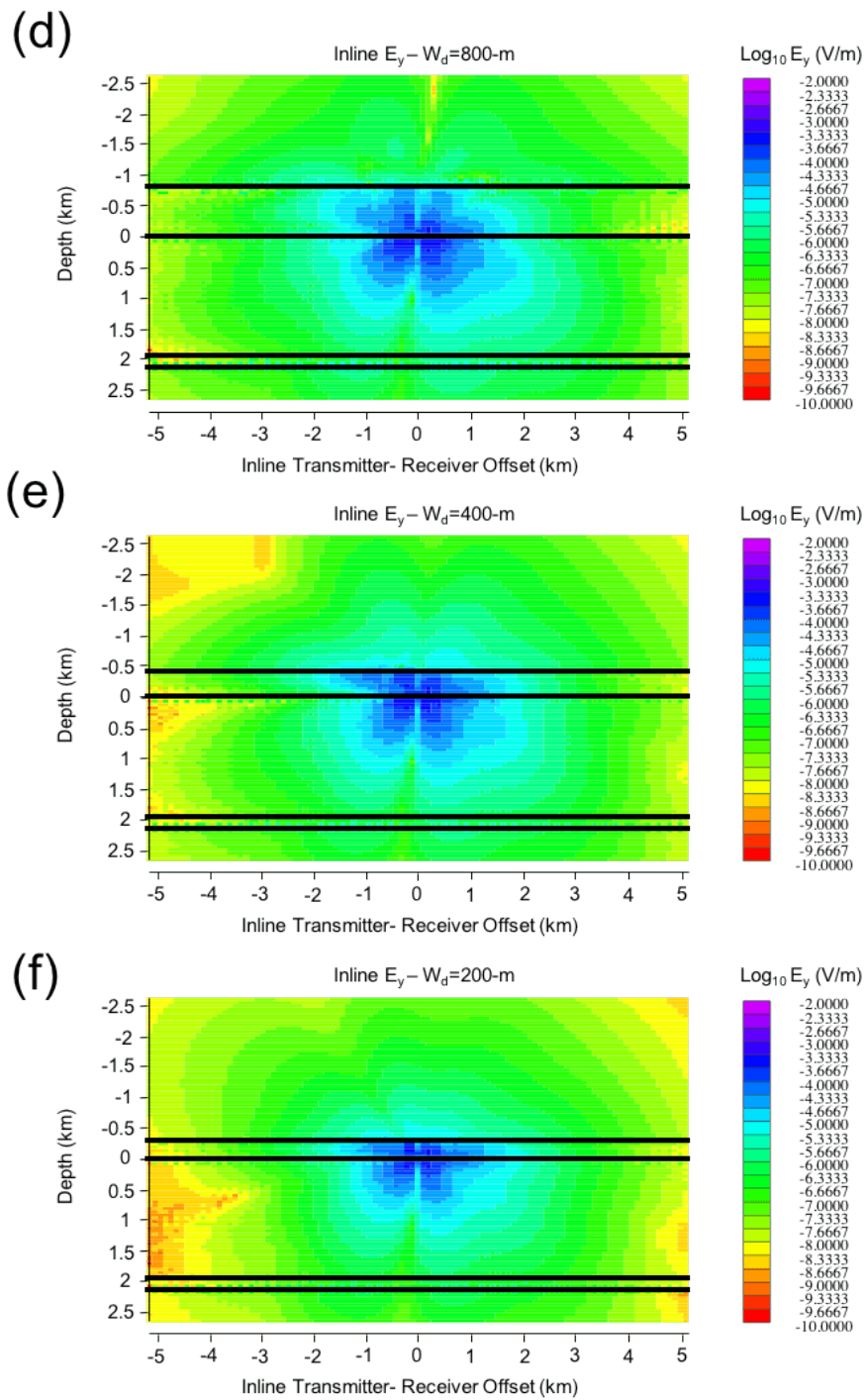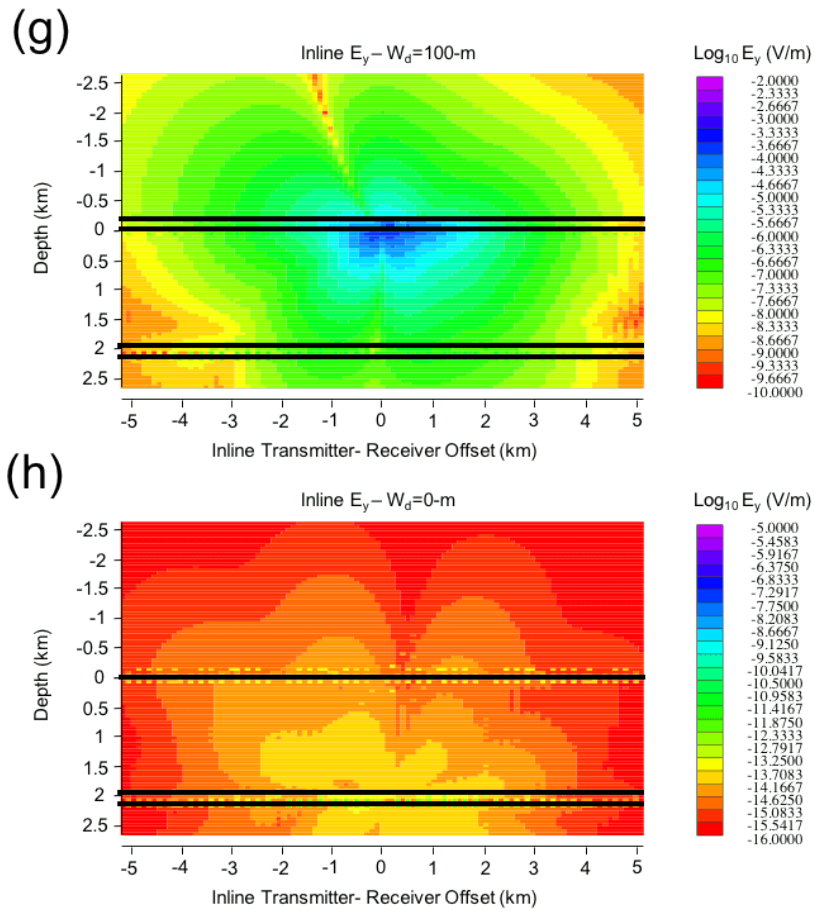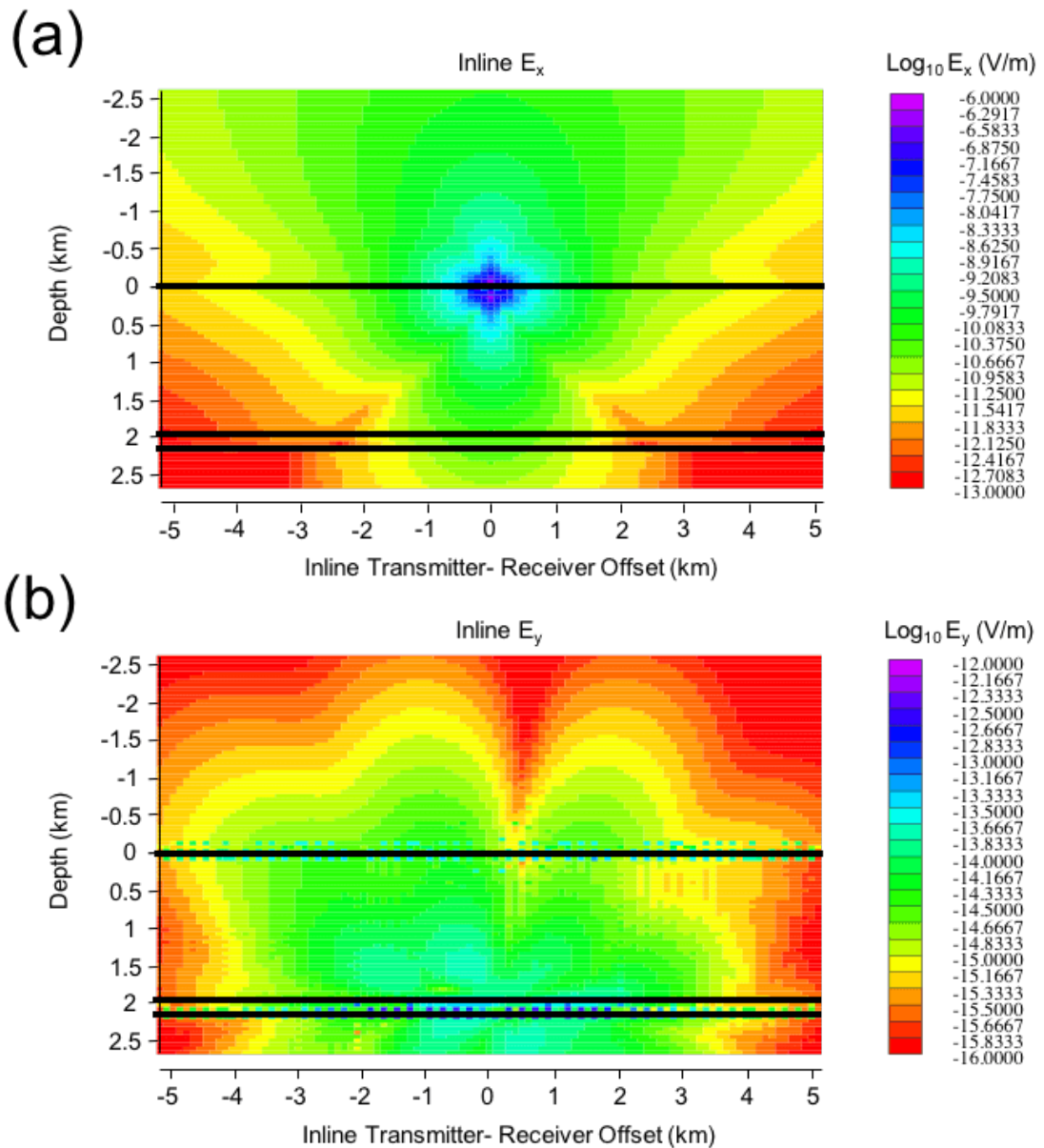
Figure 68 Continued

Figure 68 Continued

Figures 65 through 68 suggest for the resistive layer case, the water depth can be detected by all electric field components in both orientations, whereas the resistive layer is more distinguishable for broadside configurations. In general the water depth is best detected using the inline orientation, where the horizontal electric field components allow the water layer to be easily identified. The resistive layer is identified more easily as the water depth decreases due to a reduction in the overall amplitude and is most

easily identified in the inline direction. These observations are also visible in the

terrestrial case (figures 69 & 70).
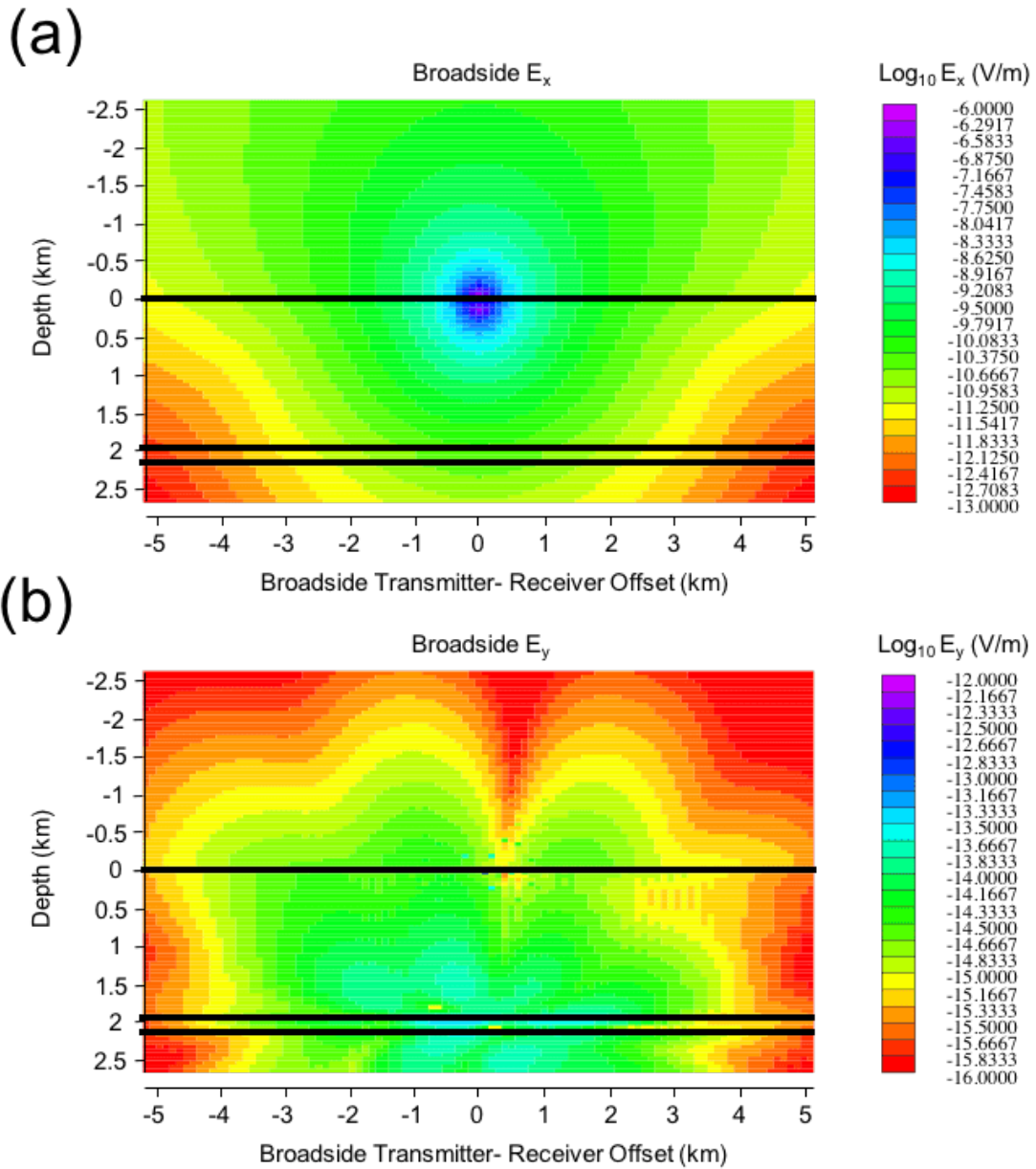
Figure 69 Broadside electric field patterns for each horizontal electric field component associated with the geoelectrical model shown in figure 62b for the terrestrial case. The annotated lines represent the boundary between the air sediment and the boundaries between the sediment and the resistive layer as seen from top to bottom

Figure 70 Inline electric field patterns for each horizontal electric field component associated with the geoelectrical model shown in figure 62b for the terrestrial case. The annotated lines represent the boundary between the air sediment and the boundaries between the sediment and the resistive layer as seen from top to bottom

For the resistive layer case, the water depth can be detected by all electric field components in both orientations, whereas the resistive layer is more distinguishable for inline configurations. In general the water depth is best detected using the inline orientation, where the horizontal electric field components allow the water layer to be easily identified. The resistive layer is identified more easily as the water depth decreases due to a reduction in the overall amplitude and is most easily identified in the inline direction.